NTNU
Norwegian University of
Science and Technology

Petrographical analysis of the diagenesis and reservoir quality of sandstones from the Nordmela and Fruholmen formations.

A study of the Fingerdjupet Sub-Basin in the Barents Sea.

Robert Andreas Havn Andresen

Petroleum Geoscience and Engineering
Submission date: June 2017
Supervisor: Mai Britt E. Mørk, IGP

Norwegian University of Science and Technology
Department of Geoscience and Petroleum

Abstract

The Barents Sea is going to be a key area for future hydrocarbon exploration activities on the Norwegian Continental Shelf in the years ahead. The reservoir quality of the formations native to the Barents Sea will be important knowledge for the oil companies in the future.

The objective of this paper is to determine the diagenetic processes and reservoir quality of the sandy sections of the Nordmela and Fruholmen Formations of the Realgrunnen Sub-Group in the Fingerdjupet Sub-Basin of the Barents Sea. A Petrographic analysis of thin sections taken from core samples has formed the basis of this study. Optical microscopy and electron microscopy were applied along with cathodoluminescence for cement quantification. The underlying Snadd Formation is included in the analysis to serve as a comparison to the two other formations.

The results of the analysis show a good reservoir potential in the middle “Reke” sequence of the Fruholmen Formation, with fair potential in the Nordmela Formation as a whole. The upper and lower “Krabbe” and “Akkar” sequences of the Fruholmen Formation have poor reservoir potential, and the Snadd Formation has very poor reservoir potential due to silt-sized grains and extremely low porosity.

Evidence of compaction, cementation, dissolution, alteration and diagenetic mineral replacement was found in the study. In addition, temperature evidence from mineral data imply an uplift of close to 2km.

Sammendrag

I årene som kommer vil Barentshavet være et kjerneområde for framtidige lete-aktiveter etter petroleum på den norske kontinentalsokkelen. I framtiden er reservoarkvaliteten til formasjonene som hører hjemme i Barentshavet viktig informasjon for oljeselskapene.

Målet med denne oppgaven er å bestemme reservoarpotensialet og de diagenetiske prosessene i de sandholdige delene av Nordmela Formasjonen og Fruholmen Formasjonen fra Realgrunnen-subgruppen i Fingerdjupet sub-bassenget. En Petrografisk analyse av tynnslip tatt fra kjerneprøver danner grunnlaget for studien. Optisk mikrosopering og elektron-mikroskopering ble anvendt i tillegg til katodeluminisens for bestemmelse av andelen diagenetisk sement. Den underliggende Snadd Formasjonen er tatt med i analysen for å kunne sammenlignes med de to andre formasjonene.

Resultatene av analysen viser et godt reservoarpotensiale i det midtre «Reke»-laget av Fruholmen Formasjonen, med et rimelig potensiale i Nordmela Formasjonen sett som helhet. De øvre og nedre «Krabbe» og «Akkar»-lagene i Fruholmen Formasjonen har dårlig reservoarpotensiale, og Snadd Formasjonen har meget dårlig reservoarpotensiale på grunn av silt-størrelse korn og lav porøsitet.

Bevis for kompaksjon, diagenetisk sementering, oppløsning, forvandling og substitusjon er funnet i analysen. I tillegg er det funnet temperatur-bevis i mineraldata som antyder en tektonisk oppløfting på nærmere 2km.

Foreword

I would like to thank Professor Mai Britt Engeness Mørk of the Department of Geoscience and Petroleum at NTNU for her help as the supervisor for this thesis.

I would also like to thank Mr. Kjetil Eriksen of the Department of Geoscience and Petroleum at NTNU for his help with laboratory work and my technical questions regarding SEM analysis.

I have also had email correspondence with Professor Ian Parsons of the University of Edinburgh's School of Geosciences, and I would like to thank him for his help with identifying feldspars.

Table of Contents

Abstract i

Sammendrag ii

Foreword iii

Table of figures vii

List of tables xii

Introduction 1

- Structure of the report 2

Theoretical framework 3

- Geology of the Barents Sea 3
- Local geology 5
- Realgrunnen subgroup 7
- Fruholmen Formation 8
- Nordmela Formation 9
- Background of the thin section samples 10

Methods 17

- Thin section analysis 17
- Porosity determination 18
- Scanning Electron Microscope (SEM) – Backscatter Electron (BSE) imaging 19
- Scanning Electron Microscope (SEM) – Energy Dispersive X-ray Spectroscopy (EDS) 19
- Scanning Electron Microscope (SEM) – Cathodoluminescence (CL) 20

Results 23

- Results of petrography 23

Classification of formations in Dott-diagram 25

Formation petrography 31

Nordmela Formation 31

Fruholmen Formation 37

Snadd Formation 41

Results of EDS and BSE analysis 45

Nordmela Formation 45

Fruholmen Formation 50

Snadd Formation 56

Discussion 59

Diagenetic processes observed in the thin sections 59

Comparison between the formations and reservoir quality 71

Conclusion 73

Future research 74

References 75

Appendix A – CL photos 79

Appendix B – EDS spectra 92

Appendix C – perthite data points 104

Table of figures

Figure 1: Map of the greater Barents Sea with selected structural features superimposed (Marello et al., 2013) 4

Figure 2: Map of the Norwegian Barents Sea with fault boundaries visible. Emphasis on the location of the Fingerdjupet Sub-Basin in yellow. Purple rectangle represents block 7321/8, and the purple dot represents the well location of well 7321/8-1. Original image taken from the Norwegian petroleum directorate (Gabrielsen et al., 1990). 6

Figure 3: Stratigraphic chart of the Barents Sea with emphasis on the South Western Barents Sea Realgrunnen Sub-group and underlying Snadd-formation. (Ogg, 2013) with modifications. 7

Figure 4: An illustration showing the suggested transgressive event in which the tidal-flat Nordmela Formation was deposited (Olaussen et al., 1984). 9

Figure 5: Exposed cores from well 7321/8-1. a) Left image shows the interval 2839m-2844m of the Snadd formatioon. a) and b) showing the mud-laminated sands of the snadd formation studied in thin section of the interval 2839m-2846.81m. 11

Figure 6: Exposed cores from well 7321/8-1. Purple bars represents boundary. a) Left image shows the interval 1493.7m-1498m, interpreted as the boundary between the krabbe and reke members in the fruholmen formation. b) right image shows depth interval 1526mm-1531m, showing the breccia-like mud clasts in the middle of the Reke member of the Nordmela formation, purple arrow for emphasis. 12

Figure 7: Exposed cores from well 7321/8-1. Purple bars represent formation boundaries. a) Left image shows the interval 1443m-1458m, interpreted as the boundary between the stø and nordmela formations. b) right image shows depth interval 1465.5m-1470m, interpreted as the boundary between the nordmela and fruholmen formations. 13

Figure 8: The formation depths as given in the well report for well 7321/8-1. RKB = Rotary Kelly Bushing. Extracted from the document “1070_01_WDSS_General_Information” (Oljedirektoratet, 2005) 14

Figure 9: Well log of well 7321/8-1 in the interval where most of the samples are taken. Left depth bar is measured depth, right depth bar is true vertical depth subsea (Oljedirektoratet, 2005). 15

Figure 10: Examples of areas and scale used during point counting. Left image shows typical sandstone photo sued, right image shows typical image used when clay laminations are present. Scale bar shows 500µm, representing 5x optical zoom. 18

Figure 11: CL photo example showing the quantification of quartz cement using the KLONK Image Measurement software. Blue lines are measuring lines. 21

Figure 12: The Dott classification ternary diagram for sandstones (Dott Jr, 1964) 25

Figure 13: A visualisation of the data presented in Table 2 26

Figure 14: QFL-Diagram using the data in Table 2 for Dott-Classification of siliciclastic rocks. 28

Figure 15: QFL diagram using recalculated values to correct for quartz cement values listed in Table 3. 28

Figure 16: Phases of textural maturity based on rounding, sorting and removal of clay. Based on Folk (1951) with modifications (Folk, 1951). 30

Figure 17: Thin section photo of partly dissolved microcline in the upper right corner. plane polarized light (left) and cross polarized light (right). Depth = 1460.80m, Nordmela Formation. 31

Figure 18: Thin section photograph showing deformed muscovite and illite grain coatings. Nordmela Formation, depth = 1460.80m. 32

Figure 19: Thin section photos of quartz grain boundaries and schistose quartz in the centre. The schistose quartz is assumed to be a rock fragment as no other quartz grains in the formation exhibits polycrystalline patterns. Nordmela Formation, depth = 1463.70m. 32

Figure 20: Thin section photos of deformed muscovite (centre) and carbonate cement (right). Nordmela Formation, depth = 1460.80m. 33

Figure 21: Thin section photos showing clay aggregate in upper right corner with dust rim inside the grain. Depth = 1460.80m, Nordmela Formation. 34

Figure 22: Thin section photos showing quartz cementation on quartz grains and albite cement on K-feldspar. Nordmela Formation, depth = 1463.70m. 35

Figure 23: Diagenetic kaolinite replacing detrital grains (presumably K-feldspar). Illitization of plagioclase grain (centre). Depth = 1460.85m, Nordmela Formation. 36

Figure 24: Thin section photo of diagenetic kaolinite having replaced what is presumably a feldspar grain. Note organic matter at the grain’s right-side edge. Nordmela Formation, depth = 1463.70m. 36

Figure 25: Thin section photograph of plagioclase (top) and K-feldspar (middle) being partly dissolved. Fruholmen Formation, depth = 1495.44m. 37

Figure 26: Thin section photograph of deformed muscovite and pore-filling kaolinite/illite. Fruholmen Formation, depth = 1495.44m. 38

Figure 27: Thin section photograph showing stylolites with dissolved muscovite in the centre and pyrite grains and organic matter along the lamination. Fruholmen Formation, depth = 1543.02m. 38

Figure 28: Thin section photograph of quartz cemented quartz grains. The grains are larger closer to the stylolites. Fruholmen Formation, depth = 1468.90m. 39

Figure 29: Thin section photos of illitization of plagioclase and illite grain coatings. Fruholmen Formation, depth = 1538.32m. 39

Figure 30: Thin section photograph showing pyrite grain with siderite coatings. Fruholmen Formation, depth = 1468.90m. 40

Figure 31: Thin section photograph showing the grain size transition zone, with larger grains above the horizon outlined in the picture. Snadd Formation, depth = 2840.50m. 41

Figure 32: Thin section photograph showing grain size difference in Snadd. Upper photographs have Medium to Fine grains, while lower photographs have Fine to Very fine grains. Snadd Formation, depth = 2840.50m. 42

Figure 33: Thin section photograph showing clay laminations and fracture porosity. Snadd Formation, depth = 2846.70m 43

Figure 34: Backscatter image showing quartz grains, albite grains, kaolinite booklets and siderite cement. Nordmela formation, depth = 1460.55m. 46

Figure 35: Backscatter image showing chlorite grains which appear to overgrow albite grains. Small illite grains are also visible growing in quartz in the lower right corner. Nordmela formation, depth = 1460.55m. 46

Figure 36: Backscatter photograph showing displasive growth of siderite in chlorite. Nordmela Formation, depth = 1460.80m. 47

Figure 37: Backscatter image showing grain consisting of albite and oligoclase lamellae. Nordmela formation, depth = 1460.80m. 47

Figure 38: Backscatter image showing abundant albite intergrowing with calcite, siderite, illite and chlorite. The uncharacteristic shape of the calcite crystals might be the result of a cross section of hopper-habit calcite or dedolomitization. Dissolution of albite in the right side of the image. Nordmela formation, depth = 1460.85m. 48

Figure 39: Backscatter image showing a Rare-Earth-Elements (REE) rich veins running through quartz. Vein mineral identified as lanthanum-florencite. Nordmela formation, depth = 1463.70m. 49

Figure 40: Backscatter image showing cemented quartz grains, pyrite growing on illite and muscovite being replaced by kaolinite. Nordmela formation, depth = 1463.70m. 49

Figure 41: Backscatter image showing pyrite cement around quartz and partially dissolved albite. Accessory rutile and siderite. Fruholmen formation, depth = 1468.90m. 51

Figure 42: Backscatter image showing siderite surrounding pyrite grains. Contains both regular illite and Ti-enriched illite. Fruholmen formation, depth = 1468.90m. 51

Figure 43: Backscatter image showing illite growing both in and coating quartz grains. Both regular and C-enriched illite, with coal-illite lamellae visible. Long fibrous illite strands almost parallel to chlorite. Small grains of florencite. Fruholmen formation, depth = 1468.90m. 52

Figure 44: Backscatter image showing the content of a clay lamination running through the otherwise sand-rich thin section. High siderite content, along with a matrix consisting of quartz, illite, albite and chlorite. Fruholmen formation, depth = 1468.90m. 52

Figure 45: Backscatter image showing alternating coal and Ti-enriched illite lamellae along with rutile grains. Fruholmen formation, depth = 1487.95m. 53

Figure 46: Backscatter image showing a stylolite with high concentration of heavy minerals and organic material. Fruholmen formation, depth = 1495.44m. 53

Figure 47: Backscatter image showing magnesium-rich calcite surrounding illite and quartz intergrowths. Fruholmen formation, depth = 1513.41m. 54

Figure 48: Backscatter image showing illite replacing muscovite and retaining the mica-morphology. Siderite crystals are shown to accumulate around illite with distinct rounding of illite grains. Fruholmen formation, depth = 1513.41m.. 54

Figure 49: Backscatter image of siderite strands with mica-like morphology, Possibly replacing a biotite. Also shown is calcite, chlorite and albite. Lower right corner shows partly dissolved albite with illite and siderite. Fruholmen formation, depth = 1538.32m. 55

Figure 50: Backscatter image showing illite replacing muscovite. The quartz in the right side of the picture can be seen being limited by the illite-muscovite. Depth = 1543.02m. 55

Figure 51: Backscatter image showing ankerite cement, mixed layer illite-chlorite parallel with what might be glauconite. Pyrite and quartz/chert. Snadd formation, depth = 2840.50m. 56

Figure 52: Backscatter image showing coal fragments and muscovite being replaced by lamellae of chlorite and possibly glauconite. Snadd formation, depth = 2846.70m.. 57

Figure 53: Backscatter image showing euhedral siderite crystals. Euhedral quartz face in lower right corner bordering Mg-rich calcite cement. Snadd formation, depth = 2846.70 57

Figure 54: A graphic representation of kaolinite-dickite alteration (Beaufort et al., 1998)...................... 61

Figure 55: Albite-oligoclase lamellae seen under CL. Same lamellar grain as presented in the Nordmela results section for backscatter photos... 64

Figure 56: Plagioclase phase diagram as proposed by Nord et al. Peristerite miscibility gap shown in the lower left corner. (Parsons, 2012) 64

Figure 57: Relevant permeability remarks in Hydro documents. Extracted from document “1070_1” in the well directory (Oljedirektoratet, 2005) 66

Figure 58: EDS spectra showing the monazite found in the thin section sample to the left and a confirmed monazite in the upper right corner. Note that the oxygen-peak is missing from the right image.. 68

Figure 59: Overview of processes involved in authigenic development of REE-Al-phosphates. Reproduced with the kind persmission of Birger Rasmussen (Rasmussen, 1996). 69

List of tables

Table 1: Porosity from KLONK Image Measurement porosity analysis in addition to grain size and sorting observed in the thin sections. 24

Table 2: Point counting data with porosity and grain volumes. Note that the grain volumes are recalculated as percentages of grain volume excluding porosity 26

Table 3: Detrital grain and cement as percentage of total quartz grain volume 27

Introduction

The objective of this paper is to present a descriptive analysis of rock samples taken from the Barents Sea and to comment on the reservoir properties and diagenetic processes of the sandstone intervals studied. This is done to better understand the potential for future hydrocarbon exploration and production in the Barents Sea. The samples originate from well number 7321/8-1 in the Fingerdjupet Sub-Basin in the Barents Sea, and ten out of twelve of the samples correspond to parts of the Realgrunnen Sub-Group, namely the Nordmela and Fruholmen formations present in this area. The Nordmela and Fruholmen formations will be the main subjects of analysis, with the Snadd Formation serving as a comparison due to the Snadd samples originating from more than 1300m deeper than the other samples and belonging to a different Sub-Group.

A Petrographic description will be presented including the detrital grains, matrix and diagenetic grains. The author moves on to present information gleaned through use of Scanning Electron Microscope. Furthermore, the diagenetic processes that were observed will be discussed along with an analysis of the reservoir quality of the formations.

This paper is a continuation of an unpublished semester project at the Norwegian University of Science and Technology during the fall semester of 2016 written by the same author. The scope of the previous work was the use of optical microscopy without the use of more advanced methods employed in this paper. As such, data in the form of photographs of optical microscopy are the same in both papers. In addition, the geological introductions are in part similar in both papers, with modified figures and extra text added for this thesis.

The 7321/8-1 well has previously been the subject of analysis in a master’s thesis written by Helene Rønning at the Norwegian University of Science and Technology (Rønning, 2011). This previous paper used samples from the Stø and Nordmela Formations. The thin section samples used in the analysis of the Nordmela Formation in the current paper are different from those used in Rønning’s paper, although the samples are taken from the same depth interval and therefore some of the same NPD core sample photos have been used.

Structure of the report

The structure of the report will be ordered in the following way, with 1 being first and 7 being last:

1. The **geological background** of the Barents Sea, the local geology and the formations studied in this paper will be presented.
2. **A background of the samples** will be given and relevant previous work in the area will be outlined.
3. The **methods** employed in this study will be presented
4. The **results** from the Petrographic analysis will be presented along with photos of the thin sections in optical and electron microscopes and the measured quantities of quartz cement. All optical photos are pairs in plane polarized and cross polarized light, while backscatter images are presented on their own.
5. Results from the Petrographic analysis observations will be **discussed** along with the reservoir characteristics of the studied formations.
6. The **conclusion** will be given.
7. Areas of **future research** will be suggested.

Theoretical framework

Geology of the Barents Sea

The Barents Sea contains several basins thought to be the home of hydrocarbon reservoirs, with proven reserves in Snøhvit, Goliath and other reservoirs yet to be produced in Norwegian territory. The Jurassic formations have proven to be the most successful hydrocarbon exploration targets in the Norwegian territory, with most of the activity having taken place in the Hammerfest Basin (Johansen et al., 1992). The greater Barents Sea includes Russian territory, and earlier Norwegian-Soviet cooperation has made it possible to map the greater Barents Sea. Based on discoveries, the greater Barents Sea is thought to have more oil prone reservoirs in the east and greater gas prone reservoirs in the west and centre (Johansen et al., 1992). See Figure **1** for a map showing the areas described. The 23rd licensing round for the Norwegian continental shelf is the first in 20 years to contain areas that are as of yet unexplored by the oil industry. Also, the Norwegian government has announced that the Barents Sea will most likely be a key area for the 24th licensing round (Statsministerens-kontor, 2016).

Major events

The Barents Sea continental shelf basement was formed by three major orogenic events: The Timanian, the Caledonian and the Uralian events (Marello et al., 2013).

The Timanian event: A Neoproterozoic to early Cambrian event which involved the south-eastern parts of the greater Barents Sea. Orogenic deformation and metamorphism led to accretions of magmato-sedimentary deposits along the north-eastern margin of Baltica, forming NE-SW trending folds with SW-vergence (Marello et al., 2013).

The Caledonian event: An early Ordovician to mid-Silurian / early Devonian event, ending with the collision of Baltica and Laurentia in the mid-Silurian. The western Barents Sea was affected, with N-S structural trends in the north-western part of the area. Basement on the mainland consists of both Fennoscandic autochtons and Caledonian allochtons, with the Caledonian basement stretching into the Barents Sea overlain by younger sediments (Johansen et al., 1992; Marello et al., 2013).

The Uralian event: An early Carboniferous to early Jurassic event, responsible for the formation of the Ural Mountains. Subduction of the Ural Ocean beneath the Siberian craton started in the early Carboniferous, followed by the collision of Laurussia and Siberia in the early Permian. The westwards over-thrusting created the Ural Mountains, with the Novaya Zemlya (visible in Figure **1**) considered to be the northern extension of the Urals and the eastern boundary of the Barents Sea, with the western boundary being the Norwegian-Greenland Sea (Marello et al., 2013).

Periods of rifting from the late Paleozoic to the Mesozoic culminated with the opening of the Norwegian-Greenland Sea. Three periods of uplift have been identified in the Paleocene, Oligocene and Pliocene/Pleistocene (Ohm et al., 2008). Erosion in the Paleogene and Neogene has removed 600m of sediments on average (Vorren et al., 1991).

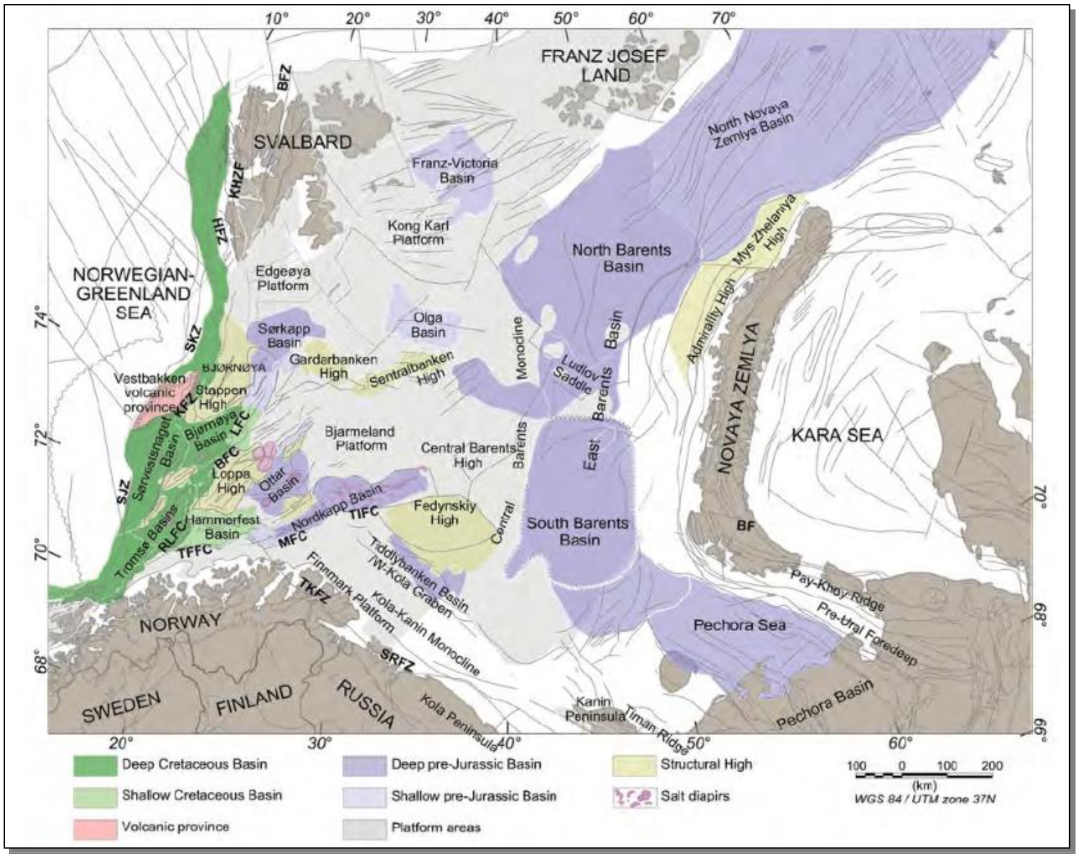

Figure 1: Map of the greater Barents Sea with selected structural features superimposed (Marello et al., 2013)

Local geology

The southwestern part of the Barents Sea is the area which is the most relevant for this paper, as it is the home of the Fingerdjupet Sub-Basin.

The southern areas of the Barents Sea which are located west of the Ringvassøy-Loppa Fault Complex and the Bjørnøyrenna Fault Complex are characterized by thick sediments in the Bjørnøya, Harstad and Tromsø Basins of Cretaceous, Paleogene and Neogene origin. This area was tectonically active in the late Mesozoic and Cenozoic times, and the faults in the area have NE-SW to N-S trends (Oljedirektoratet, 2014a).

The Loppa High and surrounding area has complex geological history. Several phases of uplift and subsidence have been followed by tilting and erosion. Upper Paleozoic siliciclastics, carbonates and evaporites filled and overlaid rift topography from the Late Carboniferous. The Loppa Ridge was uplifted and tilted during the Late Permian to Early Triassic. Gradual onlap followed during the Early and Middle Triassic, followed by deposition of thick Upper Trassic sediments of the Snadd Formation. (Oljedirektoratet, 2014a)

The Fingerdjupet Sub-Basin is located in the northeastern part of the Bjørnøya Basin, bounded by the Bjarmeland Platform to the east and the Loppa High to the southeast (Gabrielsen et al., 1990). The Leirdjupet Fault Complex provides the southern and western boundary along the Bjørnøya Basin. The Fingerdjupet Sub-Basin is thought to have the same history as the Stappen and Loppa Highs up to the Middle Triassic.

In the Middle Triassic to Middle Jurassic, the Fingerdjupet Sub-Basin was part of the regional cratonic platform (Gabrielsen et al., 1990). Late Jurassic tectonism generated the dominant NNE-SSW trending fault blocks, which were reactivated in the Early Cretaceous. The faults might have been reactivated in the Paleogene and Neogene. Erosion in this period has removed up to 2km of sediments in the area (Gabrielsen et al., 1990), and an increase in the erosion took place during the Quaternary due to glaciation (Oljedirektoratet, 2014a).

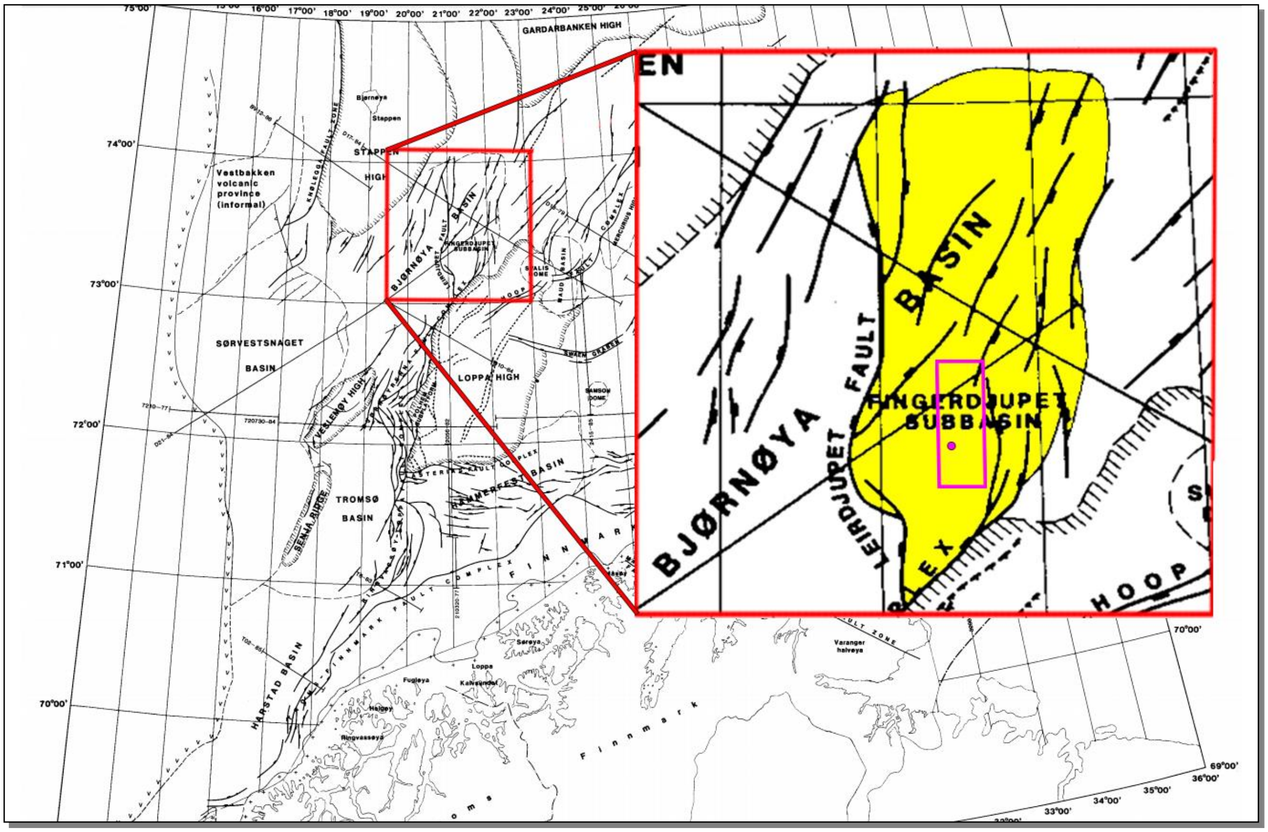

Figure 2: Map of the Norwegian Barents Sea with fault boundaries visible. Emphasis on the location of the Fingerdjupet Sub-Basin in yellow. Purple rectangle represents block 7321/8, and the purple dot represents the well location of well 7321/8-1. Original image taken from the Norwegian petroleum directorate (Gabrielsen et al., 1990).

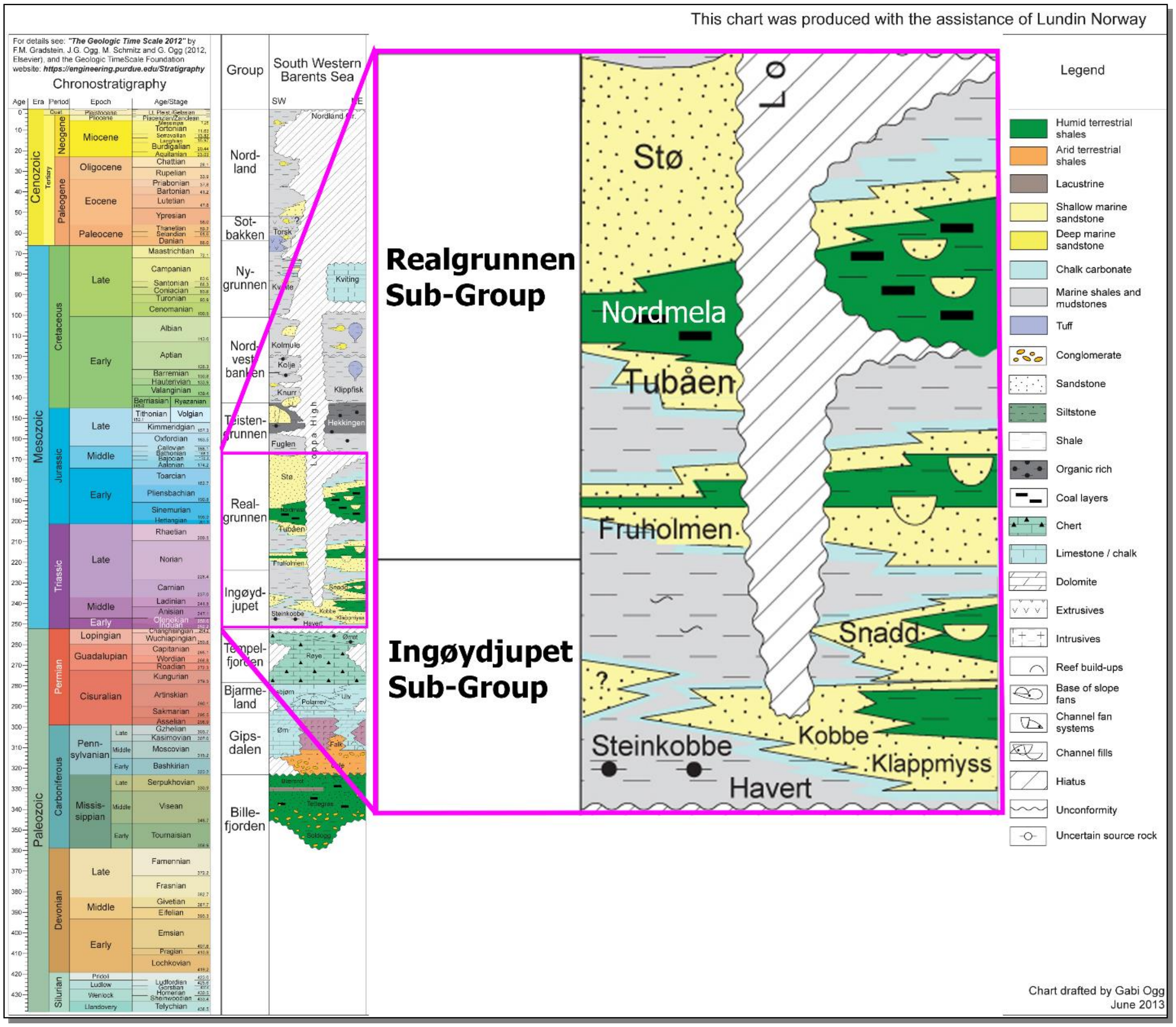

FIGURE 3: STRATIGRAPHIC CHART OF THE BARENTS SEA WITH EMPHASIS ON THE SOUTH WESTERN BARENTS SEA REALGRUNNEN SUB-GROUP AND UNDERLYING SNADD-FORMATION. (OGG, 2013) WITH MODIFICATIONS.

Realgrunnen subgroup

The Realgrunnen Sub-Group of the Kapp Toscana Group consists of four formations as seen in figure **3**: Fruholmen, Tubåen, Nordmela and Stø. The Fruholmen and Nordmela Formations are the most relevant formations for this paper because ten out of twelve of the samples are taken from these formations. The Snadd Formation of the Storfjorden Sub-Group is only included for comparison, and is therefore not expanded upon in this section.

Fruholmen Formation

The Fruholmen Formation is the lower part of the Realgrunnen Sub-Group and is of late Triassic to middle Jurassic origin. Along with the Nordmela Formation, it was deposited in a tectonically quiet environment (Johansen et al., 1992). The Fruholmen Formation is thought to represent the transition from open marine to costal and fluvial sandstones with a fluviodeltaic progradation northwards. As the deltaic input shifted laterally, the northern parts of the basin accreted marine deposits while the centre and southern parts accreted flood-plain deposits (Dalland et al., 1988).

The Fruholmen Formation is divided into three members: Akkar, Reke and Krabbe.

The Akkar Member: This is the lowermost sequence dominated by grey to dark grey shales with interbedded sandstones and coal, interpreted as marine deposits. Log readings show a sharp increase in gamma ray signature compared to the underlying Snadd Formation, with more moderate increases in sonic travel time and bulk density (Dalland et al., 1988).

The Reke Member: The middle sequence consists of sandstones with cross bedding and is interpreted to be a coastal and fluvial channel deposit. The base of the sequence is defined by a carbonate horizon which shows up as lower density-neutron separation in well logs. It has a lower and more funnel shaped gamma ray signature (Dalland et al., 1988).

The Krabbe Member: The upper sequence consists of shales and is thought to be a marine deposit to the north and a flood-plain deposit to the centre and southern parts of the Western Barents Sea. Defined by larger separation in density-neutron logs, and like the Reke sequence it has a funnel shaped gamma ray signature (Dalland et al., 1988).

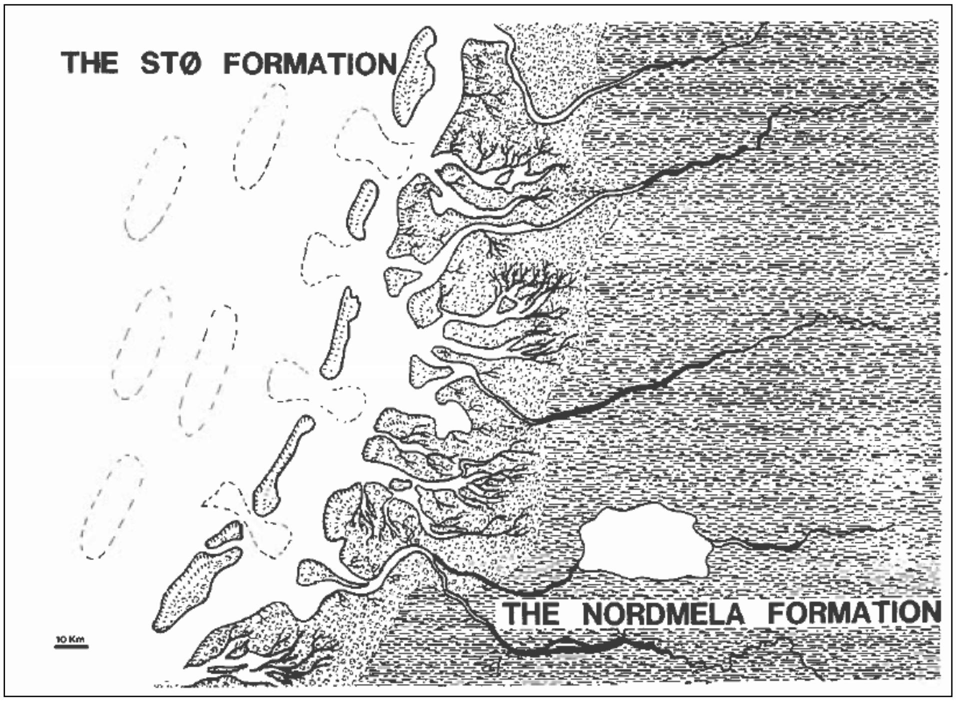

Figure 4: An illustration showing the suggested transgressive event in which the tidal-flat Nordmela Formation was deposited (Olaussen et al., 1984).

Nordmela Formation

The Nordmela Formation is an interbedded formation with siltstones, sandstones, shale and mudstones with minor coals (Oljedirektoratet, 2014b). It is of Early Jurassic age, with a coarsening upwards of channel sands and sandstones are frequently interbedded with thin mudstone layers (Olaussen et al., 1984). Plant roots and marine bioturbation occur in the same layer or alternating beds, which along with flaser bedding, lenticular bedding and wave ripples suggests tidal flat to flood plain origins (Dalland et al., 1988).

The formation is divided into three sub-units: Units N1, N2 and N3.

The lower unit N1 is thought to be a tidal flat sequence with flaser bedding, root traces and marine fossils. It is thoroughly interbedded and has a serrated gamma ray signature. Due to the fine to very find sand grains and the frequent interbedding with mudstones, unit N1 is considered to have poor reservoir quality (Olaussen et al., 1984).

The middle unit N2 has a higher separation of mudstone and sandstone layers, yielding better reservoir properties. Coal beds and plant fragments are more frequent than in unit N1, and it is thought to be a meandering channel deposit with channel fill (Olaussen et al., 1984).

The upper unit N3 has a fining upwards sequence with bell shaped gamma ray signatures. The grain size in the lower part of unit N3 is coarser grained than the rest of the formation. Cross bedding, current ripples, plant roots and thin coal-containing beds are present. Several of the sandy sequences have erosional bases with upwards fining gradients. The reservoir quality is considered to be good in the lower part of unit N3. The upper part of unit N3 has poorer reservoir qualities due to higher mudstone content and intense to moderate bioturbation. The plant roots and thin coal-containing beds are not found in the upper part of unit N3. Unit N3 is thought to be a transgressive deposit in the lower part which becomes a shallow marine deposit in the upper part (Olaussen et al., 1984).

Seen together with the Stø Formation, the Nordmela-Stø depositional system is thought to have occurred in a quiet period with little tectonic activity and a good balance of sediment supply and subsidence (Johansen et al., 1992; Olaussen et al., 1984). The deposition of the Nordmela Formation is thought to be a part of an overall transgressive event (see Figure **4**).

Background of the thin section samples

Well 7321/8-1 was drilled in 1987 by Norsk Hydro Produksjon ASA, see Figure **2** for the location of the well. The well was abandoned the same year as a dry well with oil shows (Oljedirektoratet, 2005).

Seven cores were cut in well 7321/8-1 by Hydro in order to study the target formations. The cores from which the thin sections originate are taken from the sandy sections of the formations. The most relevant interval from 1443.5m to 1544.7m gave four cores. The intervals 2670.8m to 2678.8m and 2839m to 2847m were cored once each, and one core was taken from 3430m to 3431.4m.

Underlying the Realgrunnen Sub-Group are successions of interbedded silt/sandstones and grey shales interpreted as the Snadd Formation. Presented in Figure **5** is the interval from which samples are taken in the Snadd Formation.

Figure 5: Exposed cores from well 7321/8-1. a) Left image shows the interval 2839m-2844m of the Snadd Formatioon. a) and b) showing the mud-laminated sands of the Snadd Formation studied in thin section of the interval 2839m-2846.81m.

Cores from the interval 1443.5m to 1544.7m show sandstones with mud and clay laminations of varying frequency, with the interval 1467m to 1490m showing the largest concentration of clay laminations when observing exposed cores. The interval 1443.5m to 1467m consists of sands with moderate-low frequency of laminations and common bioturbation, and it is interpreted to contain the Stø and Nordmela Formations.

There is a boundary at 1467m (see figure **7b**) between the homogeneous sands and heavily mud/clay-laminated sands, and this facies change is interpreted as the boundary between the Nordmela and Fruholmen Formations. This heavily mud/clay-laminated sand is interpreted as the Krabbe Member of the Nordmela Formation and is found in the interval 1467m-1495m. At 1495m (see Figure **6a**) there is a transition between heavily mud/clay-laminated sands and sands with noticeably less laminations. This cleaner sand is interpreted as the Reke Member of the Fruholmen Formation and occupies the rest of the cored section of the Realgrunnen Sub-Group, being visible in cores of the interval 1495m-1544.62m. In the interval 1526.5m to 1528.3m there are large breccia-like mud clasts in the Reke Member, shown in Figure **6b**.

The interpreted boundary between the Stø and Nordmela Formations can be observed at approximately 1456.5m in Figure **7a** as the change from the seemingly massive sands of the Stø Formation to the mud-laminated sands with lenticular bedding and moderate-to-uncommon bioturbation of the Nordmela Formation. The bottom of the Nordmela Formation contains a roughly 2m tall interval of homogeneous sands.

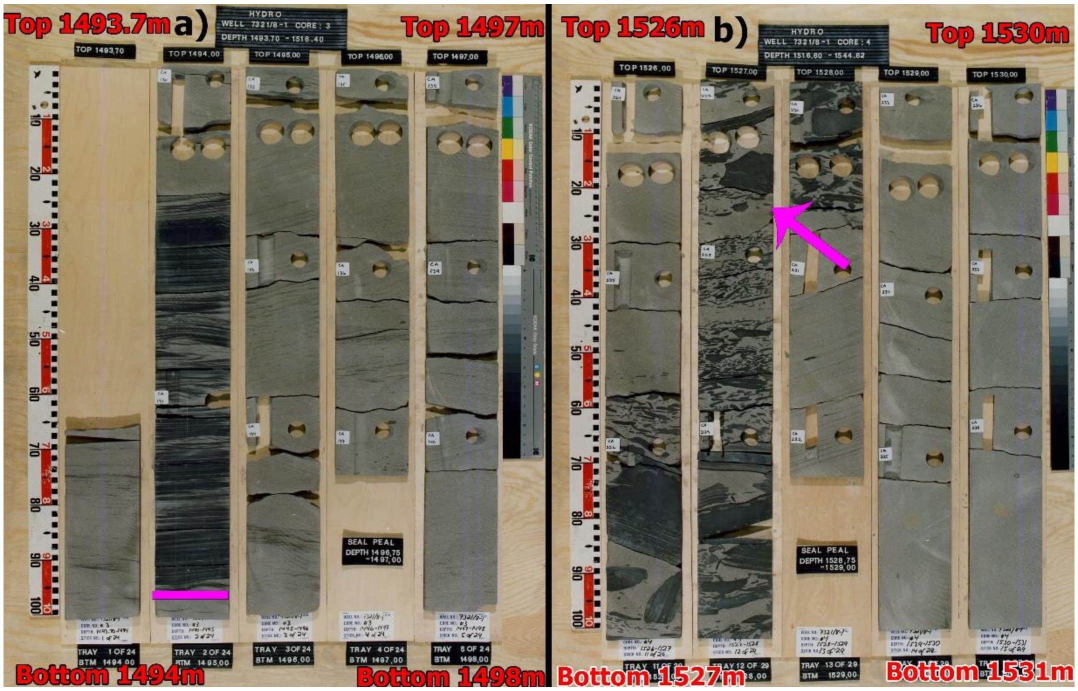

Figure 6: Exposed cores from well 7321/8-1. Purple bars represents boundary. a) Left image shows the interval 1493.7m-1498m, interpreted as the boundary between the Krabbe and Reke members in the Fruholmen Formation. b) Right image shows depth interval 1526mm-1531m, showing the breccia-like mud clasts in the middle of the Reke member of the Nordmela Formation, purple arrow for emphasis.

Figure 7: Exposed cores from well 7321/8-1. Purple bars represent formation boundaries. a) Left image shows the interval 1443m-1458m, interpreted as the boundary between the Stø and Nordmela formations. b) right image shows depth interval 1465.5m-1470m, interpreted as the boundary between the Nordmela and Fruholmen formations.

A total of twelve new thin sections were prepared on 2015-05-18 from the Nordmela, Fruholmen and Snadd Formations. The thin sections provided for this project have been assigned depths in meters without the distinction between MD (measured depth) or TVDSS (true vertical depth subsea).

The thin section samples have also been assigned formation names, with the boundary between the Fruholmen and Nordmela Formations appearing to be at 1467m. By comparing the depths given on the thin sections to the well logs supplied with the well report (see Figure **9** below) one can correlate with the Kapp Toscana Group boundary and conclude that the formation depths given on the thin sections are given in measured depths. This would correspond to the boundary given by the MD in the well report in figure **8**, so the author therefore assumes that the depths marked on the thin sections are also given in MD.

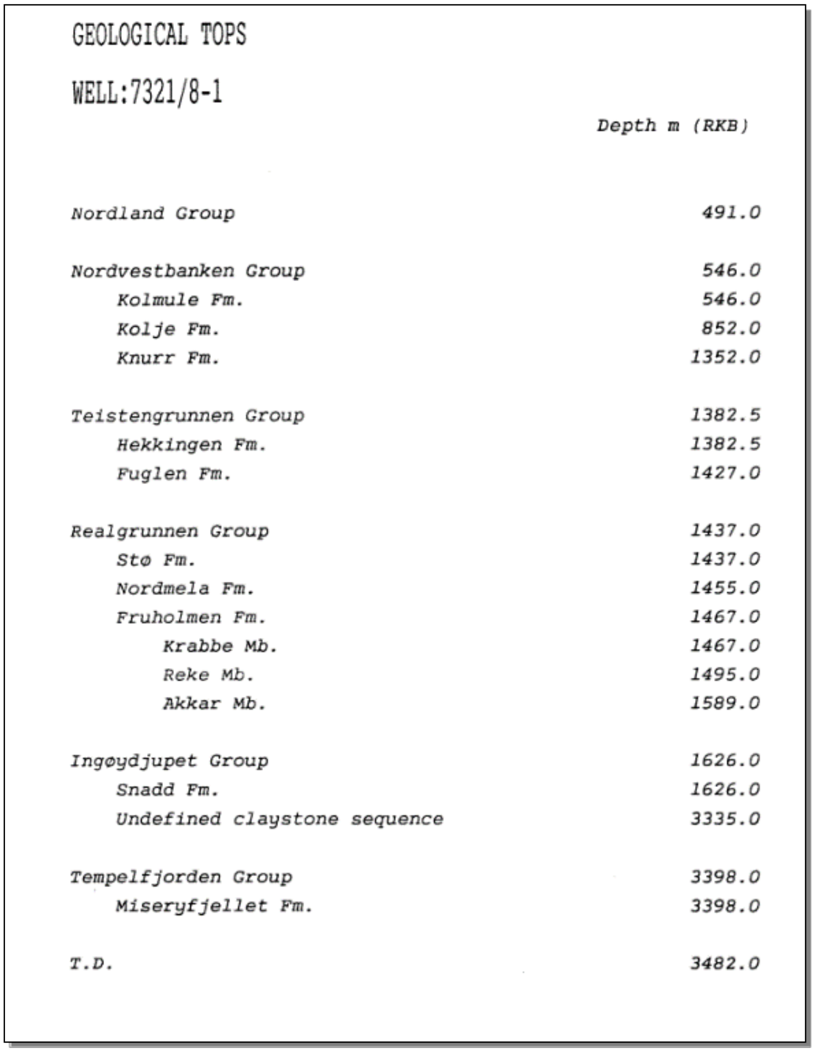

GEOLOGICAL TOPS

WELL:7321/8-1

	Depth m (RKB)
Nordland Group	491.0
Nordvestbanken Group	546.0
Kolmule Fm.	546.0
Kolje Fm.	852.0
Knurr Fm.	1352.0
Teistengrunnen Group	1382.5
Hekkingen Fm.	1382.5
Fuglen Fm.	1427.0
Realgrunnen Group	1437.0
Stø Fm.	1437.0
Nordmela Fm.	1455.0
Fruholmen Fm.	1467.0
Krabbe Mb.	1467.0
Reke Mb.	1495.0
Akkar Mb.	1589.0
Ingøydjupet Group	1626.0
Snadd Fm.	1626.0
Undefined claystone sequence	3335.0
Tempelfjorden Group	3398.0
Miseryfjellet Fm.	3398.0
T.D.	3482.0

*Figure 8: The formation depths as given in the well report for well 7321/8-1. RKB = Rotary Kelly Bushing. Extracted from the document "*1070_01_WDSS_General_Information" *(Oljedirektoratet, 2005)*

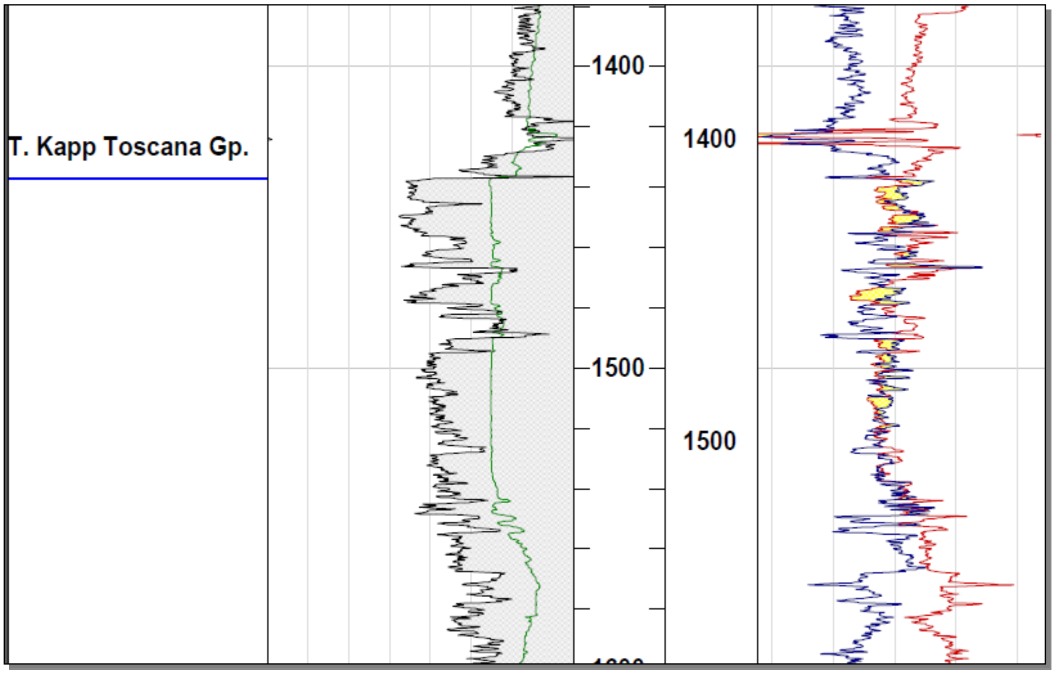

Figure 9: Well log of well 7321/8-1 in the interval where most of the samples are taken. Left depth bar is measured depth, right depth bar is true vertical depth subsea (Oljedirektoratet, 2005).

Previous work on the Sub-Group

The previous work on the Realgrunnen Sub-Group has mainly been focused on the Stø Formation, as this formation has been proven to be a reservoir which contains producible hydrocarbons. The Stø Formation is also being used for CO_2-storage during production (Statoil, 2013). The Norwegian Petroleum Directorate (NPD or Oljedirektoratet) has released several bulletin reports which outline general geological and sedimentological characteristics of the Fingerdjupet Sub-Basin and the formations in the Realgrunnen Sub-Group (Oljedirektoratet, 2014a, 2014b).

Olaussen et al (1984) have looked into the depositional environment and diagenesis of the Stø and Nordmela Formations in the Troms 1 area (Olaussen et al., 1984), which has been a useful reference in this paper. Walderhaug and Bjørkum (2003) have written about stylolites in the Stø Formation in the southern Barents Sea (Walderhaug & Bjørkum, 2003), which is relevant for this paper as stylolites have been observed during microscopy work. Vorren et al (1991) have discussed the erosion in the western Barents Sea (Vorren et al., 1991), and Ohm et al (2008) have described the uplift episodes of the Barents Sea (Ohm et al., 2008). Marello et al (2013) have discussed the basement evolution of the Barents Sea based on gravimetric and magnetic data (Marello et al., 2013).

Methods

Thin section analysis

The petrographic samples studied in this text are polished thin sections made from core samples at a depth interval of 1460.55m to 2846.70m in well 7321/8-1. The thin sections were investigated by using a transmitted light microscope, primarily at 5x (scale bar 500 µm), 10x (scale bar 250 µm) and 20x (scale bar 125 µm) optical zoom. Detrital grains, matrix and diagenetic material (both grains and cement) are presented along with photographs taken with ProgRes microscope software. Photographs of individual grains are shown as well as photographs showing evidence of diagenetic reactions.

In addition, modal analysis by point counting was performed through use of the Pointscan software and an electro-mechanical microscope slide stepper machine manufactured by Pelcon. Each counting consisted of 300 points in 6-row/50-column configuration. Point counting was performed on all thin sections except of the two from the Snadd Formation because the grains in this formation are very small and contain near-zero porosity due to carbonate cementation. Care was taken to use representative areas of the sections while point counting, especially with clay-laminated sections in which the laminations were partly included in the counting to give a representative clay content of the thin section – see Figure **10** for an example. Grains were counted by using the stepper motor and noting which grain the cross wire landed on for each step.

The author had trouble telling apart quartz and non-twinned albite during point counting, which became apparent when significant quantities of albite was observed during EDS analysis while very little plagioclase was recorded during point counting. The amounts of quartz and plagioclase quantified through point counting is therefore an error source and it is reasonable to assume some of the albite has been mistaken for quartz.

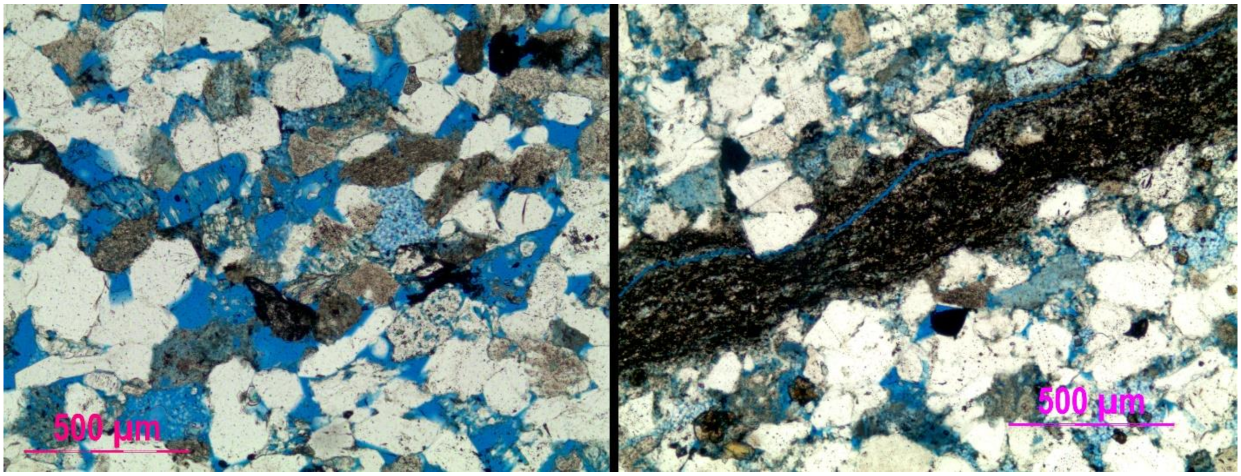

Figure 10: Examples of areas and scale used during point counting. Left image shows typical sandstone photo sued, right image shows typical image used when clay laminations are present. Scale bar shows 500μm, representing 5x optical zoom.

Porosity determination

The porosity of the thin section samples has been quantified to determine the reservoir quality of the formation sandstones. The two main components of reservoir quality are porosity and permeability. The porosity of the thin sections was quantified by two separate methods:

By use of the software KLONK Image Measurement: The thin sections have been treated with dye so the porosity is coloured blue in the photographs, which aided the porosity estimation process. Each pore that showed non-clay porosity was outlined by hand, after which the cumulative area of the outlines was calculated as a percentage of the total area of the thin section photograph. The porosity given is the porosity which could hold hydrocarbons, like intergranular porosity. The micro-porosity of clay has not been included in the given porosity, which means that the porosity presented here will most likely be lower than the total porosity obtained by laboratory determination of porosity. Photos used for acquiring area measurements were taken from two opposite corners of the thin sections, unless clay laminations were present in the thin section and should be included for accuracy. The photos used were at the same scale as shown in Figure **10**, with optical zoom of 5x.

Using point counting: Porosity was quantified during the point counting modal analysis and is included in Table **2**. Porosity for the Snadd Formation has not been quantified through point counting, only by image measurement with the KLONK software.

Scanning Electron Microscope (SEM) – Backscatter Electron (BSE) imaging

BSE imaging was performed in order to tell heavy and light minerals apart during SEM analysis.

The thin sections were carbon-coated with the assistance of Mr. Kjetil Eriksen at the Institute of Geoscience and Petroleum of NTNU. This was done to increase the electrical conductivity of the thin section surfaces with to optimise pictures from the SEM.

Thin sections were placed on a rotary pedestal inside of a vacuum chamber. Two rods of carbon were then sharpened and pressed together with a spring-clamp, and the air was then evacuated from the chamber and the rotary motion of the pedestal was initiated. Once the near-vacuum was stable, electrical current was sent through the carbon road tips for six seconds with the result of carbon particles being ejected into the chamber and covering the thin sections.

The prepared thin sections were inserted into a Hitachi SU6600 Scanning Electron Microscope. Electron backscatter imaging was used to display images of the samples

In this method, the minerals are distinguishable in terms of average atomic densities with heavy minerals appearing brighter, and lighter minerals appearing darker. Minerals with higher average atomic numbers reflect electrons more strongly by elastic scattering, leading to the higher intensity of the heavy minerals in the imaging.

Scanning Electron Microscope (SEM) – Energy Dispersive X-ray Spectroscopy (EDS)

EDS was performed to identify minerals based on their atomic composition.

EDS works by the electron incidence beam exciting X-rays in the mineral’s atoms, displacing electrons in the inner shells. These X-rays vary in strength between different elements, yielding X-ray signatures which can be used to assume elemental makeup of the target mineral. There were hundreds of EDS mineral-spectra acquired during this study, of which spectra representative for each mineral have been selected and are presented in Appendix **B** and in certain places in the text itself where they have been relevant. EDS was performed through the ESPRIT software suite, with backscatter imaging serving as a reference image for the spectra obtained. Roughly 30 to 40 spectra were obtained per thin section sample to have a comprehensive knowledge of the minerals present in the formations.

Operating parameters used were 15kV acceleration voltage and 10s real detection time per spectrum.

Scanning Electron Microscope (SEM) – Cathodoluminescence (CL)

The cathodoluminescence aids in distinguishing and quantifying the amount of quartz cement which is the main porosity destroying mechanism of sandstones at the depths investigated. Authigenic and detrital quartz show different intensities under CL due to detrital quartz often being inherited from igneous rocks. The igneous environments have high temperatures which provide higher levels of trace cations and lattice defects (Houseknecht, 1991). Authigenic quartz forms at much lower temperatures, leading to fewer lattice defects and trace cations. This enables imaging which can tell authigenic and detrital quartz apart.

Operating parameters used were 20kV acceleration voltage and 40s image capture time.

Cathodoluminescence photos are used to calculate the percentages of diagenetic quartz cement overgrowths and detrital quartz, such as shown in Figure **11** below. The KLONK Image Measurement software was used to obtain the relative areas of the grains and their detrital cores. For each thin section, two or more photo sets were taken with SE/BSE and CL, and the areas of detrital grains and cement were quantified. Five measurements were made per photo set, and the results were averaged and can be seen in Table **3**. The photo pairs can be seen in Appendix **A**. Grains selected for measurement were selected based on their brightness due to the contrast weaknesses of less bright grains in CL.

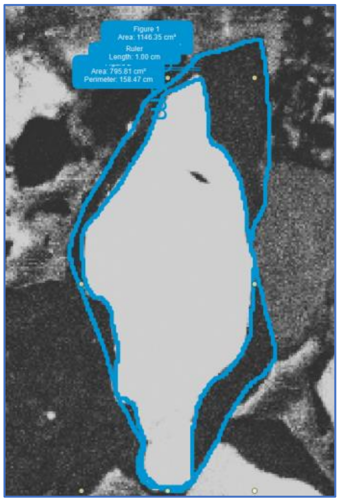

Figure 11: CL photo example showing the quantification of quartz cement using the KLONK Image Measurement software. Blue lines are measuring lines.

Results

Results of petrography

The sandstone petrography of the formations is presented based on the thin sections and illustrated by pairs of photographs in plane polarized and cross polarized light. The author will expand upon detrital grains, matrix and diagenetic minerals. Porosities, grain sizes and sorting is given in Table 1 below.

Organic matter is observed in all formations, with the highest concentration in the Fruholmen Formation. The organic matter is dark red to deep brown in appearance under optical plane polarized light. Titanium dioxides are present in all formations, with titanium enrichment in volumes of extensive chemical dissolution. The titanium dioxides are assumed to be rutile because of rutile's stability (Hanaor & Sorrell, 2011). Trace amounts of zircon are also present in all formations.

TABLE 1: POROSITY FROM KLONK IMAGE MEASUREMENT POROSITY ANALYSIS IN ADDITION TO GRAIN SIZE AND SORTING OBSERVED IN THE THIN SECTIONS.

DEPTH [M]	FORMATION NAME	POROSITY	GRAIN SIZE	SORTING	ROUNDING
1460.55	Nordmela	7.2%	Very fine sand	Moderately sorted	Subangular
1460.8	Nordmela	10.6%	Medium sand to fine sand	Well sorted	Subangular
1460.85	Nordmela	6.0%	Fine sand to very fine sand	Well sorted	Subangular
1463.7	Nordmela	12.2%	Medium sand	Very well sorted	Subhedral (heavily quartz cemented)
1468.9	Fruholmen [Krabbe Member]	2.1%	Medium sand to fine sand	Well sorted	Subangular
1487.95	Fruholmen [Krabbe Member]	6.20%	Very fine sand	Moderately sorted	Angular.
1495.44	Fruholmen [Reke Member]	4.4%	Fine sand	Moderately sorted	Very angular
1513.41	Fruholmen [Reke Member]	11.5%	Fine sand	Well sorted	Poorly rounded
1538.32	Fruholmen [Reke Member]	4.60%	Fine sand	Well sorted	Sub-angular
1543.02	Fruholmen [Reke Member]	3.30%	Very fine sand	Moderately sorted	Sub-angular
2840.5	Snadd	1.0%	Very fine sand - Coarse silt	Moderately sorted	Very angular
2846.7	Snadd	2%	Fine sand	Moderately sorted	Very angular

Classification of formations in Dott-diagram

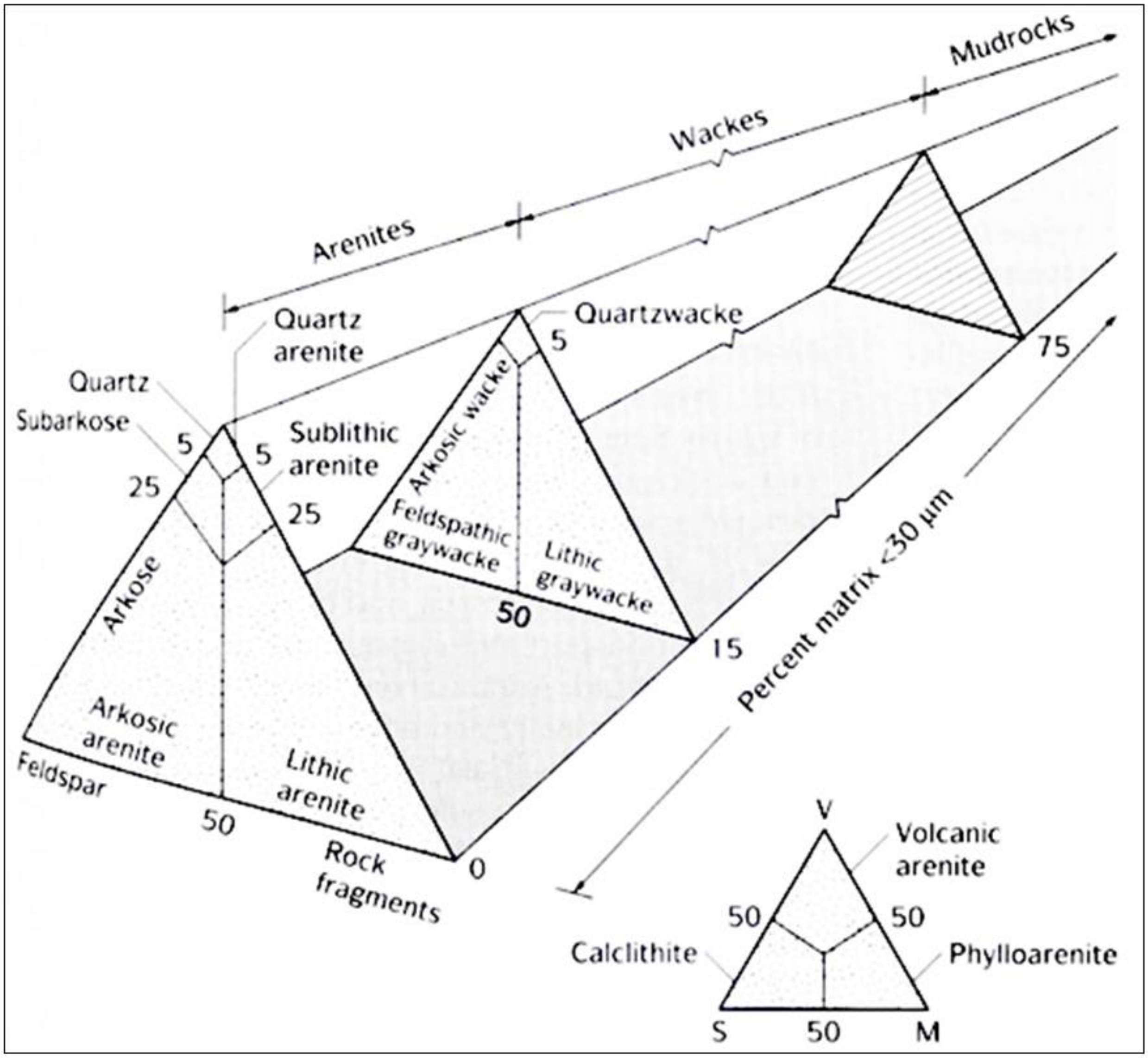

Figure 12: The Dott classification ternary diagram for sandstones (Dott Jr, 1964)

Table 2: Point counting data with porosity and grain volumes. Note that the grain volumes are recalculated as percentages of grain volume excluding porosity.

Porosity	Depth[m]	Quartz	Clay	Carbonates	K-feldspar	Organics	Plagioclase	Pyrite	Muscovite
14%	**1460.55**	58.7%	18.1%	11.2%	2.7%	2.3%	0.8%	5.0%	1.2%
16%	**1460.8**	59.2%	30.2%	3.1%	2.7%	0.0%	3.1%	1.2%	0.4%
10%	**1460.85**	59.6%	23.0%	3.7%	2.2%	0.7%	1.9%	7.0%	1.9%
13%	**1463.7**	93.0%	5.8%	0.8%	0.4%	0.0%	0.0%	0.0%	0.0%
5%	**1468.9**	71.9%	22.6%	1.7%	1.0%	1.0%	0.3%	1.4%	0.0%
13%	**1487.95**	56.5%	28.1%	0.0%	4.2%	5.8%	0.8%	3.5%	1.2%
10%	**1495.44**	56.4%	30.8%	2.6%	1.8%	1.5%	0.7%	5.9%	0.4%
11%	**1513.41**	54.9%	27.8%	7.1%	2.3%	0.0%	0.8%	6.0%	1.1%
7%	**1538.32**	53.4%	24.4%	16.3%	1.4%	0.0%	2.5%	1.8%	0.4%
6%	**1543.02**	67.8%	13.4%	13.4%	0.0%	0.0%	1.8%	2.1%	1.4%

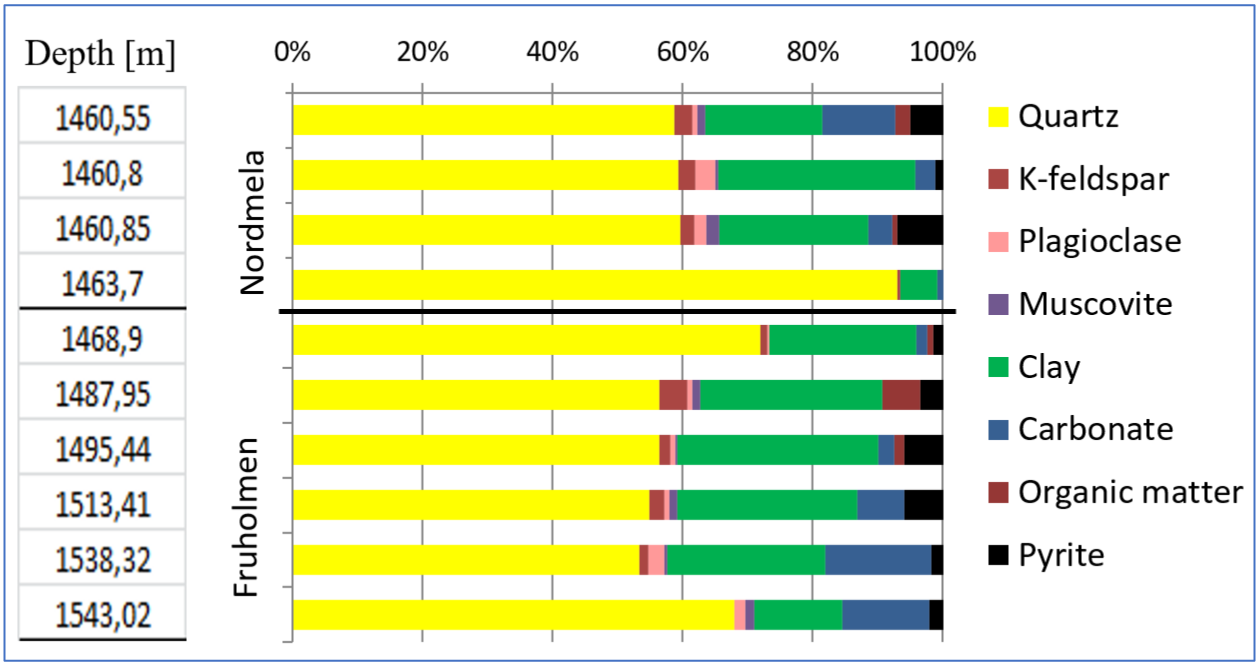

Figure 13: A visualisation of the data presented in Table 2.

TABLE 3: DETRITAL GRAIN AND CEMENT AS PERCENTAGE OF TOTAL QUARTZ GRAIN VOLUME.

Depth [m]	**Detrital grain [%]**	**Cement [%]**
1460.55	67.2	32.8
1460.8	65.3	34.7
1460.85	64.5	35.5
1463.7	69.4	30.6
1468.9	59.1	40.9
1487.95	57.5	42.5
1495.44	73	27
1513.41	60	40
1538.32	70.8	29.2
1543.02	51	49
2840.5	74.3	25.7
2846.7	70.1	29.9

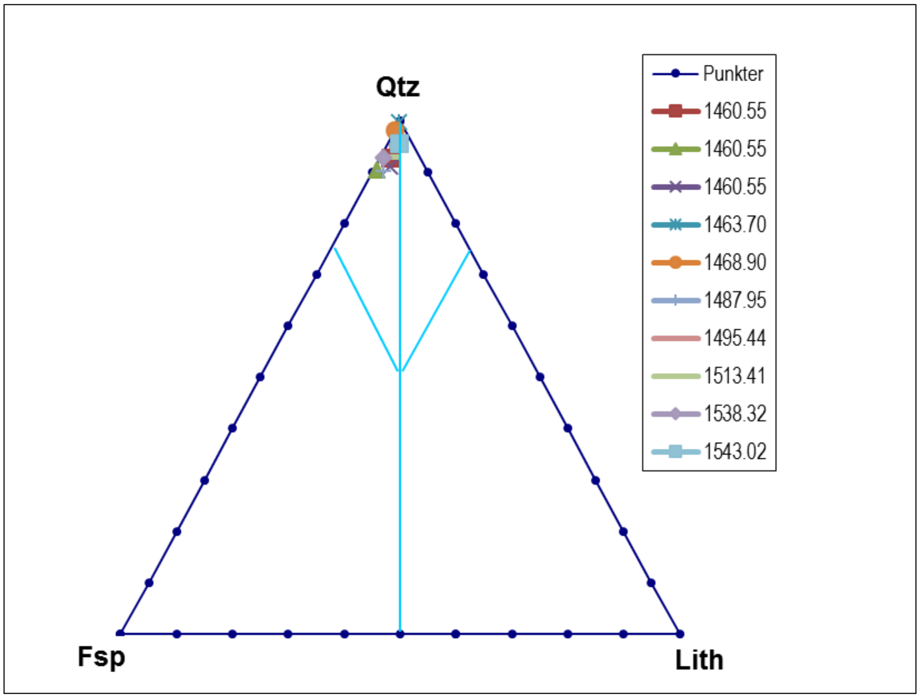

FIGURE 14: QFL-DIAGRAM USING THE DATA IN TABLE 2 FOR DOTT-CLASSIFICATION OF SILICICLASTIC ROCKS.

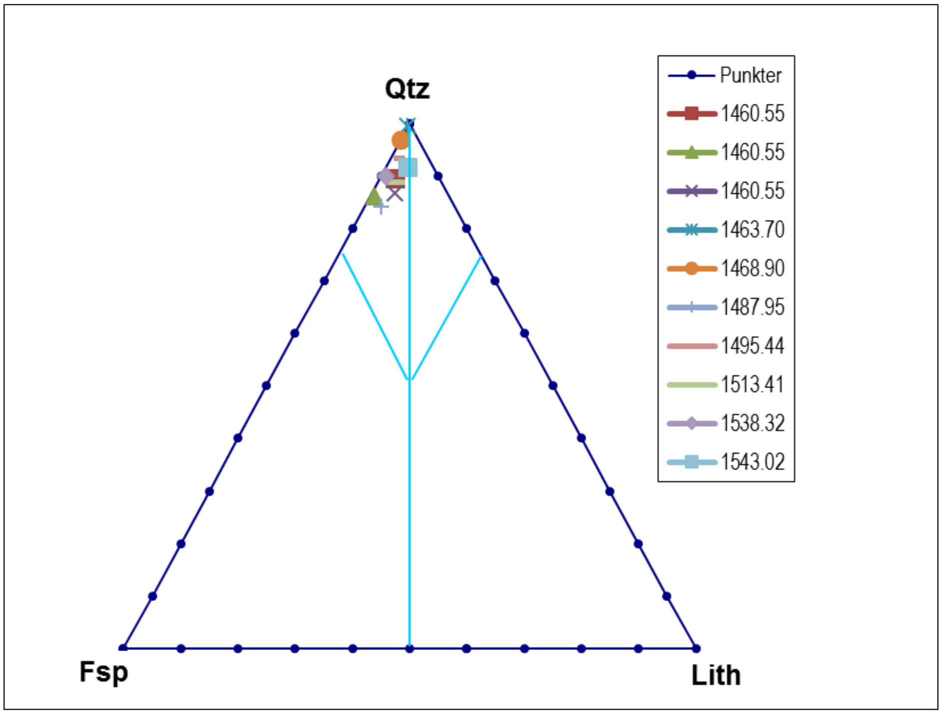

FIGURE 15: QFL DIAGRAM USING RECALCULATED VALUES TO CORRECT FOR QUARTZ CEMENT VALUES LISTED IN TABLE 3.

For use in the QFL-diagram, the following definitions were used when applying the data from modal analysis:

Quartz: Quartz and chert, both counted as quartz during point counting. The chert should have been classified as a rock fragment, but unfortunately the point counting machine used only allowed for nine different types of minerals or substances to be counted.

Feldspar: K-feldspar and plagioclase were counted as feldspar.

Lithics: Muscovite. No other lithics of significant size except for chert were observed in the sandstones. Pyrite is interpreted to be diagenetic.

Matrix: Organic matter is interpreted to be matrix.

Most of the thin sections studied in the Nordmela and Fruholmen Formations have a mineral composition which corresponds to quartz arenite or sub-arkose in the Dott classification (see Figures **12, 14** and **15**). The kaolinite, illite, calcite and siderite are considered to be mainly diagenetic in origin, and therefore the sandstones are classified as arenites instead of wackes even though the clay and carbonate percentages from Table **2** might suggest otherwise. These classifications are a product of the count pointing data (Table **2**) and the quartz cement data (Table **3**), and should be treated with scepticism due to the plagioclase/quartz counting error outlined in the methods section. It is reasonable to assume that the actual classifications of these rocks are slightly more arkosic than the point counting data would imply.

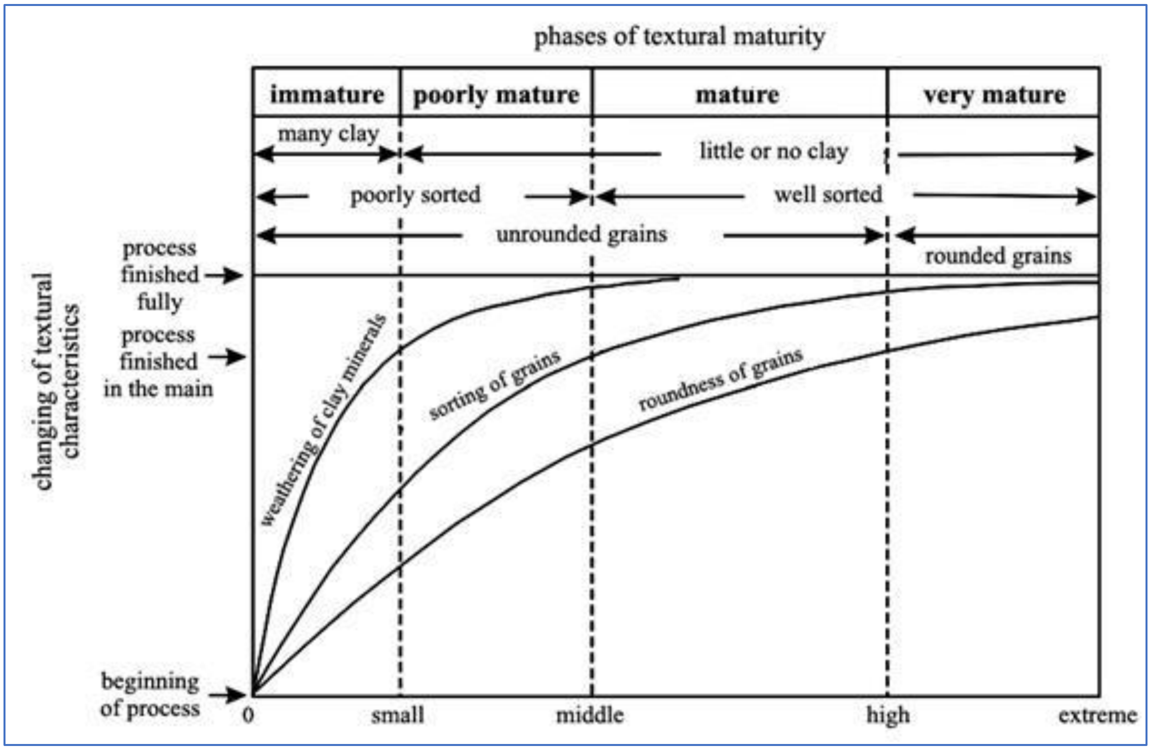

FIGURE 16: PHASES OF TEXTURAL MATURITY BASED ON ROUNDING, SORTING AND REMOVAL OF CLAY. BASED ON FOLK (1951) WITH MODIFICATIONS (FOLK, 1951).

The textural maturity of the sandstones is considered to range from poorly mature to mature in Folk's textural maturity chart (Figure **16**) based on the data from Tables **1** and **2**. The sorting is generally good, with less rounding visible due to quartz cementation and clay content ranging from 15%-30% in most of the sandstones. The sample from 1463.70m has rounded detrital grains (see Appendix **A**) but quartz cementation has made them more angular in-situ. The 1463.70m sample also has a very low clay content of 5.8%, and the author would classify the sample as very mature.

Formation petrography

Nordmela Formation

Detrital grains

Among the detrital grains observed in the samples we find a majority of quartz along with small quantities of K-feldspar, plagioclase and muscovite.

Quartz: The quartz grains appear to be the dominant mineral in all formations, showing first order interference colours in cross polarized light and being colourless to slightly beige in plane polarized light. The clear majority of the quartz grains are monocrystalline grains which show uniform or undulose extinction. A few rare polycrystalline grains show schistosity with sutured and concave-convex grain contacts (see Figure **19)**. These grains are interpreted to be chert and therefore classified as rock fragments in a QFL-diagram.

K-feldspar: Most grains are partly or fully dissolved, and some of the larger grains show microcline tartan-twinning (see Figure **17** below). Most K-feldspar grains show no twinning or are too dissolved to show original twinning. Undissolved grains show the same optical qualities as quartz with the exception of undulose extinction, although some grains are dirty and contain impurities which darken the grains.

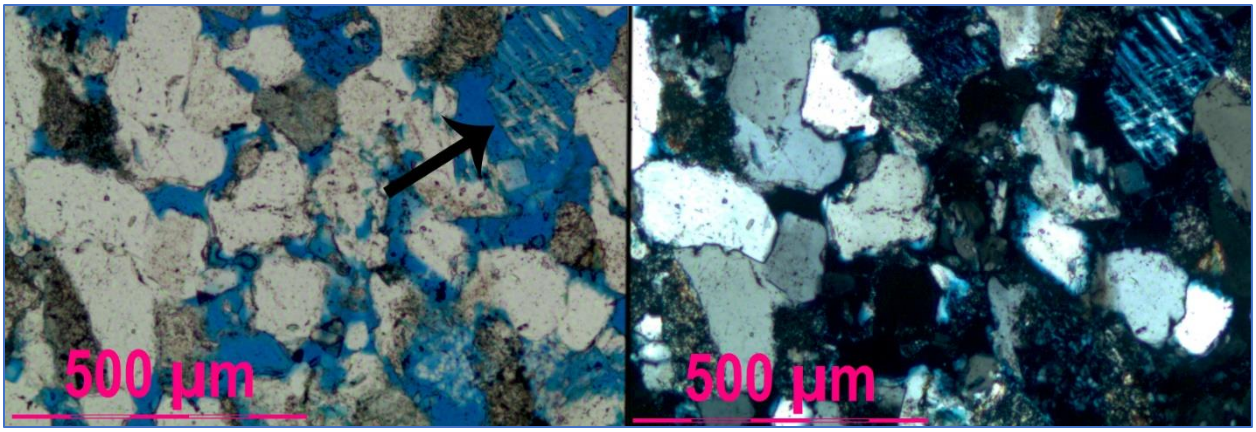

Figure 17: Thin section photo of partly dissolved microcline in the upper right corner. plane polarized light (left) and cross polarized light (right). Depth = 1460.80m, Nordmela Formation.

Plagioclase: Plagioclase grains show polysynthetic twinning under cross polarized light and is colourless in plane polarized light. Some grains are partly dissolved with parts of the grains being replaced by illite.

Muscovite: Muscovite mainly appears as long thin grains, with most of the grains showing mechanical deformation (see Figures **18** and **20**). Colourless in plane polarized light and shows bright second and third order interference colours in cross polarized light.

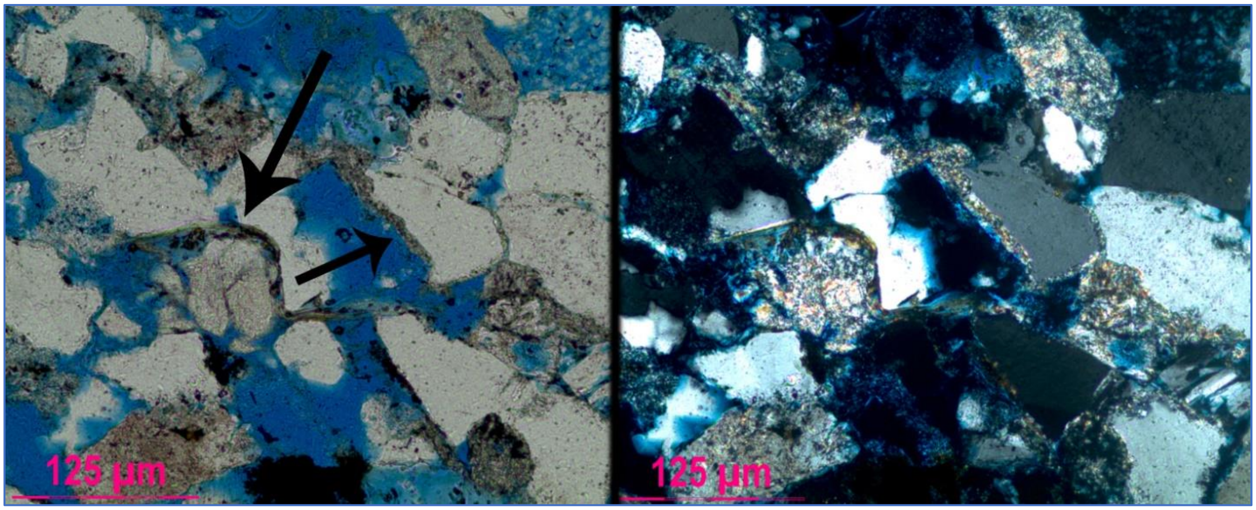

Figure 18: Thin section photograph showing deformed muscovite and illite grain coatings. Nordmela Formation, depth = 1460.80m.

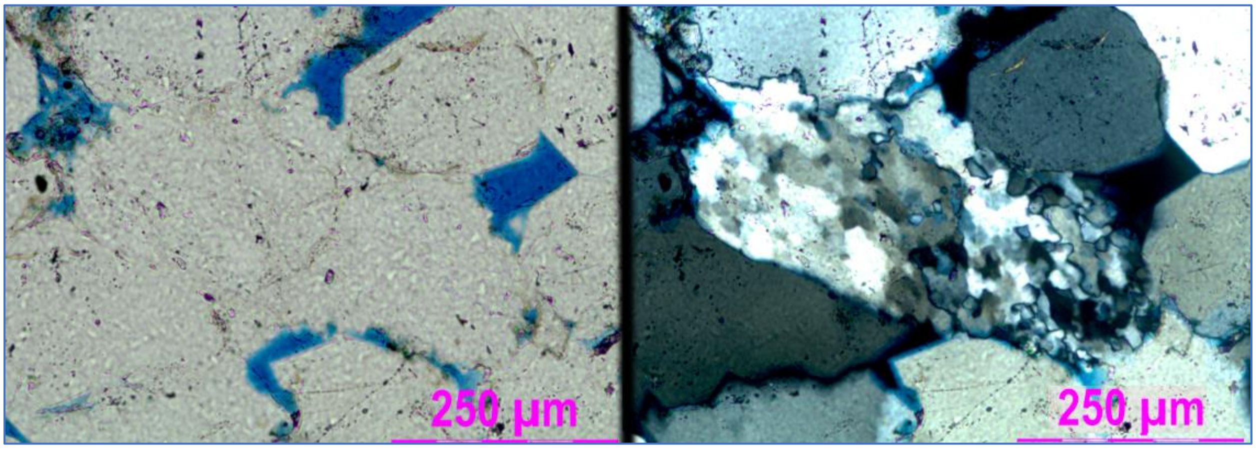

Figure 19: Thin section photos of quartz grain boundaries and schistose quartz in the centre. The schistose quartz is assumed to be a rock fragment as no other quartz grains in the formation exhibits polycrystalline patterns. Nordmela Formation, depth = 1463.70m.

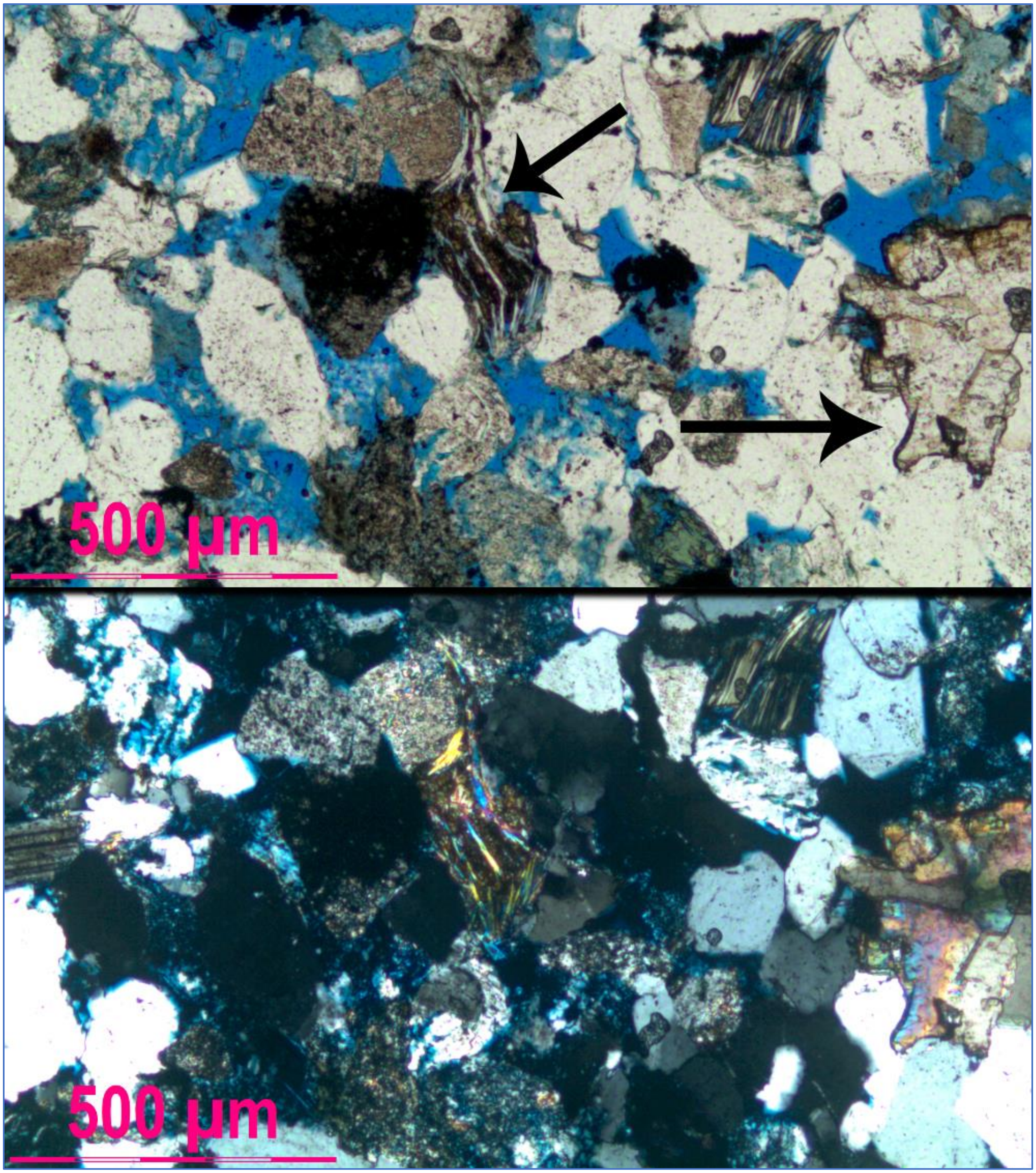

Figure 20: Thin section photos of deformed muscovite (centre) and carbonate cement (right). Nordmela Formation, depth = 1460.80m.

Matrix

Clay aggregates: Clay aggregates are common in the Nordmela Formation, and in some grains forming dust rims (see Figure **21**). The clay aggregates show the bright first order interference colours associated with illite or sericite and is grey to brown in plane polarized light.

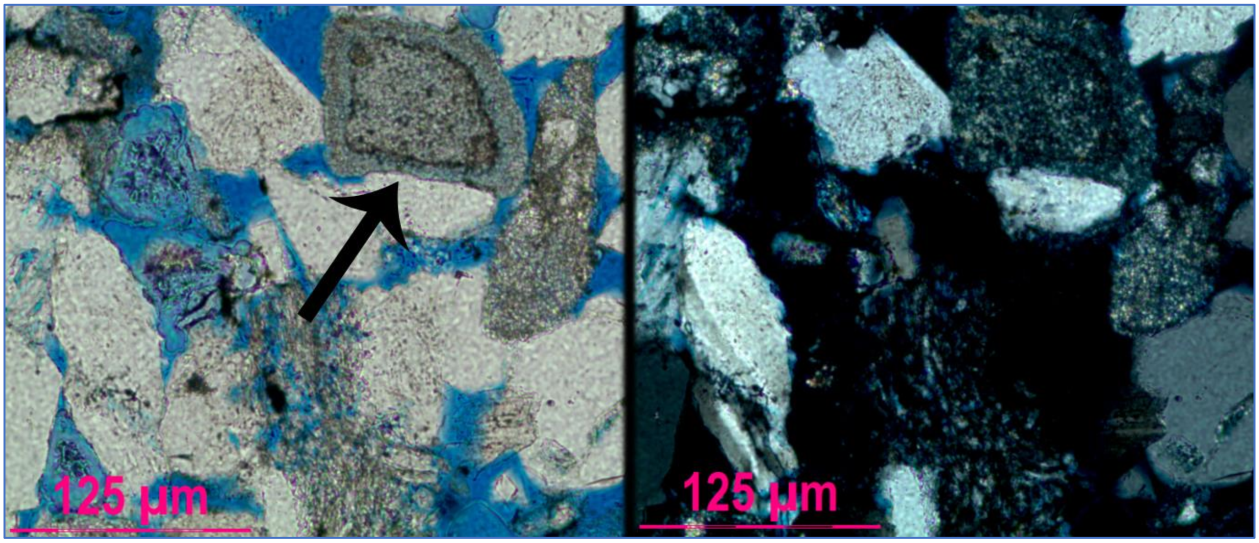

Figure 21: Thin section photos showing clay aggregate in upper right corner with dust rim inside the grain. Depth = 1460.80m, Nordmela Formation.

Diagenetic minerals

Carbonate cement: Pore filling carbonate cement is common, with calcite being the dominant mineral (see Figure **20**). Some cement grows on euhedral quartz, appearing to have grown after quartz cementation. The calcite is mostly colourless in plane polarized light, although it is slightly darker than the quartz or feldspars and it shows much higher relief. Shows bright 4th order interference colours in cross polarized light.

Quartz cement: In the mature sequence seen in the thin section sample for 1463.70m, quartz cementation is clearly visible as the dust rims in the grain outlines the original grain (see Figure **22**). Subhedral shapes are also present as a result of this cementation. Otherwise quartz cementation is not apparent in the rest of the Nordmela Formation without the use of cathodoluminescence as the quartz growths are syntaxial and optically continuous with the original grains.

Albite cement: Some K-feldspar grains show overgrowths of albite cement (identified through use of SEM), see Figure **22**. This albite does not show plagioclase twinning and looks like K-feldspar or quartz in optical microscope.

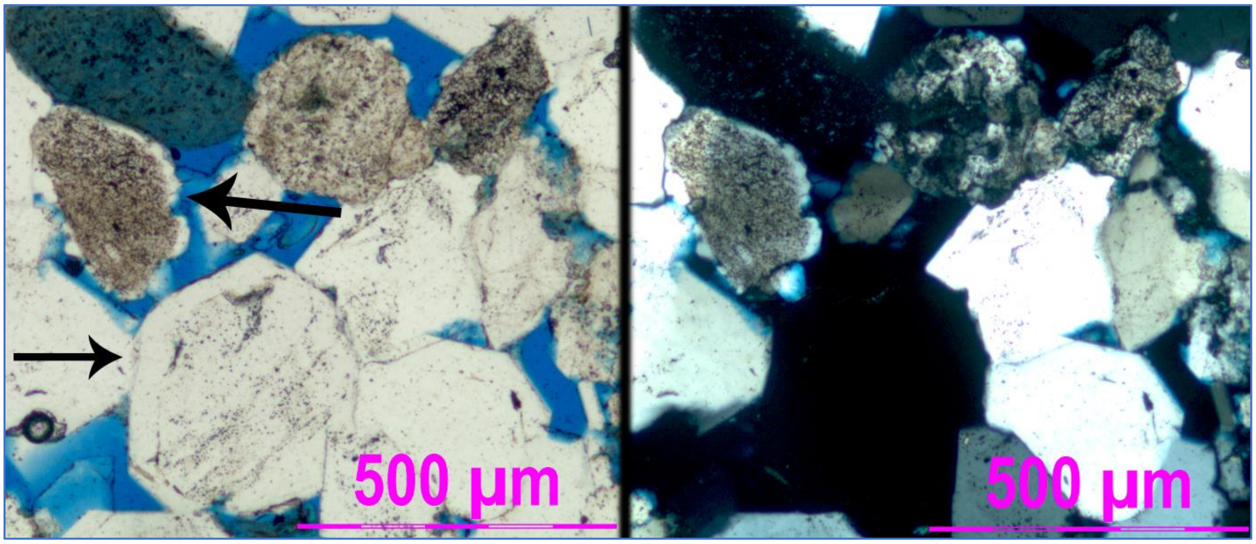

Figure 22: Thin section photos showing quartz cementation on quartz grains and albite cement on K-feldspar. Nordmela Formation, depth = 1463.70m.

Kaolinite: Replacement of K-feldspar and muscovite grains with kaolinite is visible in all the thin sections in the Nordmela Formation. Kaolinite appears similar to chert at low magnification, while the relief of the booklet-contacts in kaolinite appears as small black needles at high magnification (see Figures **23**). Colourless in plane polarized light and first order interference colours in cross polarized light.

Illite: Replacement of unstable grains with illite is particularly visible in cross polarized light as brightly coloured needles inside plagioclase in cross polarized light (see Figure **23**). Illite also occurs as grain coatings on quartz (see Figure **18**) and as pore filling matrix.

Pyrite: Pyrite occurs as both individual crystals and as cement, with clusters of smaller crystals as cement. The pyrite is opaque in both plane polarized and cross polarized light and is quite difficult to tell apart from siderite in optical microscope.

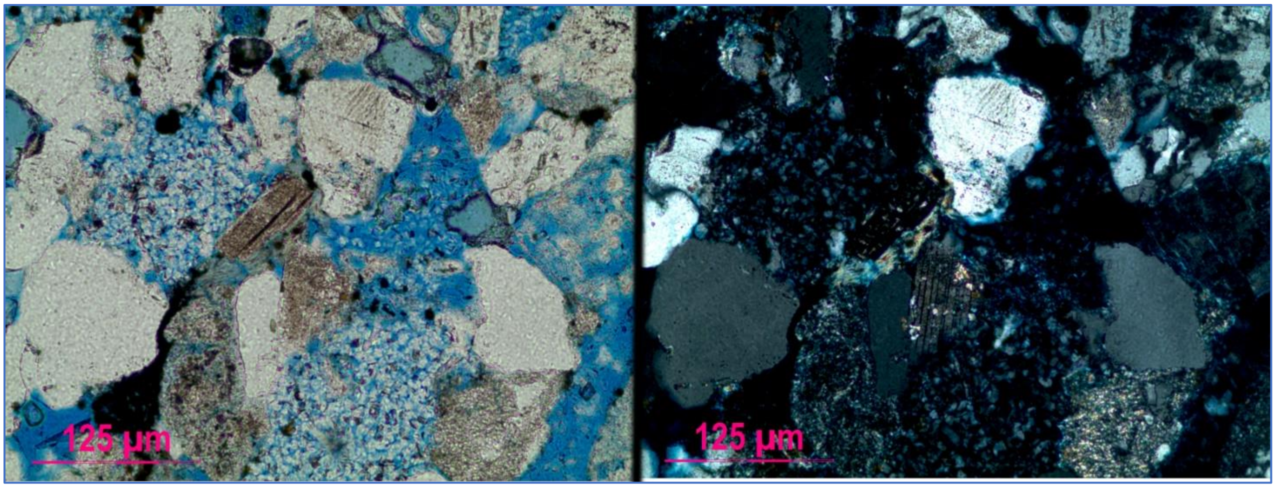

Figure 23: Diagenetic kaolinite replacing detrital grains (presumably K-feldspar). Illitization of plagioclase grain (centre). Depth = 1460.85m, Nordmela Formation.

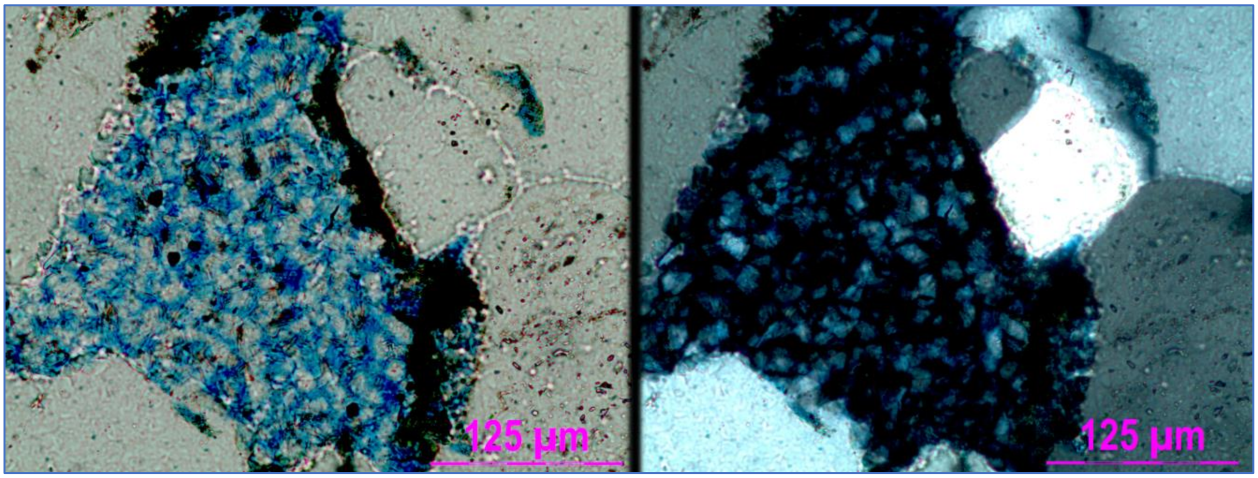

Figure 24: Thin section photo of diagenetic kaolinite having replaced what is presumably a feldspar grain. Note organic matter at the grain's right-side edge. Nordmela Formation, depth = 1463.70m.

Fruholmen Formation

Detrital grain

Among the detrital grains observed in the Fruholmen Formation samples we find the majority of the detrital grains are quartz, although slightly less than in the Nordmela Formation. In addition to the quartz there are small quantities of detrital K-feldspar, plagioclase, and muscovite.

Quartz: Monocrystalline quartz grains are the dominant mineral in the Fruholmen Formation, with little to no polycrystalline grains visible in optical microscopy. Grain sizes are variable dependent on the distance from stylolites in the Fruholmen Formation, with larger grains closer to the stylolites. The quartz has the same optical qualities as in the Nordmela Formation.

K-feldspar: K-feldspar grains in various stages of dissolution are present in the Fruholmen Formation, with more observed kaolinite-replacement than in the Nordmela Formation. The K-feldspar has the same optical qualities as in the Nordmela Formation.

Plagioclase: Plagioclase in various stages of dissolution are present in the Fruholmen Formation (see Figure **25**), with the grains showing twinning.

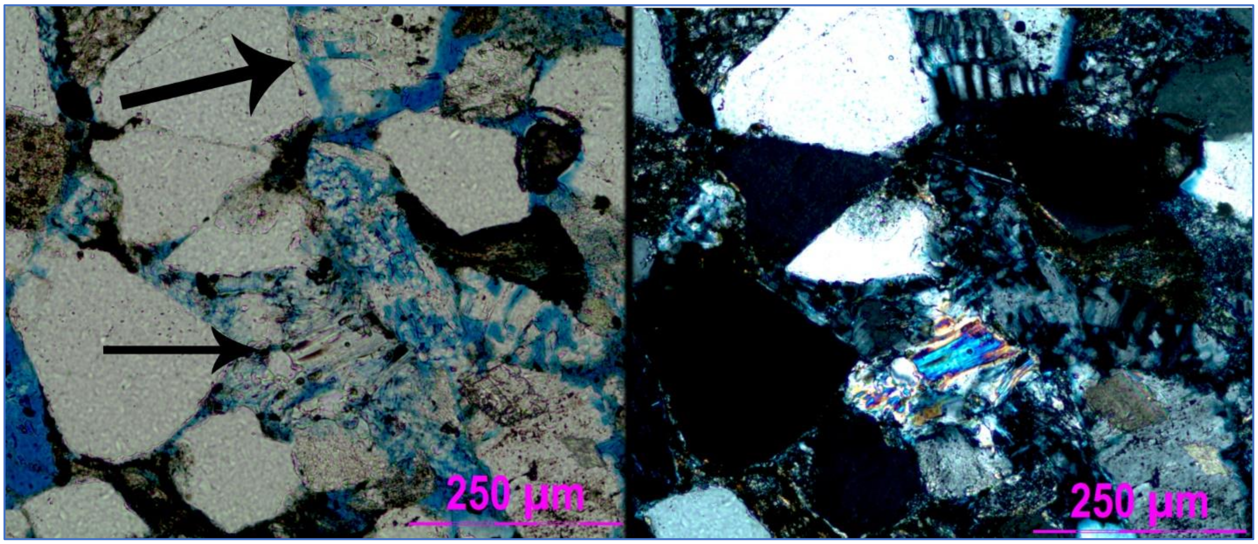

Figure 25: Thin section photograph of plagioclase (top) and K-feldspar (middle) being partly dissolved. Fruholmen Formation, depth = 1495.44m.

Muscovite: Grains of muscovite are present as both freestanding largely intact grains showing mechanical deformation, and as largely dissolved grains in stylolites (see Figures **26** and **27).**

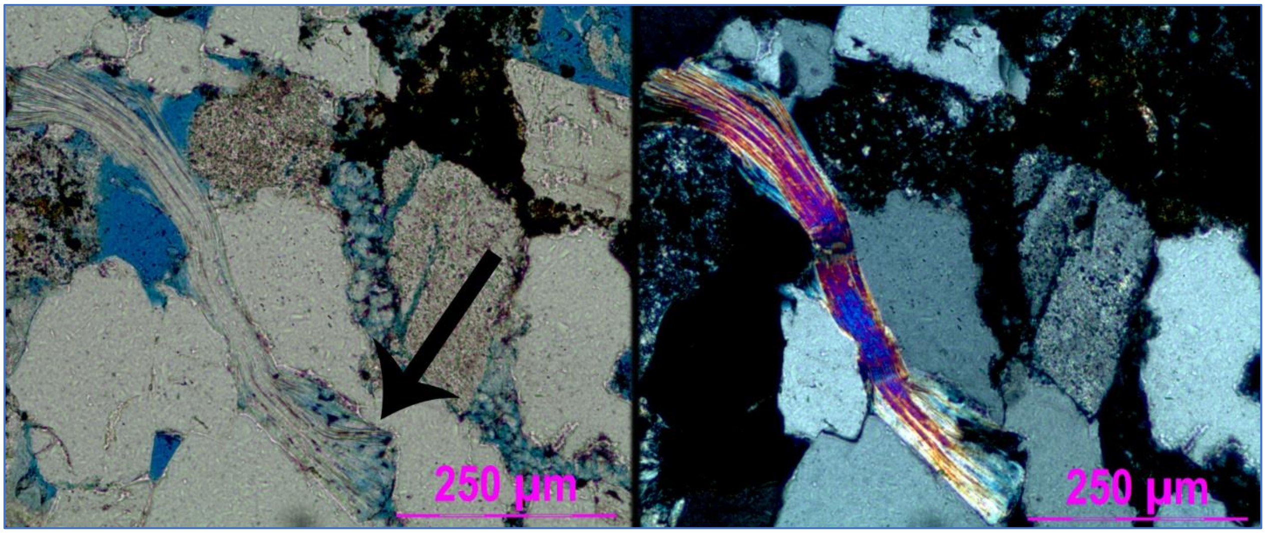

Figure 26: Thin section photograph of deformed muscovite and pore-filling kaolinite/illite. Fruholmen Formation, depth = 1495.44m.

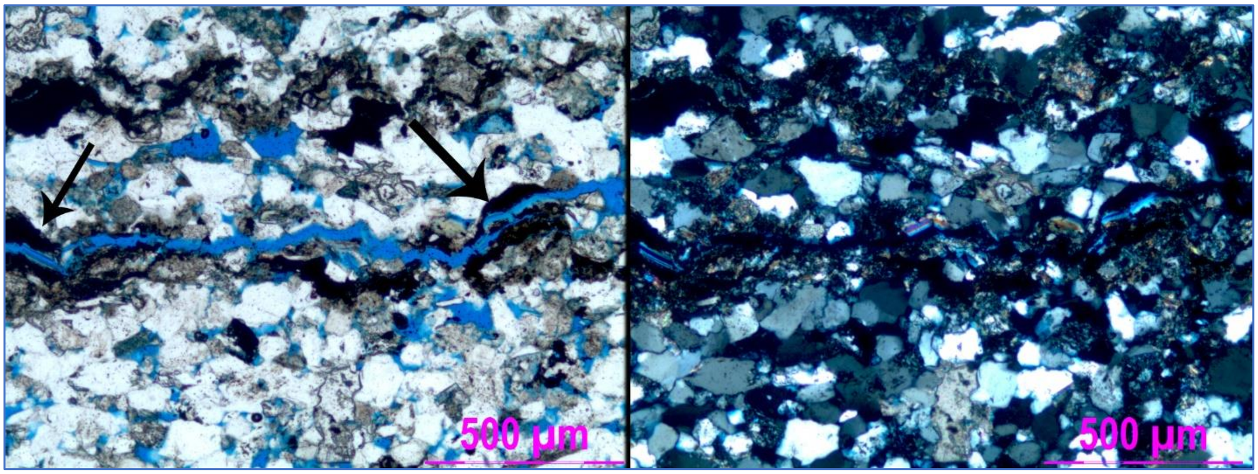

Figure 27: Thin section photograph showing stylolites with dissolved muscovite in the centre and pyrite grains and organic matter along the lamination. Fruholmen Formation, depth = 1543.02m.

Matrix

Clay laminations: Fine-grained laminations are observed in the Fruholmen thin sections, the largest of which are more than 2mm thick.

Clay aggregates: Like in the Nordmela Formation, the Fruholmen Formation contains aggregates of clay exhibiting dust rims inside the grains and showing bright first order interference colours.

Diagenetic minerals

Quartz cement: Syntaxial quartz cement in the Fruholmen Formation is present and intensifies closer to the stylolites which are also observed in the formation. Larger grains are observed closer to the stylolites (see figure **28**). Subhedral grains are observed where the quartz grains face empty pores.

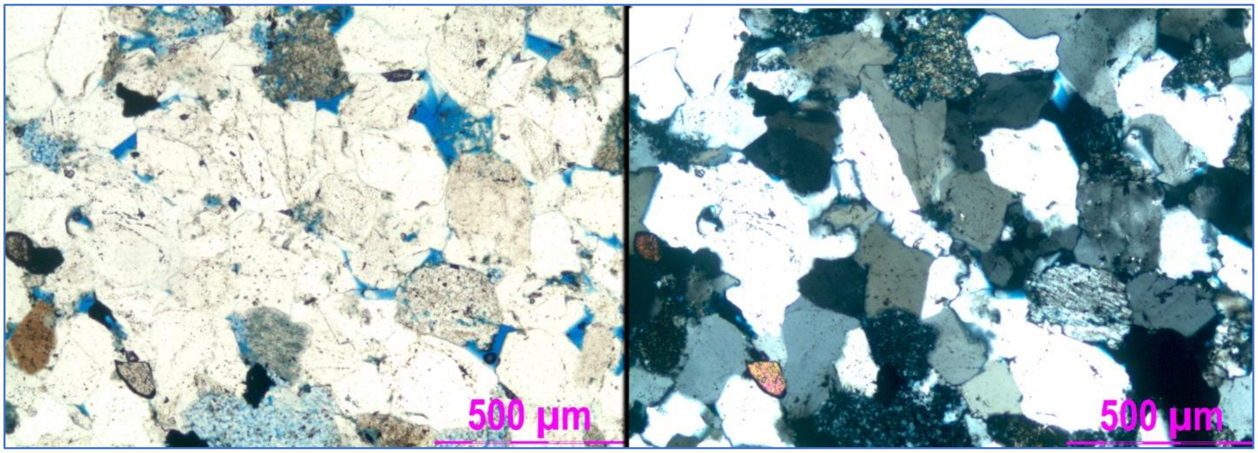

Figure 28: Thin section photograph of quartz cemented quartz grains. The grains are larger closer to the stylolites. Fruholmen Formation, depth = 1468.90m.

Kaolinite: Replacement of K-feldspar by kaolinite is observed in the Fruholmen Formation, with a larger volume of kaolinite compared to the Nordmela Formation.

Illite: Illite is observed as growing in plagioclase grains and as grain coatings (see Figure **29**).

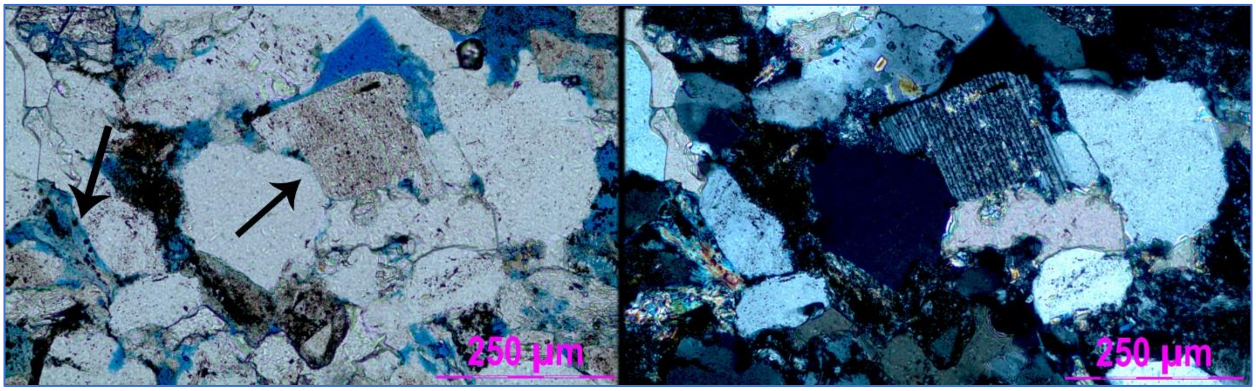

Figure 29: Thin section photos of illitization of plagioclase and illite grain coatings. Fruholmen Formation, depth = 1538.32m.

Carbonate cement: Siderite cement occurs in the Fruholmen Formation as both individual nodules and as grain coatings, notably growing on pyrite (see Figure **30).** The siderite cement overgrows calcite cement and clay aggregates. A single calci-sphere is observed in thin section. Calcite cement has grown on quartz cemented surfaces.

Pyrite: Pyrite is observed both as sand-sized grains and as silt-sized grains, with the smaller grains concentrated along stylolites.

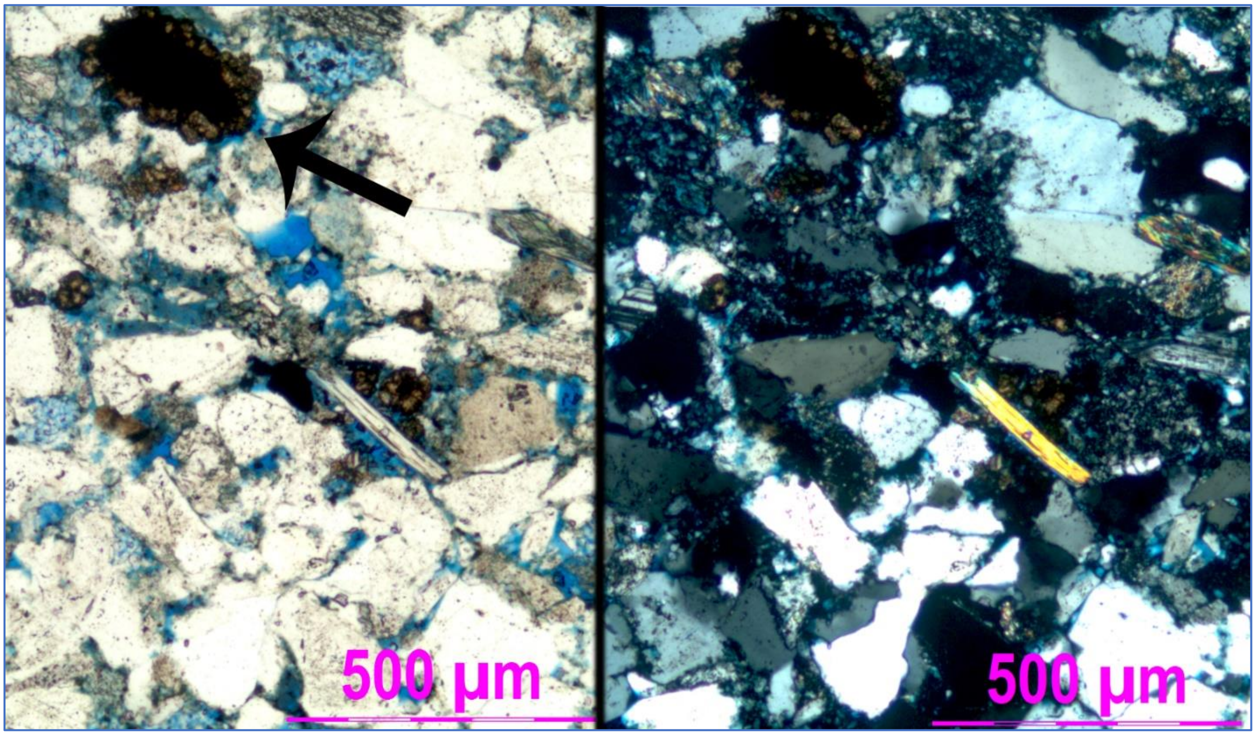

Figure 30: Thin section photograph showing pyrite grain with siderite coatings. Fruholmen Formation, depth = 1468.90m.

Snadd Formation

The Snadd Formation is included for comparison to the Nordmela and Fruholmen formations. A transition zone is observed in the thin section taken from depth 2840.50m, where the grain size suddenly decreases along a seemingly arbitrary horizon (see figures **31** and **32**).

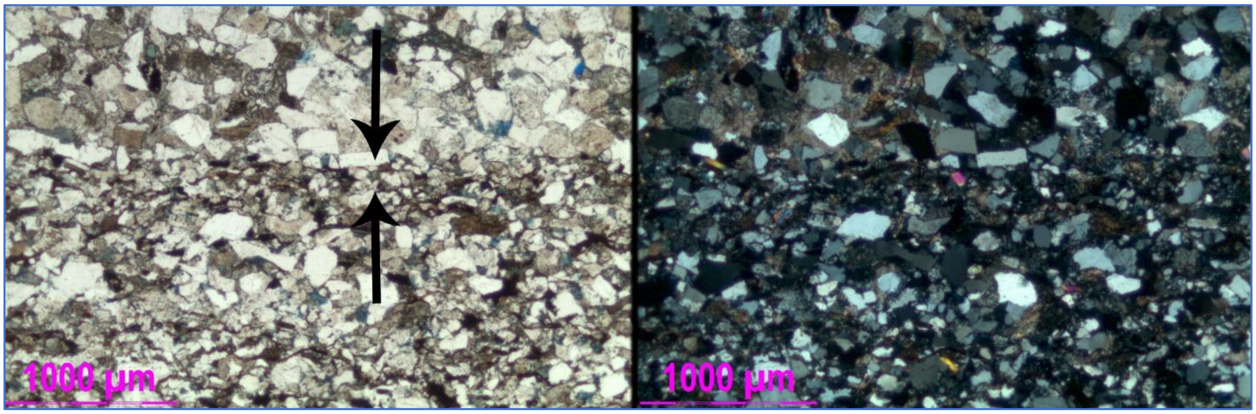

Figure 31: Thin section photograph showing the grain size transition zone, with larger grains above the horizon outlined in the picture. Snadd Formation, depth = 2840.50m.

Detrital grains

The Snadd Formation does not deviate much from the mineralogical makeup seen in the Nordmela and Fruholmen formations except for large amounts of carbonate matrix.

Quartz: Quartz grains are monocrystalline and show little signs of quartz cementation.

Plagioclase: The plagioclase grains are in different stages of dissolution, although no illite in plagioclase can be observed in the Snadd Formation.

Muscovite: Muscovite grains are present, but the small size of the grains means they are not large enough to show signs of mechanical deformation in optical microscopy.

K-feldspar: K-feldspar grains in various stages of dissolution are observed, none show twinning.

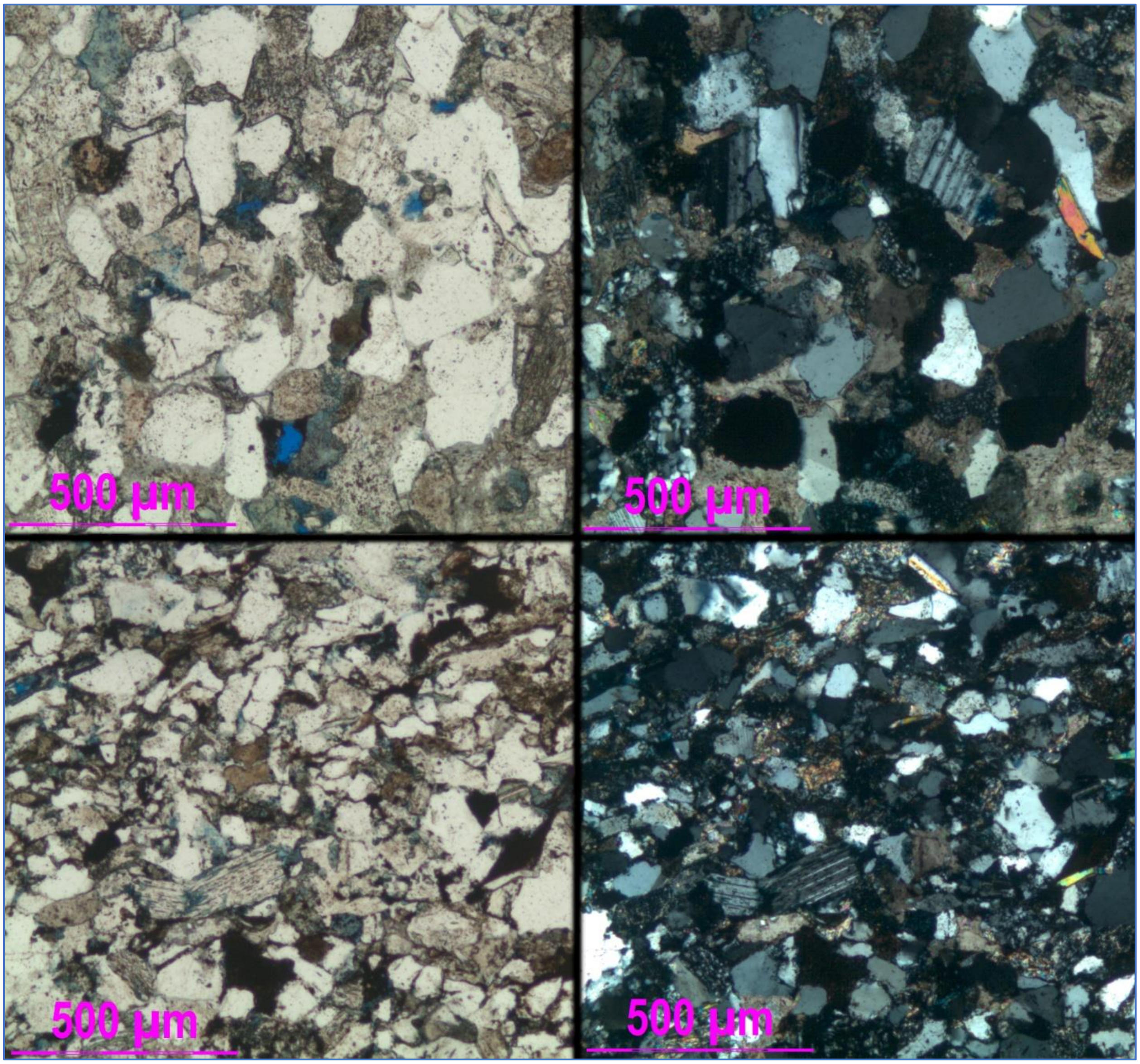

Figure 32: Thin section photograph showing grain size difference in Snadd. Upper photographs have Medium to Fine grains, while lower photographs have Fine to Very fine grains. Snadd Formation, depth = 2840.50m.

Matrix

Clay laminations: Laminations of clay minerals are present in the Snadd Formation (see figure **33**), although they are not laterally extensive like in the Fruholmen Formation.

Carbonate matrix: The Snadd Formation has near-zero intergranular porosity due to pore-filling carbonate matrix. The matrix shows little to no crystal structure.

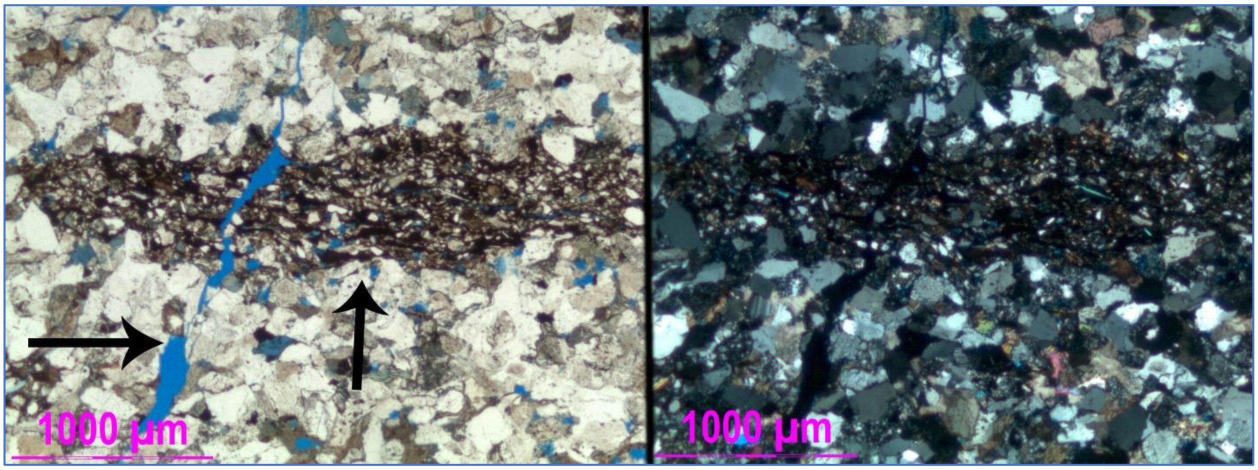

Figure 33: Thin section photograph showing clay laminations and fracture porosity. Snadd Formation, depth = 2846.70m

Diagenetic minerals

Carbonate cement: Calcite cement is present in the Snadd Formation, yet in lesser quantities than in the Nordmela and Fruholmen Formations.

Quartz cement: Little to no quartz cement is visible in the Snadd Formation, with mostly anhedral grains showing dust spots throughout the whole grain. The quartz grains do show signs of dissolution and intergrowth, and it is likely that the dissolved quartz cemented elsewhere is not visible without cathodoluminescence.

Kaolinite: Kaolinite grows in pores where dissolved K-feldspar once resided, although the amount of kaolinite is lower than in both the Nordmela and Fruholmen Formations.

Results of EDS and BSE analysis

The EDS and BSE analysis has helped to determine the mineralogy of the different grains observed in thin section samples. It has been especially helpful in telling apart quartz and non-twinned feldspars, as well as telling apart siderite and pyrite cement. The EDS analysis results are presented formation by formation, with accompanying backscatter photographs, focusing on diagenetic minerals.

Nordmela Formation

The Nordmela Formation has been shown to contain little to no pyrite. The main carbonate present is siderite which appears as both separate grains and as cement in the formation (Figure **34**). The siderite is commonly found as displasive growths in chlorite (Figures **35 and 36**). Calcite is found in various stages of dissolution, with some crystals being triangular crystals which might be the effect of “hopper” crystal cross section or dedolomitization (Figure **38**).

Kaolinite is common in the formation, and illite is commonly observed growing in quartz grains and albite grains (Figures **34 and 40**). Albite appears in two forms, with both elongated crystals and as grain replacing mass (Figure **34**).

Quartz occurs as often cemented grains, showing good crystal faces where the porosity has permitted unimpeded cement growth (Figures **36** and **40**). Florencite was identified by EDS (see Appendix **B**) and is observed cementing quartz in the most mature section, running through quartz like veins (Figure **39**). A single feldspar grain containing albite and oligoclase lamellae was observed (Figure **37**).

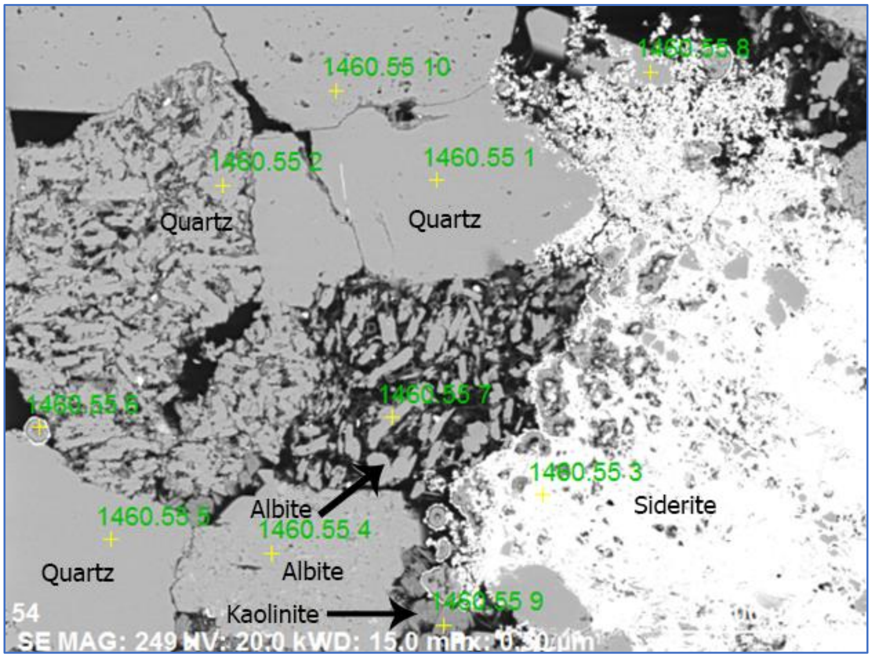

Figure 34: Backscatter image showing quartz grains, albite grains, kaolinite booklets and siderite cement. Nordmela formation, depth = 1460.55m.

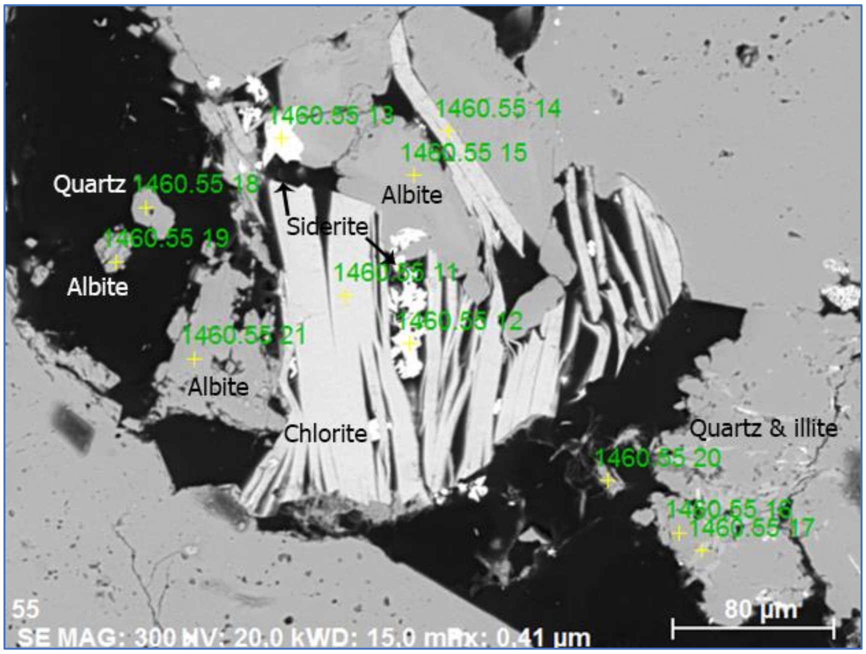

Figure 35: Backscatter image showing chlorite grains which appear to overgrow albite grains. Small illite grains are also visible growing in quartz in the lower right corner. Nordmela formation, depth = 1460.55m.

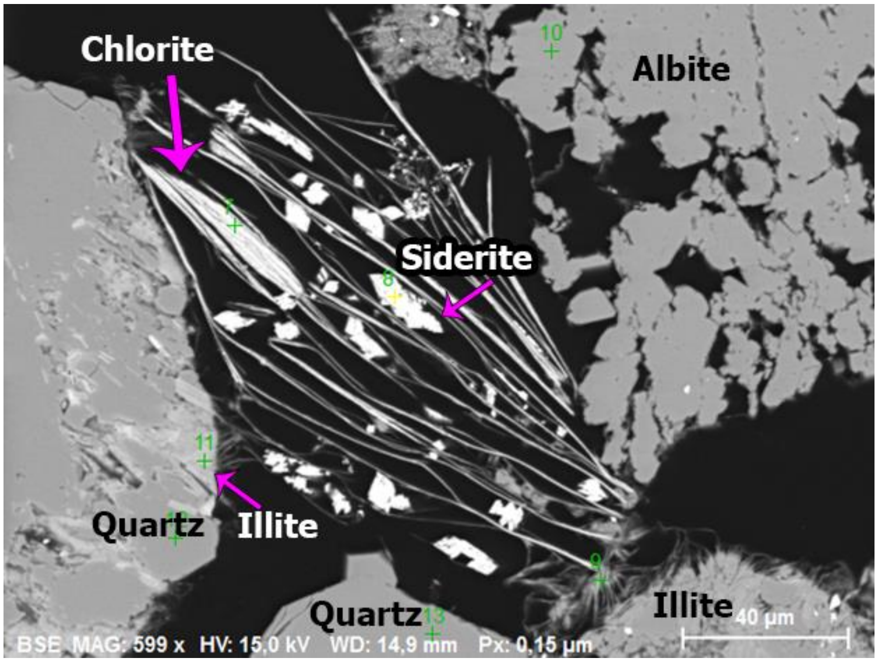

FIGURE 36: BACKSCATTER PHOTOGRAPH SHOWING DISPLASIVE GROWTH OF SIDERITE IN CHLORITE. NORDMELA FORMATION, DEPTH = 1460.80M.

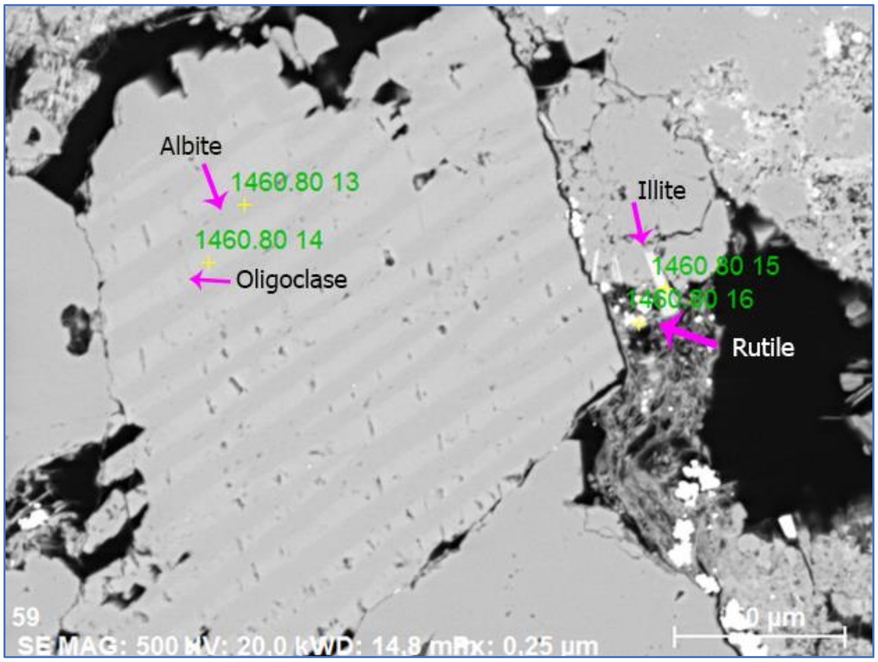

FIGURE 37: BACKSCATTER IMAGE SHOWING GRAIN CONSISTING OF ALBITE AND OLIGOCLASE LAMELLAE. NORDMELA FORMATION, DEPTH = 1460.80M.

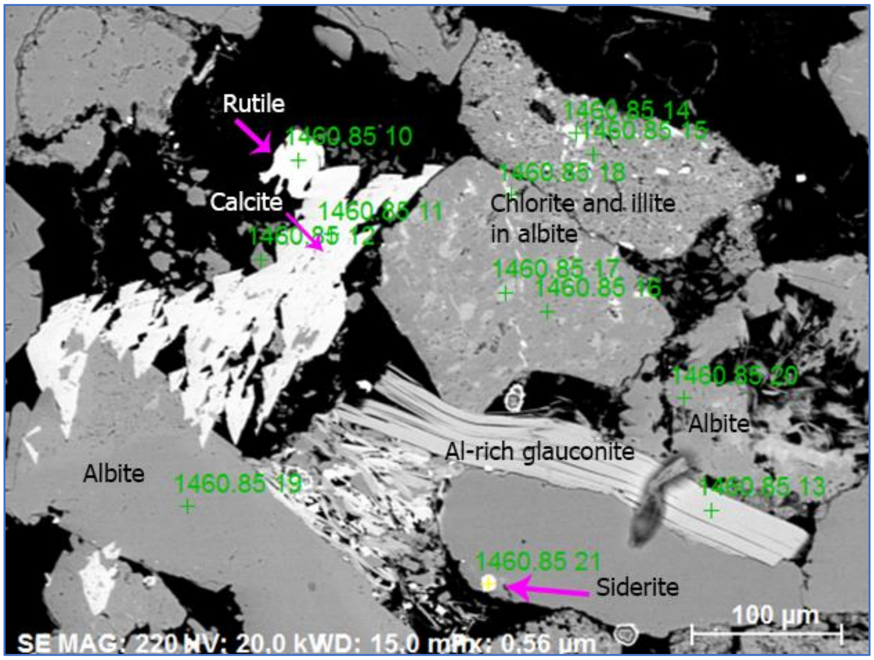

Figure 38: Backscatter image showing abundant albite intergrowing with calcite, siderite, illite and chlorite. The uncharacteristic shape of the calcite crystals might be the result of a cross section of hopper-habit calcite or dedolomitization. Dissolution of albite in the right side of the image. Nordmela formation, depth = 1460.85m.

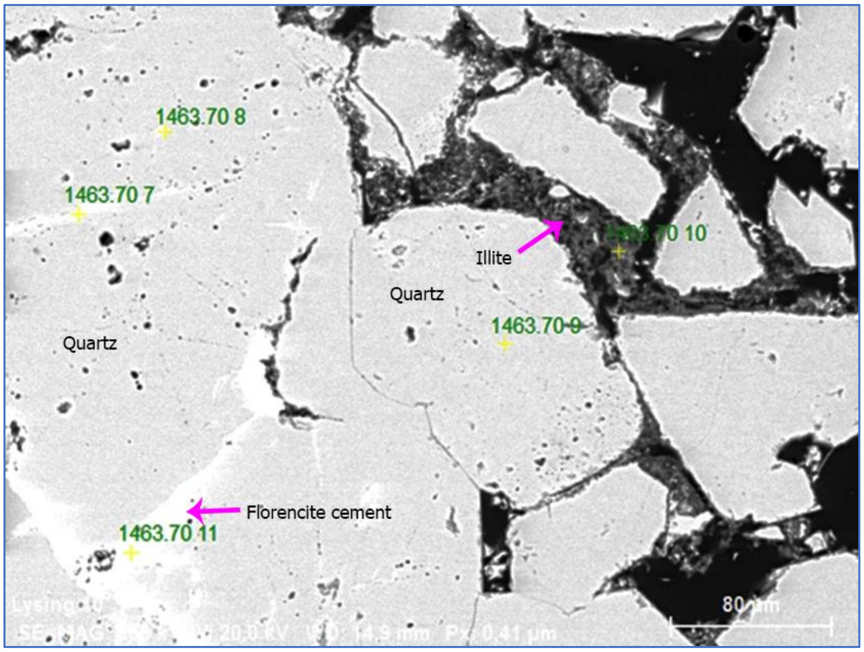

Figure 39: Backscatter image showing a Rare-Earth-Elements (REE) rich veins running through quartz. Vein mineral identified as lanthanum-florencite. Nordmela formation, depth = 1463.70m.

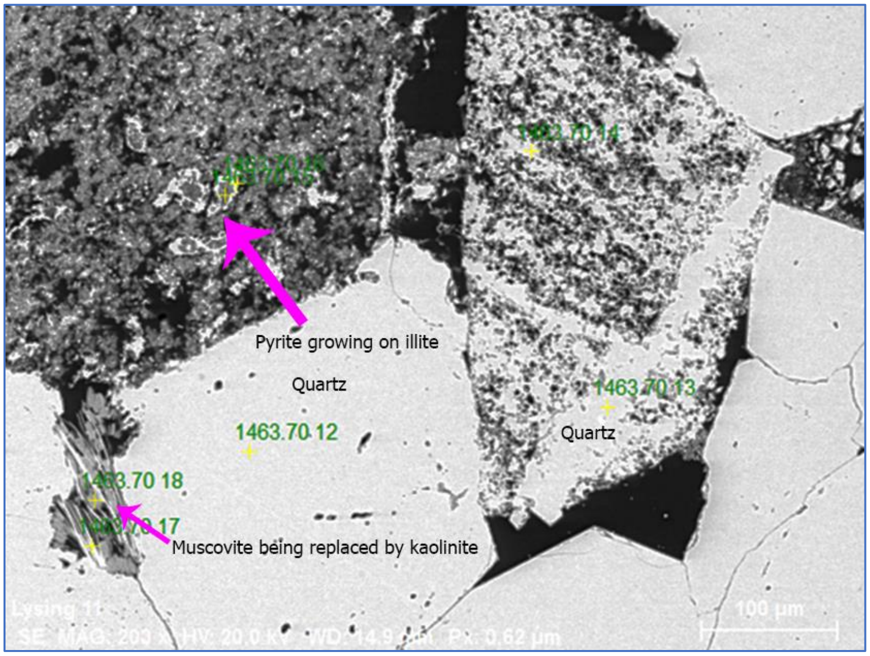

Figure 40: Backscatter image showing cemented quartz grains, pyrite growing on illite and muscovite being replaced by kaolinite. Nordmela formation, depth = 1463.70m.

Fruholmen Formation

The Fruholmen formation has a higher pyrite/siderite ratio than the Nordmela Formation, with the siderite surrounding the pyrite (see Figure **42**). The pyrite is also observed as cement around quartz and albite grains, where the albite is highly fractured (Figure **41**).

Clay laminations and stylolites are observed in the Fruholmen formation. The clay laminations are a mix of smaller illite, chlorite, albite and quartz grains along with larger siderite grains (Figure **44**). The stylolites are made up of micas and less soluble minerals along with organic matter (Figure **46**). The porosity is very low around the stylolites, with apparent dissolution and cementation of quartz grains.

Illite is observed replacing expanded muscovite (Figure **50**), and siderite is observed in strands which look very similar to the displasive muscovite strands (Figure **49**). Siderite is also observed growing concentrically around partially dissolved siliciclastic nuclei (Figure **48**). Both calcite and Mg-rich calcite are observed in the formation (Figures **47** and **49**), with some siderite also showing high Mg-content.

Quartz grains are slightly less common than in the Nordmela formation and with a lower degree of developed crystal faces. There is slightly more chert than in the Nordmela Formation. Authigenic albite is more common in the Fruholmen formation, with grains in varying states of dissolution. Both monazite and florencite are observed in the Fruholmen formation as individual grains which are not cemented on quartz (Figures **43** and **47**). Ti-enriched illites are observed as well as Ti-containing rutile (Figure **45**).

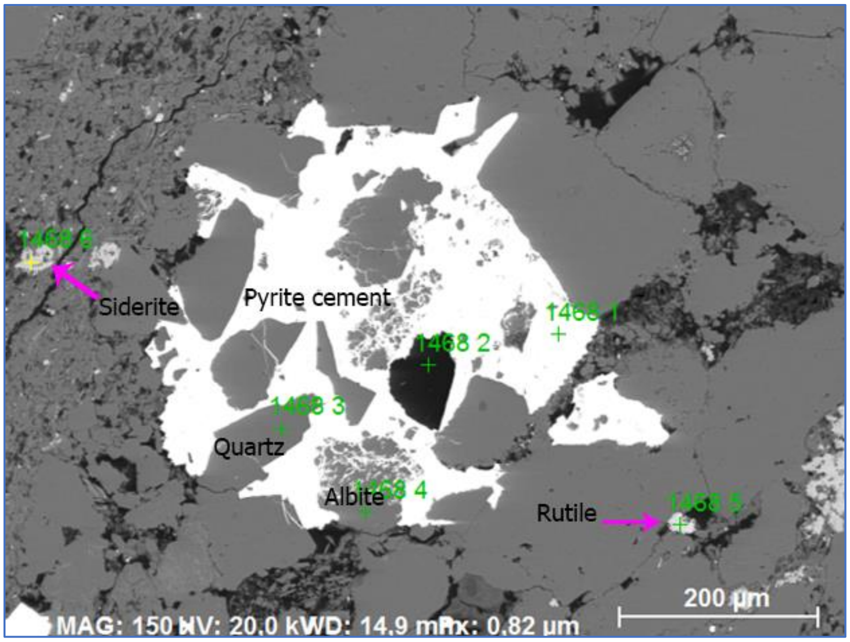

Figure 41: Backscatter image showing pyrite cement around quartz and partially dissolved albite. Accessory rutile and siderite. Fruholmen formation, depth = 1468.90m.

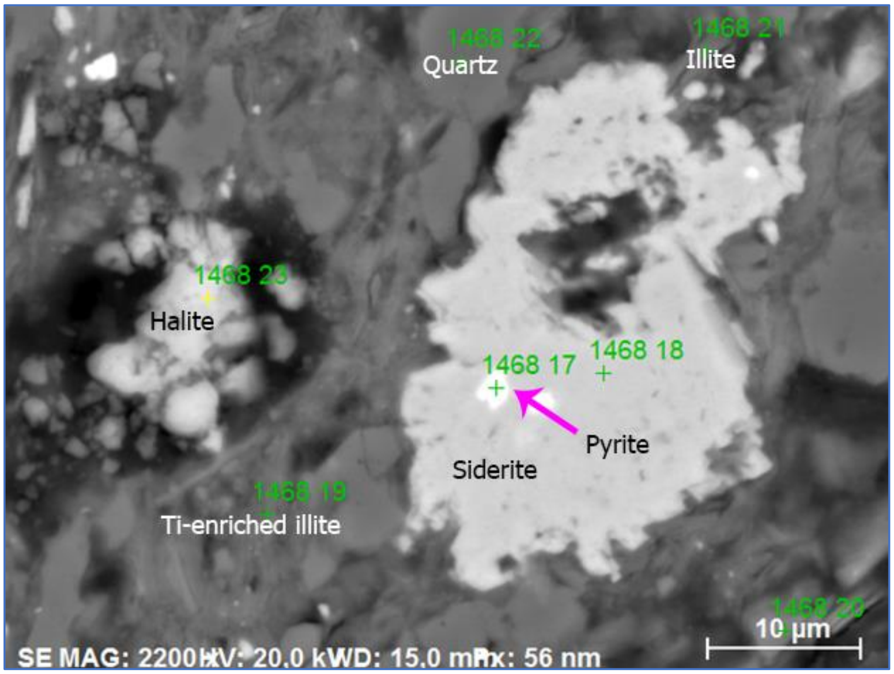

Figure 42: Backscatter image showing siderite surrounding pyrite grains. Contains both regular illite and Ti-enriched illite. Fruholmen formation, depth = 1468.90m.

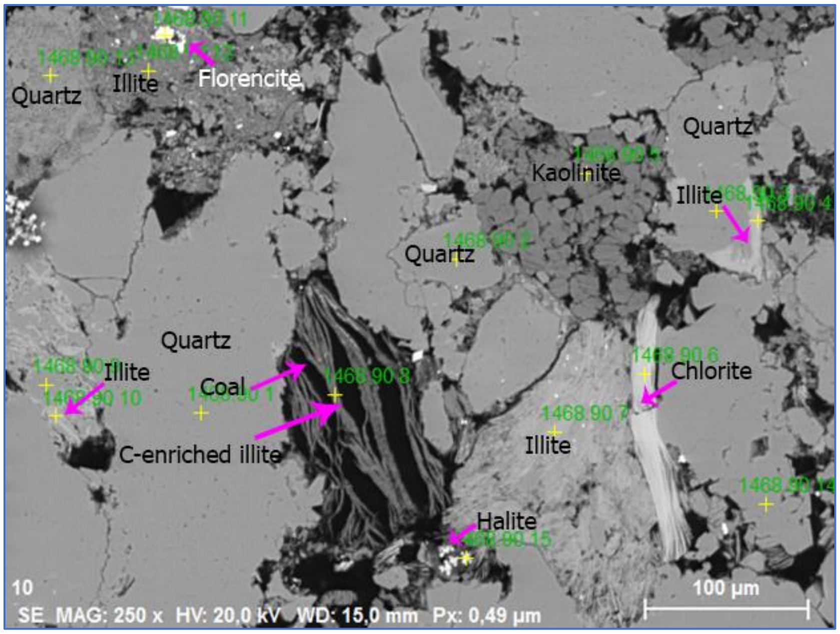

FIGURE 43: BACKSCATTER IMAGE SHOWING ILLITE GROWING BOTH IN AND COATING QUARTZ GRAINS. BOTH REGULAR AND C-ENRICHED ILLITE, WITH COAL-ILLITE LAMELLAE VISIBLE. LONG FIBROUS ILLITE STRANDS ALMOST PARALLEL TO CHLORITE. SMALL GRAINS OF FLORENCITE. FRUHOLMEN FORMATION, DEPTH = 1468.90M.

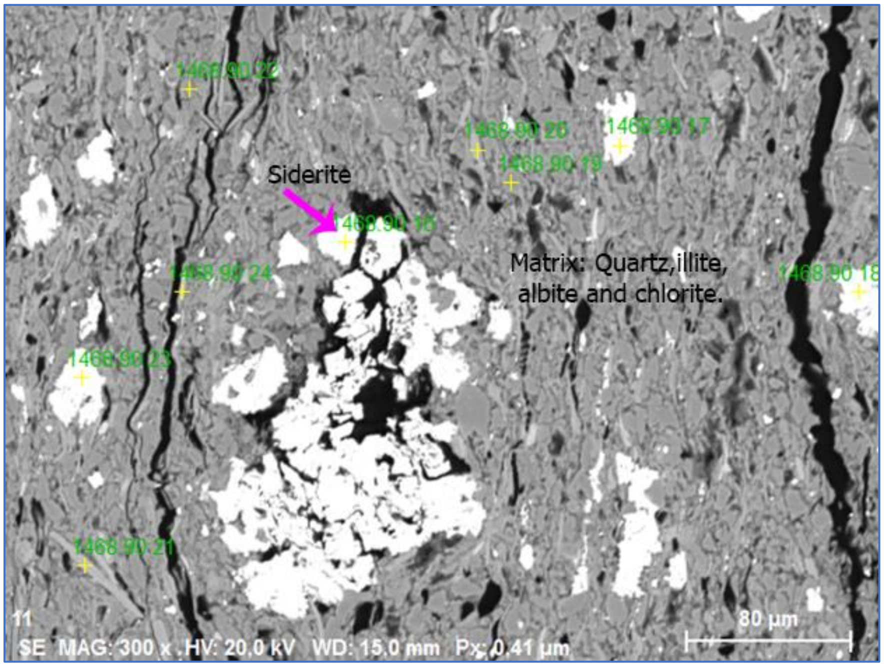

FIGURE 44: BACKSCATTER IMAGE SHOWING THE CONTENT OF A CLAY LAMINATION RUNNING THROUGH THE OTHERWISE SAND-RICH THIN SECTION. HIGH SIDERITE CONTENT, ALONG WITH A MATRIX CONSISTING OF QUARTZ, ILLITE, ALBITE AND CHLORITE. FRUHOLMEN FORMATION, DEPTH = 1468.90M.

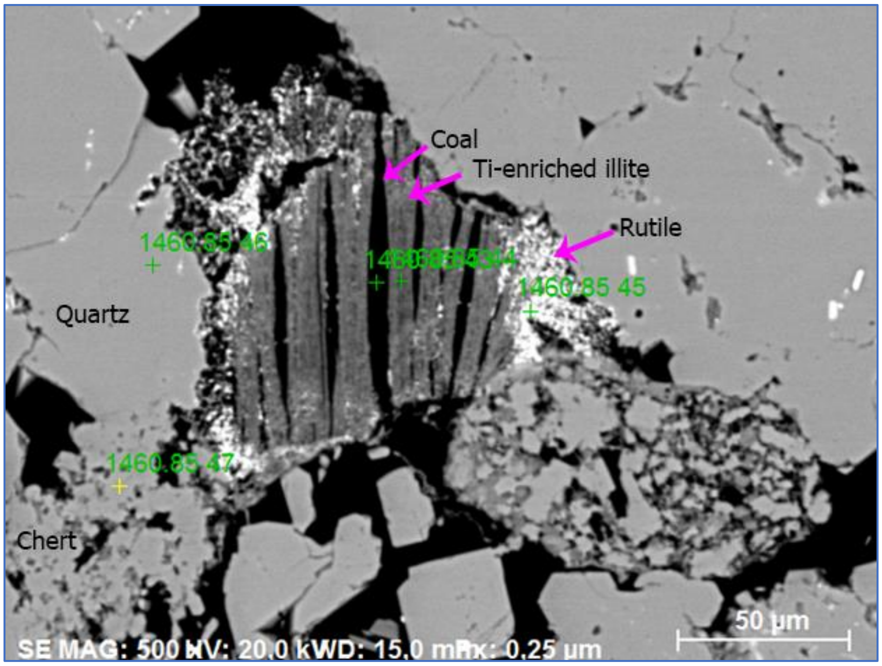

Figure 45: Backscatter image showing alternating coal and Ti-enriched illite lamellae along with rutile grains. Fruholmen formation, depth = 1487.95m.

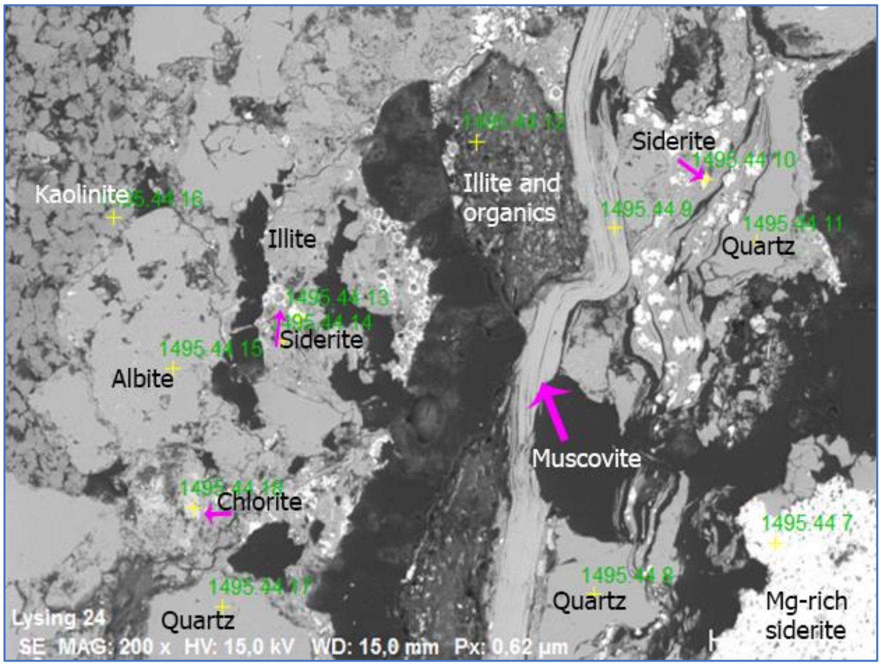

Figure 46: Backscatter image showing a stylolite with high concentration of heavy minerals and organic material. Fruholmen formation, depth = 1495.44m.

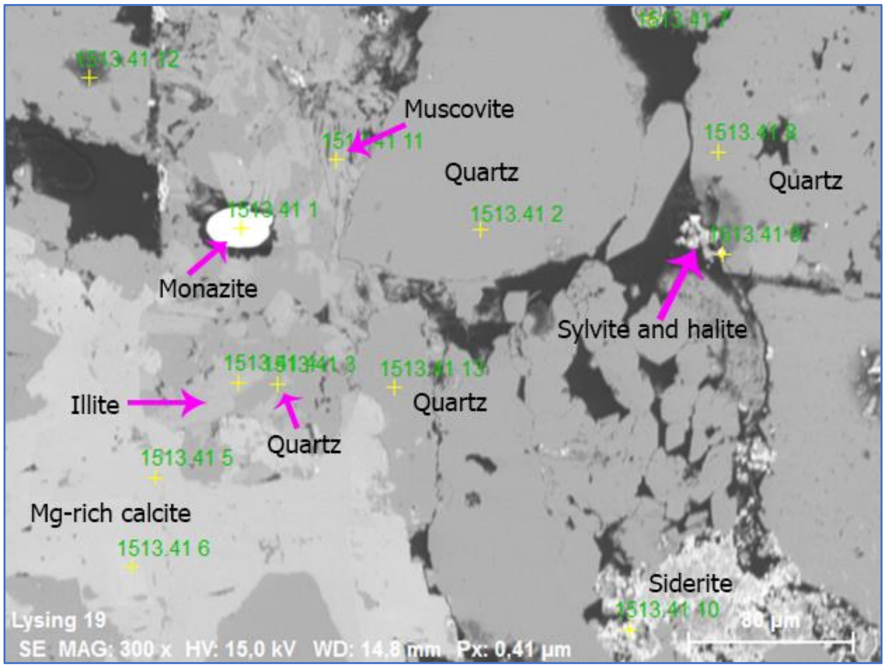

Figure 47: Backscatter image showing magnesium-rich calcite surrounding illite and quartz intergrowths. Fruholmen formation, depth = 1513.41m.

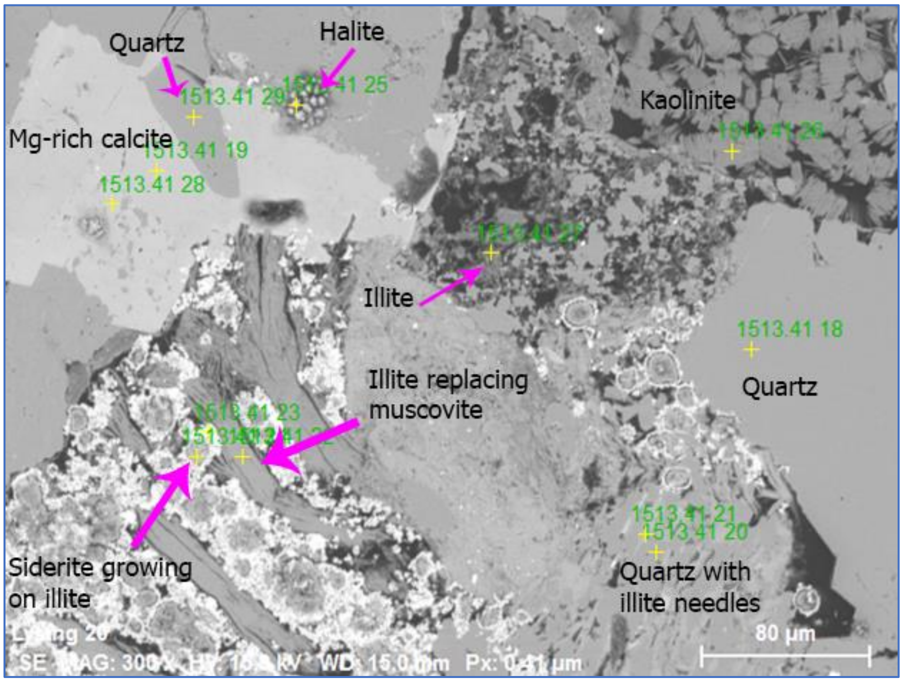

Figure 48: Backscatter image showing illite replacing muscovite and retaining the mica-morphology. Siderite crystals are shown to accumulate around illite with distinct rounding of illite grains. Fruholmen formation, depth = 1513.41m.

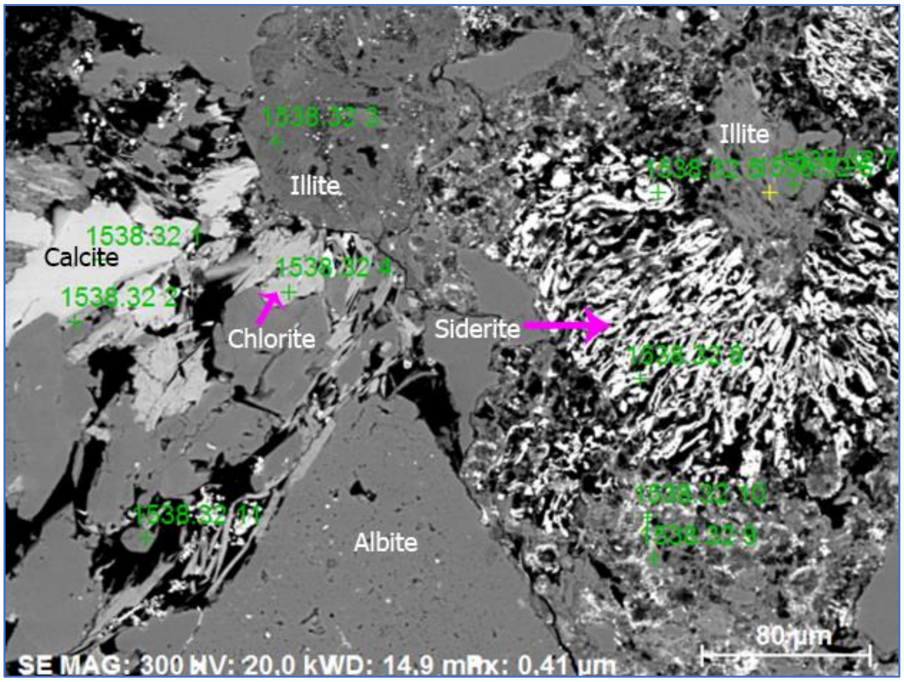

Figure 49: Backscatter image of siderite strands with mica-like morphology, Possibly replacing a biotite. Also shown is calcite, chlorite and albite. Lower right corner shows partly dissolved albite with illite and siderite. Fruholmen formation, depth = 1538.32m.

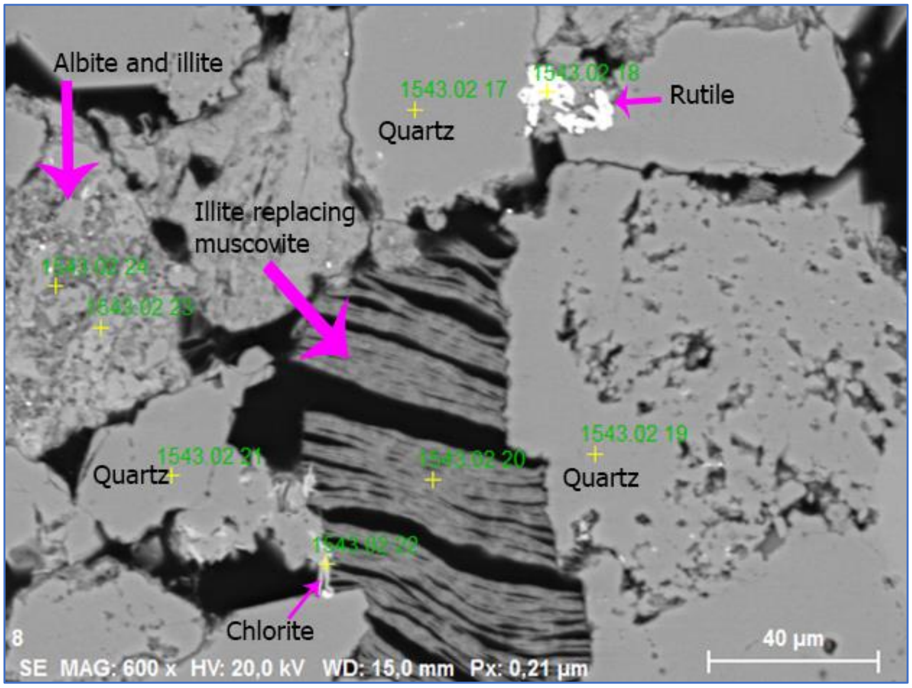

Figure 50: Backscatter image showing illite replacing muscovite. The quartz in the right side of the picture can be seen being limited by the illite-muscovite. Depth = 1543.02m.

Snadd Formation

The Snadd formation shows a high degree of cementation, with Mg-rich calcite cement and ankerite filling the pores. The quartz grains in the formation are seemingly less quartz cemented than in the other two formations, with very few grains showing developed crystal faces. The few grains that are quartz cemented are facing carbonate cement (see Figure **53** for an example), implying the carbonate was precipitated after quartz cementation had taken place.

Siderite crystals surrounded by albite show euhedral crystal habit, implying albite was precipitated after siderite growth (Figure **53**). Chlorite is observed parallel with an unknown mica-like mineral, possibly glauconite (Figures **51** and **52**). Muscovite is also observed in the Snadd Formation (Figure **53**). Chlorite needles are also observed in albite (Figure **52**).

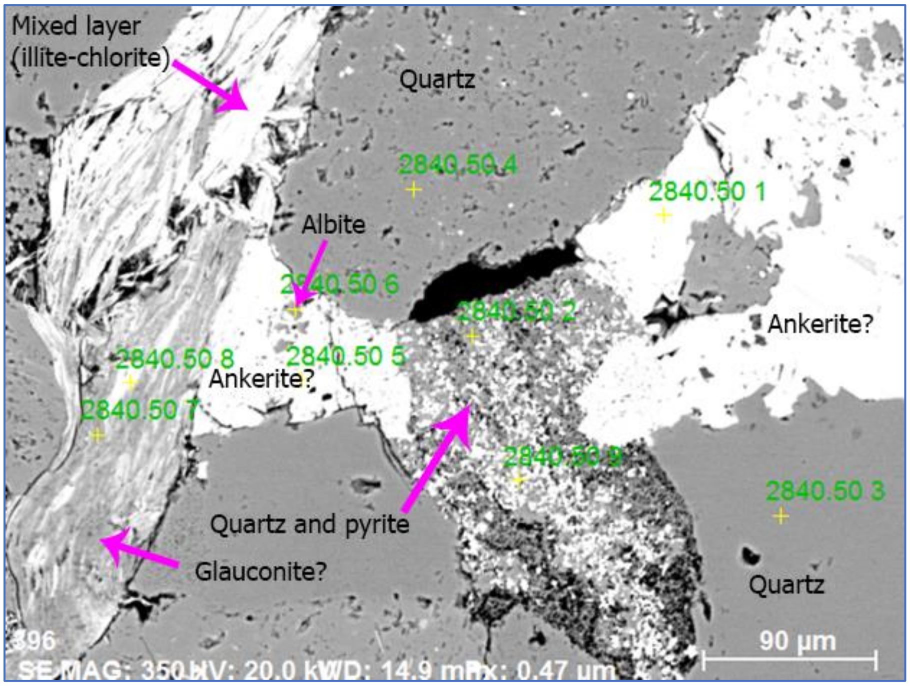

Figure 51: Backscatter image showing ankerite cement, mixed layer illite-chlorite parallel with what might be glauconite. Pyrite and quartz/chert. Snadd Formation, depth = 2840.50m.

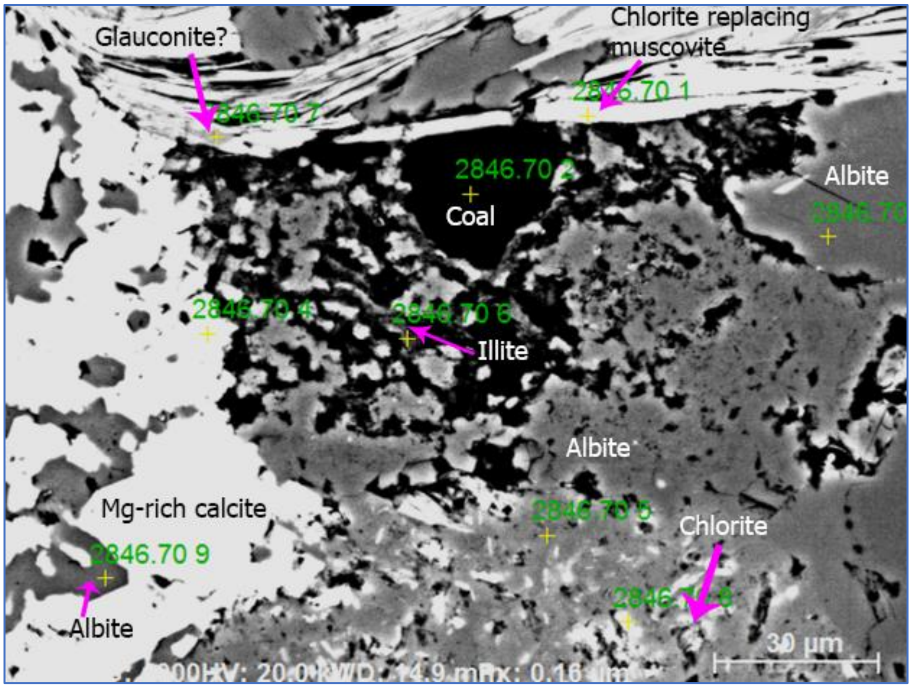

Figure 52: Backscatter image showing coal fragments and muscovite being replaced by lamellae of chlorite and possibly glauconite. Snadd formation, depth = 2846.70m.

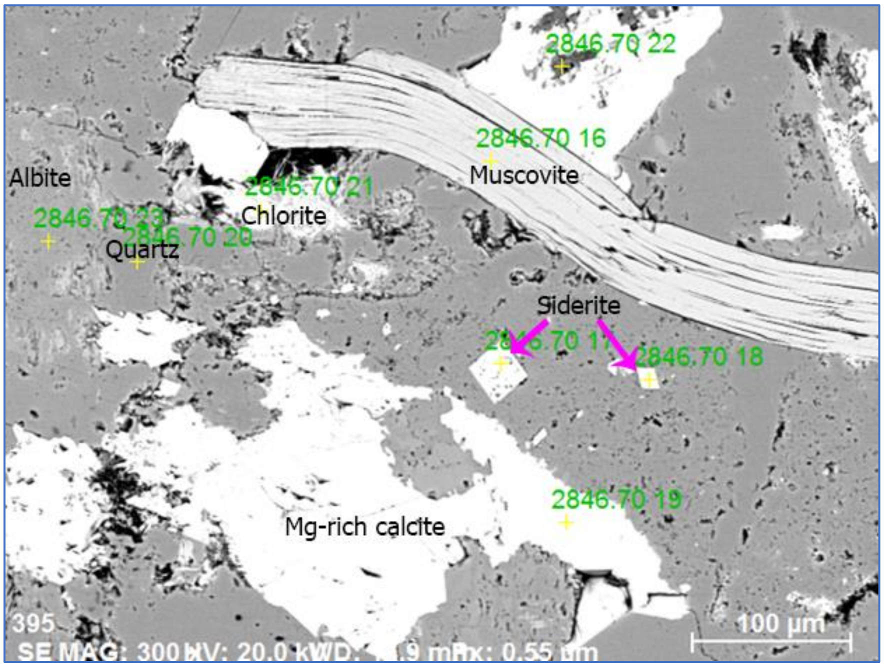

Figure 53: Backscatter image showing euhedral siderite crystals. Euhedral quartz face in lower right corner bordering Mg-rich calcite cement. Snadd formation, depth = 2846.70

Discussion

The author will begin the discussion of findings by presenting the diagenetic processes that were observed. The author then offers a comparison of the processes in the different formations and the reservoir potential of each formation.

Diagenetic processes observed in the thin sections

The following processes and minerals were observed during optical microscopy:

1. Mechanical compaction is evident when observing deformed muscovite grains, as these grains appear to be have been bent between other detrital grains.
2. Dissolution of K-feldspar and muscovite, and replacement of K-feldspar with kaolinite implies temperatures of at least 30-60 °C, a low K^+/H^+ ratio and sufficient water flux (Knut Bjørlykke & Jahren, 2010).
3. Quartz cementation implies temperatures above 80-100 °C and sufficient surface area for cement growth (Knut Bjørlykke & Jahren, 2010). Cement concentration closer to stylolites is also observed in the Fruholmen formation, which matches observations made in the Stø formation by Walderhaug and Bjørkum (Walderhaug & Bjørkum, 2003). See Table **3** for cement quantities.
4. Illitization of kaolinite and K-feldspar occurs at approximately 130 °C, and at 70-80 °C for smectite illitization (Knut Bjørlykke & Jahren, 2010). The illitization observed in the formations is not complete, and kaolinite and K-feldspar are observed in the same thin sections. This implies that the temperatures necessary for illitization of kaolinite and K-feldspar happened during a limited time interval or was interrupted by lowering temperatures.
5. Carbonate cementation of calcite is apparent in all the formations that were studied. Calcite is observed growing on quartz-cemented quartz grains, implying the calcite cementation at least partially happened after the quartz cementation. A single calci-sphere is observed in the Fruholmen Formation, which suggests the cement might be derived from local dissolved carbonate grains. Siderite cementation is apparent in the Fruholmen Formation, especially in volumes where calcite and clay aggregates share borders. This

implies that the iron content in the clay aggregates is high enough to supply the iron necessary for siderite formation.

6. Pyrite is observed in the formations as both large and small crystals, which means a sulphate reduction zone was present during burial. Siderite has been observed growing on some of the larger pyrite grains, implying the sulphate content in the pore water was not high enough to spend all the detrital iron on forming pyrite. The grains of the pyrite with siderite cement surrounding it present the transition from the sulphate reduction zone to either the sub-oxic zone or the methanogenesis zone (Irwin et al., 1977)

In addition to the processes observed in optical microscopy, several diagenetic reactions and minerals have been observed in the use of SEM.

The alteration of kaolinite into dickite may gradually occur at depths between 2500m and 5000m (Beaufort et al., 1998), although it is tricky to tell the two minerals apart without studying the morphology. The kaolin observed in this paper show the regular booklet shape associated with kaolinite (see Figure **54**), but it cannot be ruled out that the kaolin has a partial content of dickite. Provided that the uplift theory is correct, the formation may have been buried at 2500m depth or more and might therefore have experienced kaolinite-dickite alteration.

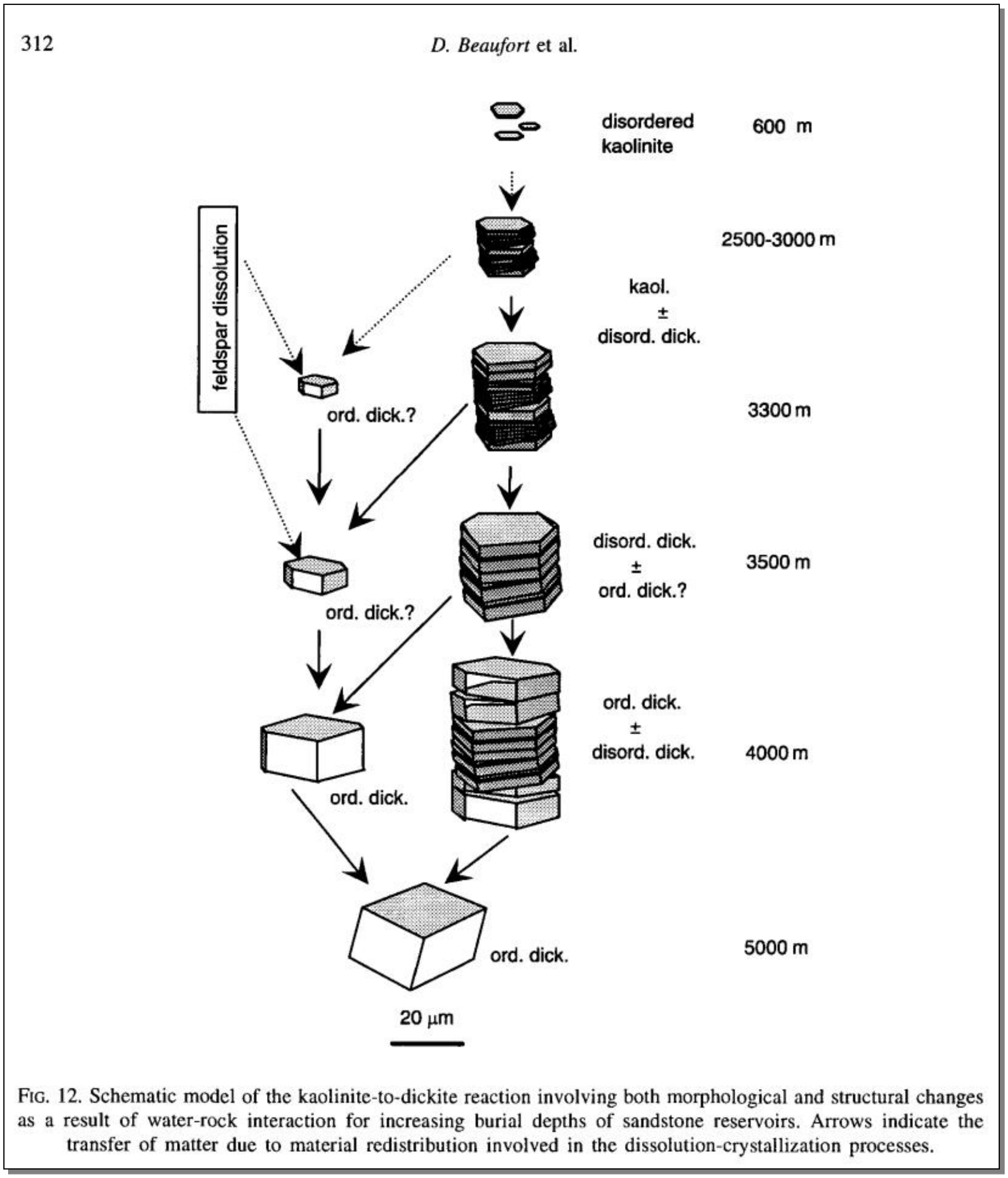

312 *D. Beaufort* et al.

FIG. 12. Schematic model of the kaolinite-to-dickite reaction involving both morphological and structural changes as a result of water-rock interaction for increasing burial depths of sandstone reservoirs. Arrows indicate the transfer of matter due to material redistribution involved in the dissolution-crystallization processes.

FIGURE 54: A GRAPHIC REPRESENTATION OF KAOLINITE-DICKITE ALTERATION (BEAUFORT ET AL., 1998)

The breakdown of kaolinite can happen with different reaction routes, and two main breakdown reactions are thought to have occurred in the sediments described in this paper. The first reaction presented in Equation **1** consumes both kaolinite and K-feldspar and produces both illite and silica.

$$\mathbf{Al_2SiO_5(OH)_4 + KAlSi_3O_8 \rightleftharpoons KAl_3Si_3O_{10}(OH)_2 + 2SiO_2 + H_2O \quad (1)}$$

Kaolinite + K-feldspar ⇌ Illite + Quartz + Water

(K Bjørlykke, 1998)

The anhedral grains of quartz and illite grains observed in figures **35**, **36** and **43** suggest that the common illite-forming reaction has taken place and removed kaolinite and K-feldspar. The illite is also often present as fairly straight needles inside the quartz/silica, unlike the meandering illite threads observed elsewhere (see Figure **36**).

The second important kaolinite breakdown reaction is presented in Equation **2** and consumes kaolinite, K-feldspar and sodium from the porewater which then produces illite and albite along with acidic water.

$$\mathbf{3Al_2SiO_5(OH)_4 + 2KAlSi_3O_8 + 2Na^+ \rightleftharpoons 2KAl_3Si_3O_{10}(OH)_2 + 2NaAlSi_3O_8 + 2H^+ + 3H_2O \ (2)}$$

3Kaolinite + 2K-feldspar + 2Sodium ⇌ 2Illite + 2Albite + 2Hydrogen + 2Water

(K Bjørlykke, 1998)

The albite with illite strands inside the grains seen in figures **38**, **50** and **53** suggesting that the albite-forming reaction has consumed and replaced the kaolinite, with the illite strands showing little signs of deformation like much of the other illite in the thin sections. The albite forming reaction suggests temperatures exceeding 120-130°C and is a good indicator of the minimum temperature the formations have experienced.

Albite is shown as both anhedral grains and as elongated grains with visible crystal faces (figures **34**, **36**, **37** and **52**). The crystal faces are regularly observed in thin sections where the albite is surrounded by porosity, suggesting that there were no other grains hindering the diagenetic growth of said crystal faces. However, the clear majority of the observed albite grains have no developed crystal faces and show signs of alteration. Little to no albite grains show evidence of rounding as a result of transport or abrasion, and instead take on a more matrix-like form surrounding other minerals. The CL imaging shows no difference in luminescence between the euhedral albites and matrix-like albites, suggesting they are all diagenetic in origin with the exception of individual grains containing albite-oligoclase lamellae (see Figure **37**). These oligoclase lamellae show a much stronger luminescence under CL than the albite (see Figure **55**), which suggests they are detrital in origin (Parsons et al., 2005).

These grains of albite-oligoclase lamellae remained a mystery until investigated by CL. Albite-oligoclase lamellae are common in peristerites, however these lamellae are usually not visible on the micrometer-scale used in CL. A comprehensive SEM elemental analysis of the lamellae (N=68, n=36 albite, n=32 oligoclase, see Appendix **C**) put the grain in the peristerite miscibility gap with a molar bulk composition of An_8Alb_{92} (see Figure **56**). This composition would imply temperatures more than 400 °C, which is outside the diagenetic temperature range. By studying the grain in Figure **37** further one can see the oligoclase lamellae are less chemically stable and shows signs of fracturing while the albite appears less fractured but much more dissolved at the edges of the grain – the oligoclase lamellae sticks out of the grain like the teeth of a comb. As Ca-rich plagioclase is less stable than Na-rich plagioclase at the depths investigated, it appears that the albite was precipitated at a later point than the oligoclase. The difference in luminescence strengthens this hypothesis, and it was concluded that this is a detrital perthite which had its K-feldspar content replaced by albite during burial. However, it is strange that the oligoclase survived burial when most K-feldspar in the formations has been dissolved.

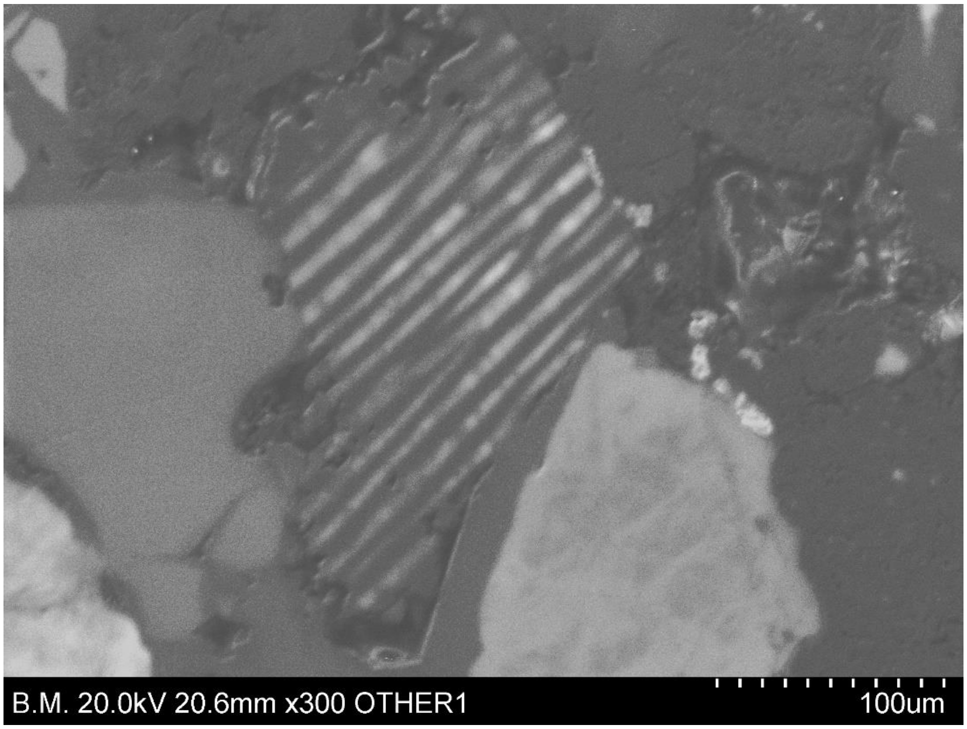

Figure 55: Albite-oligoclase lamellae seen under CL. Same lamellar grain as presented in the Nordmela results section for backscatter photos.

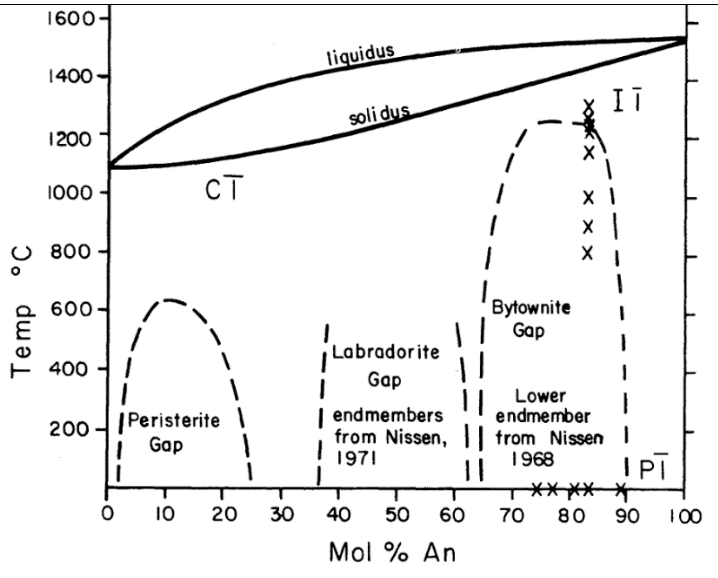

Figure 3. Simplified phase diagram for plagioclase showing only the miscibility gaps, as envisaged by Nord et al. (1974). Reproduced by kind permission of G.L.Nord, Jr.

Figure 56: Plagioclase phase diagram as proposed by Nord et al. Peristerite miscibility gap shown in the lower left corner. (Parsons, 2012)

There is a moderately high content of authigenic illite in the studied formations. Pore-filling illite is known to be a permeability destroying clay mineral with detrimental effects on reservoir properties (Pallatt et al., 1984). The SEM-analysis has shown that illite manifests as pore-bridging, grain-coating and inside albite/quartz grains (interpreted as kaolinite replacing). The pore-bridging morphology of illite is the one with the highest impact on permeability, reducing permeability more compared to other forms of illite. It should be noted that the drying method of the cores influences the perceived quantity of pore-bridging illite. The method of critical point drying is preferable if the goal is to study illite morphology as it appears in reservoir conditions. Methods such as air drying may cause the pore-bridging illite to flatten against grain surfaces, and therefore masquerade as grain-coating when it is not. The air-dried cores may therefore not yield the same permeability results during laboratory testing as is observed in during well testing (Kantorowicz, 1990). Unfortunately, the geochemical reports attached to well 7321/8-1 do not specify which method was used to dry the cores, and so there may be sources of errors with regards to the amount of pore-bridging illite.

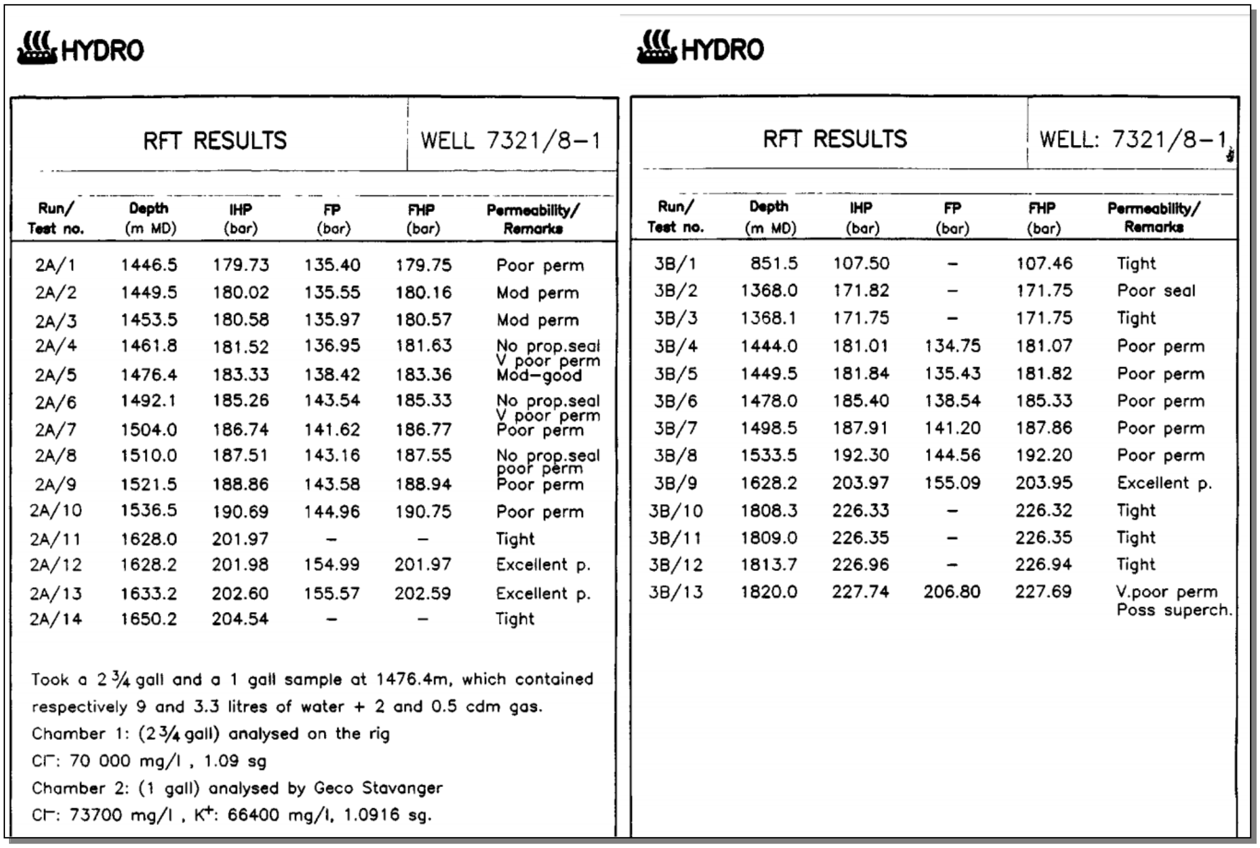

HYDRO

RFT RESULTS | WELL 7321/8-1

Run/ Test no.	Depth (m MD)	IHP (bar)	FP (bar)	FHP (bar)	Permeability/ Remarks
2A/1	1446.5	179.73	135.40	179.75	Poor perm
2A/2	1449.5	180.02	135.55	180.16	Mod perm
2A/3	1453.5	180.58	135.97	180.57	Mod perm
2A/4	1461.8	181.52	136.95	181.63	No prop.seal V poor perm
2A/5	1476.4	183.33	138.42	183.36	Mod–good
2A/6	1492.1	185.26	143.54	185.33	No prop.seal V poor perm
2A/7	1504.0	186.74	141.62	186.77	Poor perm
2A/8	1510.0	187.51	143.16	187.55	No prop.seal poor perm
2A/9	1521.5	188.86	143.58	188.94	Poor perm
2A/10	1536.5	190.69	144.96	190.75	Poor perm
2A/11	1628.0	201.97	–	–	Tight
2A/12	1628.2	201.98	154.99	201.97	Excellent p.
2A/13	1633.2	202.60	155.57	202.59	Excellent p.
2A/14	1650.2	204.54	–	–	Tight

Took a 2 ¾ gall and a 1 gall sample at 1476.4m, which contained respectively 9 and 3.3 litres of water + 2 and 0.5 cdm gas.
Chamber 1: (2 ¾ gall) analysed on the rig
Cl^-: 70 000 mg/l , 1.09 sg
Chamber 2: (1 gall) analysed by Geco Stavanger
Cl^-: 73700 mg/l , K^+: 66400 mg/l, 1.0916 sg.

HYDRO

RFT RESULTS | WELL: 7321/8-1

Run/ Test no.	Depth (m MD)	IHP (bar)	FP (bar)	FHP (bar)	Permeability/ Remarks
3B/1	851.5	107.50	–	107.46	Tight
3B/2	1368.0	171.82	–	171.75	Poor seal
3B/3	1368.1	171.75	–	171.75	Tight
3B/4	1444.0	181.01	134.75	181.07	Poor perm
3B/5	1449.5	181.84	135.43	181.82	Poor perm
3B/6	1478.0	185.40	138.54	185.33	Poor perm
3B/7	1498.5	187.91	141.20	187.86	Poor perm
3B/8	1533.5	192.30	144.56	192.20	Poor perm
3B/9	1628.2	203.97	155.09	203.95	Excellent p.
3B/10	1808.3	226.33	–	226.32	Tight
3B/11	1809.0	226.35	–	226.35	Tight
3B/12	1813.7	226.96	–	226.94	Tight
3B/13	1820.0	227.74	206.80	227.69	V.poor perm Poss superch.

FIGURE 57: RELEVANT PERMEABILITY REMARKS IN HYDRO DOCUMENTS. EXTRACTED FROM DOCUMENT "1070_1" IN THE WELL DIRECTORY (OLJEDIREKTORATET, 2005)

With regards to non-quartz grain coatings, no chlorite coatings have been directly observed. However, there are illite coatings observed on quartz grains in backscatter images (figures **36**, **39** and **40**). Illite coatings are generally considered to be detrimental to reservoir properties, unless the grain coating illite is formed early and the growth stops – in which case it is porosity preserving (Storvoll et al., 2002). The illite does not appear to have acted as a porosity preserver in the formations studied, and the poor permeabilities shown in figure **57** suggests the illite has acted as a permeability killer as well.

Much of the calcite cement is observed to be concentrated around albite grains. Along with the oligoclase observed in figure **37** it can be reasonably assumed that albitization of Ca-containing plagioclase with the calcium being incorporated into calcites and becoming cement around the Ca-source grain has occurred. Organic matter is observed in the thin section samples, and dissolved organic matter has an inhibitory effect on Ca-calcite formation and instead favours

Mg-rich calcites (Kitano et al., 1969). This corresponds well with the Mg-rich calcites observed in the Snadd Formation.
Figure **48** shows siderite growing concentrically around nuclei which are dissolved. EDS analysis shows traces of alumina-silicates and siderite in the nuclei, but the dissolution is too high to pinpoint exactly what the nuclei were. However, the shape is rounded and there has been observed a calci-sphere in the formation which might suggest biogenic nuclei which could have been recrystallized into siderite or other carbonates.

In Figure **49**, siderite is shown as spaced out parallel strands which are quite similar to the expanded muscovite shown in Figure **50**. One explanation is the breakdown of biotite which provides the iron for the siderite while the siderite takes on a similar shape as the biotite grain. Displasive precipitation of siderite in chlorite is also observed in formation, which might suggest a similar origin for the siderite strands.

Stylolites have been observed in the Fruholmen Formation, and the quartz grains are larger and with less inter-crystalline porosity closer to the stylolites. Table 3 shows that there is extensive syntaxial quartz cementation in all formations with some variability, with the more mature sandstones in the formations having larger total volumes of porosity destroying quartz overgrowths due to the higher content of detrital quartz. The detrital makeup of the Nordmela and Fruholmen formations are not very different if one looks at figures **14** and **15**, although these figures are thought underrepresent the feldspar content as mentioned previously.

A peculiar duo of minerals is observed in thin sections – monazite and lanthanum-florencite. Probably formed early in diagenesis in sulphate reduction zone with the breakdown of organic materials, the florencite manifests as both individual crystals and as cement between quartz grains (figures **39** and **43**). The appearance of monazite suggests detrital monazite as a source for the authigenic florencite as the monazite observed (Figure **47**) has a highly rounded shape indicative of partial dissolution (Rasmussen, 1996). Figure **59** suggests another source of phosphorous and REE-elements, with the P-source being organic and REE-elements coming from clay-particles. It should be noted that the rounded monazite grain looks much like a zircon crystal (which have also been observed in the formations) and that P and Zr are difficult to tell apart on an EDS spectrum. However, the EDS spectrum for the grain (Figure **58**) matches perfectly with confirmed monazite spectra published by EDAX and is therefore named as monazite in this paper (EDAX, 2017).

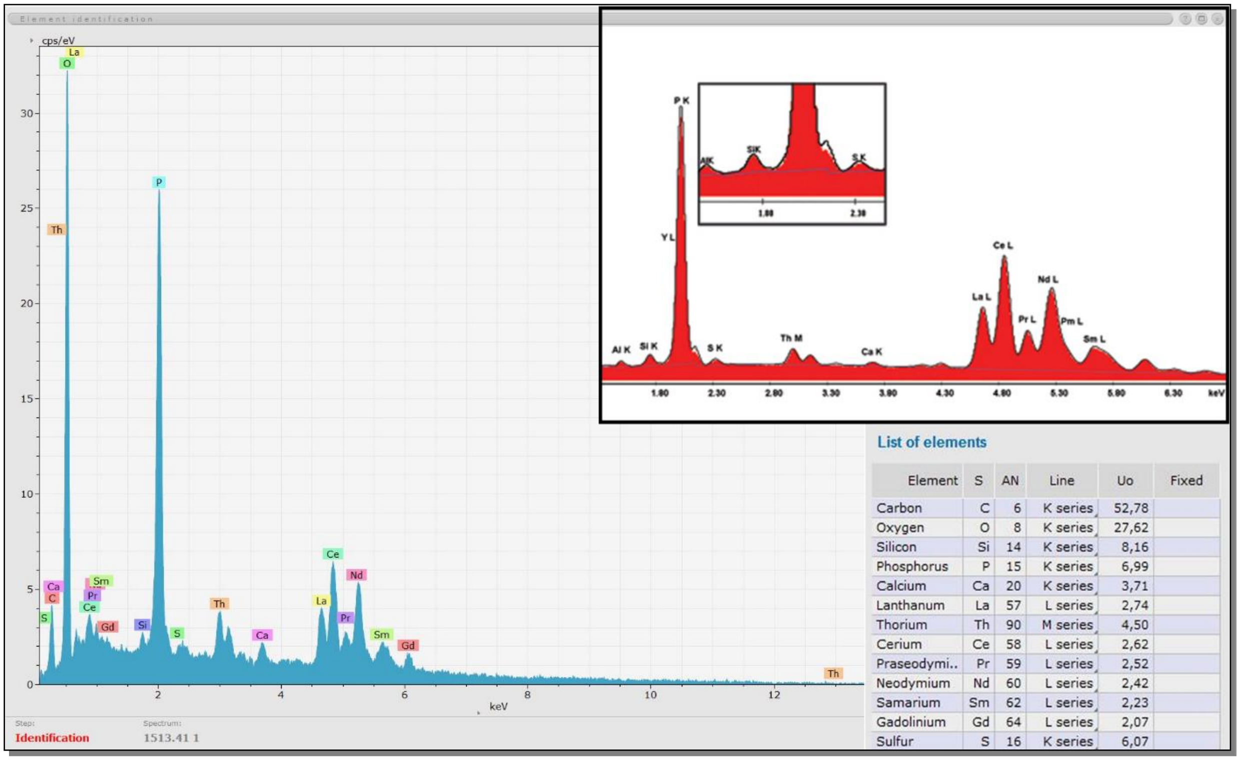

List of elements

Element	S	AN	Line	Uo	Fixed
Carbon	C	6	K series	52,78	
Oxygen	O	8	K series	27,62	
Silicon	Si	14	K series	8,16	
Phosphorus	P	15	K series	6,99	
Calcium	Ca	20	K series	3,71	
Lanthanum	La	57	L series	2,74	
Thorium	Th	90	M series	4,50	
Cerium	Ce	58	L series	2,62	
Praseodymi..	Pr	59	L series	2,52	
Neodymium	Nd	60	L series	2,42	
Samarium	Sm	62	L series	2,23	
Gadolinium	Gd	64	L series	2,07	
Sulfur	S	16	K series	6,07	

FIGURE 58: EDS SPECTRA SHOWING THE MONAZITE FOUND IN THE THIN SECTION SAMPLE TO THE LEFT AND A CONFIRMED MONAZITE IN THE UPPER RIGHT CORNER. NOTE THAT THE OXYGEN-PEAK IS MISSING FROM THE RIGHT IMAGE.

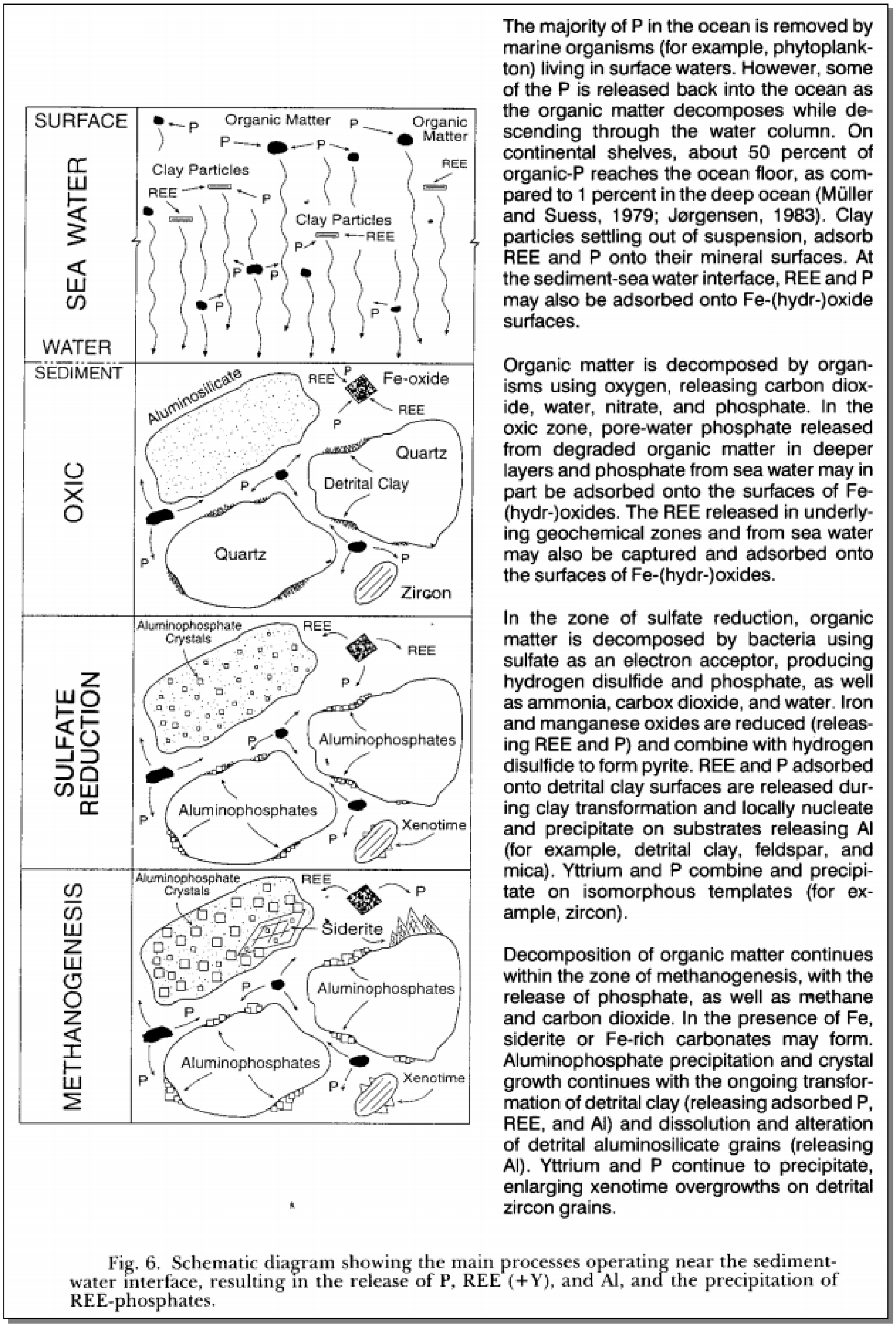

The majority of P in the ocean is removed by marine organisms (for example, phytoplankton) living in surface waters. However, some of the P is released back into the ocean as the organic matter decomposes while descending through the water column. On continental shelves, about 50 percent of organic-P reaches the ocean floor, as compared to 1 percent in the deep ocean (Müller and Suess, 1979; Jørgensen, 1983). Clay particles settling out of suspension, adsorb REE and P onto their mineral surfaces. At the sediment-sea water interface, REE and P may also be adsorbed onto Fe-(hydr-)oxide surfaces.

Organic matter is decomposed by organisms using oxygen, releasing carbon dioxide, water, nitrate, and phosphate. In the oxic zone, pore-water phosphate released from degraded organic matter in deeper layers and phosphate from sea water may in part be adsorbed onto the surfaces of Fe-(hydr-)oxides. The REE released in underlying geochemical zones and from sea water may also be captured and adsorbed onto the surfaces of Fe-(hydr-)oxides.

In the zone of sulfate reduction, organic matter is decomposed by bacteria using sulfate as an electron acceptor, producing hydrogen disulfide and phosphate, as well as ammonia, carbox dioxide, and water. Iron and manganese oxides are reduced (releasing REE and P) and combine with hydrogen disulfide to form pyrite. REE and P adsorbed onto detrital clay surfaces are released during clay transformation and locally nucleate and precipitate on substrates releasing Al (for example, detrital clay, feldspar, and mica). Yttrium and P combine and precipitate on isomorphous templates (for example, zircon).

Decomposition of organic matter continues within the zone of methanogenesis, with the release of phosphate, as well as methane and carbon dioxide. In the presence of Fe, siderite or Fe-rich carbonates may form. Aluminophosphate precipitation and crystal growth continues with the ongoing transformation of detrital clay (releasing adsorbed P, REE, and Al) and dissolution and alteration of detrital aluminosilicate grains (releasing Al). Yttrium and P continue to precipitate, enlarging xenotime overgrowths on detrital zircon grains.

Fig. 6. Schematic diagram showing the main processes operating near the sediment-water interface, resulting in the release of P, REE (+Y), and Al, and the precipitation of REE-phosphates.

FIGURE 59: OVERVIEW OF PROCESSES INVOLVED IN AUTHIGENIC DEVELOPMENT OF REE-AL-PHOSPHATES. REPRODUCED WITH THE KIND PERSMISSION OF BIRGER RASMUSSEN (RASMUSSEN, 1996).

Sylvite and halite were observed with near perfect crystals in both the Nordmela and Fruholmen Formations. These typical evaporite-minerals are assumed to be a result of the KCl/polymer water based mud used during drilling from 818m to 2514m in the studied well. The flushed zone had its porewater replaced by drilling mud and it follows that the chemical equilibrium was altered which might have led to the precipitation of sylvite and halite crystals.

The temperatures the formation has gone through as evident by the diagenetic processes is 130 °C or higher, yet the thin sections studied for the Nordmela and Fruholmen formations are taken from depths of around 1.5km. Only geothermal gradients from mid ocean ridges are high enough to explain this temperature-depth relationship, but as no known geothermal gradients from sedimentary basins are high enough to explain the relationship observed, it appears like that uplift has occurred. This conceptualized uplift is also described in the geological introduction of this study (Ohm et al., 2008).

Even given a geothermal gradient of 38 °C/km (Smelror et al., 2014), close to 2km of uplift must have occurred to yield temperatures above 130 °C in the Nordmela and Fruholmen formations.

$$\frac{130\ °C}{38°C/km} - 1.5km \approx 1.92\text{km}$$

It is otherwise highly unlikely the observed reactions could have taken place at 1.5km depth where the samples were acquired.

Comparison between the formations and reservoir quality

Of the three formations, the Nordmela Formation has the highest average porosity value measured, with the Fruholmen Formation coming in second and the Snadd Formation with the lowest porosity (see Tables **2** and **3**). The Fruholmen Formation should be discussed as three parts because the clayey upper and lower sequences (Krabbe and Akkar) are drastically different than the sandy middle sequence (Reke). The Snadd Formation has near-zero porosity due to the pore-filling calcite, but contains most of the same minerals as the other formations.

When it comes to minerals, the contents of the formations are very similar. Domination of monocrystalline quartz grains followed by K-feldspar grains in various stages of dissolution are characteristic of all formations. The amount of dissolved feldspar varies between the formations, with the Fruholmen Formation having the highest amount of observable dissolution and also the highest amount of kaolinite. The Snadd Formation has the least amount of kaolinite with the Nordmela Formation having kaolinite content closer to the Fruholmen Formation than the Snadd Formation. Plagioclase grains is present in all formations, with illitization of the grains the most frequent in the Fruholmen formation, less so in the Nordmela formation and absent in the Snadd formation. The plagioclase is mainly diagenetic albite, with only a few grains showing twinning under cross polarized light.

The clay content is higher in the Fruholmen Formation than in the Nordmela Formation, but the clay is concentrated in laminations and as clusters of kaolinite where K-feldspar grains have been. As such, the clay does not reduce the effective porosity much, but instead affects permeability negatively. The Snadd Formation also contains clay laminations, although the laminations have negligible effect on permeability as the porosity is around 1-2%. Some fractures are observed in the Snadd formation, but these might have occurred during sample preparation and should not be assumed to represent reservoir porosity.

The Nordmela Formation has an average porosity higher than the other formations, but the sandy sequences from which the samples are taken are not thick. With only a few tens of centimetres between the clay laminations at maximum, vertical permeability would be low and production would be adversely affected. The overall reservoir potential therefore appears to be low, with the sandy sequences having fair reservoir potential.

The Fruholmen Formation has varying porosity due to the tripartite nature of the formation, with the upper and lower sequences having higher clay content and frequent laminations. For this reason, the author considers the overall reservoir potential to be fair, with the middle Reke Member sequence having good reservoir potential due to several metres of uninterrupted sand deposits. The upper Krabbe Member sequence has poor reservoir potential due to frequent clay laminations every few centimetres.

The Snadd Formation has very poor reservoir potential due to pore filling calcite matrix and cement as well as silt-sized framework grains leading to tight pore throats which reduces the permeability further.

Conclusion

The formation sandstones studied have a highly similar content of detrital grains, with the main differences being in the types and quantities of diagenetic minerals.

Evidence of compaction, diagenetic cementation, dissolution, alteration and replacement was found in the study of the formation sandstones. The [K-feldspar → Kaolinite → Illite + Albite] reaction route is observed in the thin sections, which along with other reactions gives a good estimate of minimum temperature. The dissolution of K-feldspar has provided secondary porosity for diagenetic minerals to grow in. The diagenetic processes observed suggest temperatures of at least 130 °C which implies an uplift of close to 2km.

The observed pyrite-siderite transition is a key indicator of marine origin and the core photos show signs of bioturbation in the Nordmela Formation. The pyrite is interpreted as being formed in the sulphate reduction zone, and along with kaolinite, Mg-poor calcite and florencite it is found to be of eogenetic origin. Siderite and ankerite form after the sulphate reduction zone and are thought to be formed in the transition zone from the eogenetic to the mesogenetic conditions. Syntaxial quartz overgrowths, illite, dickite and authigenic albite are thought to be of mesogenetic origin based on the temperatures required for these reactions. As Mg-rich calcite is found to envelop syntaxial quartz overgrowths, it is thought to have formed after the quartz cementation and likely during mesogenesis or telogenesis.

Porosity loss by quartz cementation is observed in all formations using CL. The more mineralogically mature sections have significant porosity loss from higher volumes of diagenetic quartz overgrowths due to a higher content of detrital quartz. The less mature sections have lost significant porosity to carbonate cementation and less to quartz cementation. The overall porosity reducing diagenetic mineral is quartz cement, with roughly 30% of the quartz grains being quartz overgrowths. Diagenetic florencite cement is also observed as overgrowths on quartz grains in the Nordmela Formation's most mature thin section sample, and it appears to have precipitated after the quartz cementation. In addition, >90% of the albite observed is found to be authigenic and often appears matrix-like in the way it fills pores between other grains, causing further porosity loss. Mineral observations suggest significant amounts of detrital Ca-plagioclase has been present in the formation and altered into authigenic albite and calcites. Illite is frequently found in all formations in both pore-lining and pore-bridging forms, leading to low permeabilities for the already low-porosity formations.

The reservoir potential of the Nordmela and Fruholmen Formation intervals studied in this paper are on the lower end of the porosity scale with poor permeabilities and no thin sections showing more than 13% porosity (KLONK measurements), excluding micro-porosity. The middle Fruholmen Formation sequence has the best reservoir potential due to its middle Reke Member sandy sequence with few mud/clay laminations and good porosity. The Nordmela Formation has a higher average porosity, but comes in second for reservoir potential because of its thin sand sequences and frequent mud/clay laminations which would inhibit hydrocarbon flow during production. The Snadd Formation interval studied has very poor reservoir conditions due to the pore-filling carbonates and silt-sized grains, with a mineralogically immature makeup.

Future research

As for further research, the author suggests the following courses of action:

1. Use of drilled cores to create a sedimentological log tailor made for the 7321/8-1 well.
2. Use of X-ray to acquire elemental composition intensity map of grains in order to quantify amount of quartz vs non-twinned albite.

References

Beaufort, D., Cassagnabere, A., Petit, S., Lanson, B., Berger, G., Lacharpagne, J., & Johansen, H. (1998). Kaolinite-to-dickite reaction in sandstone reservoirs. *Clay minerals, 33*(2), 297-316.

Bjørlykke, K. (1998). Clay mineral diagenesis in sedimentary basins—a key to the prediction of rock properties. Examples from the North Sea Basin. *Clay minerals, 33*(1), 15-34.

Bjørlykke, K., & Jahren, J. (2010). *Sandstones and sandstone reservoirs* (Vol. Petroleum Geoscience:: From Sedimentary Environments to Rock Physics): Springer.

Dalland, A., Worsley, D., & Ofstad, K. (1988). NPD-bulletin no. 4: A Lithostrategraphic scheme for the Mesozoic and Cenozoic succession offshore mid- and northern Norway. Retrieved from http://www.npd.no/Global/Norsk/3-Publikasjoner/NPD-Bulletin/NPD_BulletinNo4.pdf

Dott Jr, R. H. (1964). Wacke, Graywacke and Matrix--What Approach to Immature Sandstone Classification? *Journal of Sedimentary Research, 34*(3), 625-632.

EDAX. (2017). Phosphorus - Energy Dispersive Spectroscopy (EDS). Retrieved from http://www.edax.com/periodic-table/phosphorus-eds.aspx

Folk, R. L. (1951). Stages of textural maturity in sedimentary rocks. *Journal of Sedimentary Research, 21*(3).

Gabrielsen, R. H., Færseth, R. B., Jensen, L. N., Kalheim, J. E., & Riis, F. (1990). NPD bulletin no. 6: Structural elements of the Norwegian continental shelf. Retrieved from http://www.npd.no/global/norsk/3-publikasjoner/npd-bulletin/npd_bulletinnr6.pdf

Hanaor, D. A., & Sorrell, C. C. (2011). Review of the anatase to rutile phase transformation. *Journal of Materials science, 46*(4), 855-874.

Houseknecht, D. W. (1991). Use of cathodoluminescence petrography for understanding compaction, quartz cementation, and porosity in sandstones. *Society for Sedimentary Geology, SEPM Short Course 25 - Luminescence Microscopy and Spectroscopy: Qualitative and Quantitative Applications*, 59-68.

Irwin, H., Curtis, C., & Coleman, M. (1977). Isotopic evidence for source of diagenetic carbonates formed during burial of organic-rich sediments. *Nature, 269*(5625), 209-213.

Johansen, S., Ostisty, B., Birkeland, Ø., Fedorovsky, Y., Martirosjan, V., Christensen, O. B., . . . Margulis, L. (1992). Hydrocarbon potential in the Barents Sea region: play distribution and potential. *Arctic Geology and Petroleum Potential, Norwegian Petroleum Society (NPF), Special Publication, 2*, 273-320.

Kantorowicz, J. D. (1990). The influence of variations in illite morphology on the permeability of Middle Jurassic Brent Group sandstones, Cormorant Field, UK North Sea. *Marine and Petroleum Geology, 7*(1), 66-74. doi:http://dx.doi.org/10.1016/0264-8172(90)90057-N

Kitano, Y., Kanamori, N., & Tokuyama, A. (1969). Effects of organic matter on solubilities and crystal form of carbonates. *American Zoologist, 9*(3), 681-688.

Marello, L., Ebbing, J., & Gernigon, L. (2013). Basement inhomogeneities and crustal setting in the Barents Sea from a combined 3D gravity and magnetic model. *Geophysical Journal International, 193*(2), 557-584.

Ogg, G. (2013). Barents sea lithostratigraphic chart. Retrieved from http://www.nhm2.uio.no/norges/litho/Barents_Chart.html

Ohm, S. E., Karlsen, D. A., & Austin, T. (2008). Geochemically driven exploration models in uplifted areas: Examples from the Norwegian Barents Sea. *AAPG bulletin, 92*(9), 1191-1223.

Olaussen, S., Dalland, A., Gloppen, T., & Johannessen, E. (1984). Depositional environment and diagenesis of Jurassic reservoir sandstones in the eastern part of Troms I area *Petroleum Geology of the North European Margin* (pp. 61-79): Springer.

Oljedirektoratet. (2005). Wellbore Exploration 7321/8-1. Retrieved from http://factpages.npd.no/ReportServer?/FactPages/PageView/wellbore_exploration&rs:Command=Render&rc:Toolbar=false&rc:Parameters=f&NpdId=1070&IpAddress=193.214.54.130&CultureCode=en

Oljedirektoratet. (2014a). 6.1 - Geology of the Barents Sea - Oljedirektoratet. Retrieved from http://www.npd.no/Publikasjoner/Rapporter/CO2-samleatlas/6-The-Barents-Sea/61-Geology-of-the-Barents-Sea/

Oljedirektoratet. (2014b). The Kapp Toscana Group - Realgrunnen Subgroup. Retrieved from http://www.npd.no/Publikasjoner/Rapporter/CO2-samleatlas/6-The-Barents-Sea/61-Geology-of-the-Barents-Sea/The-Kapp-Toscana-Group---Realgrunnen-Subgroup/

Pallatt, N., Wilson, J., & McHardy, B. (1984). The relationship between permeability and the morphology of diagenetic illite in reservoir rocks. *Journal of Petroleum Technology, 36*(12), 2225-2227.

Parsons, I. (2012). *Feldspars and their Reactions* (Vol. 421): Springer Science & Business Media.

Parsons, I., Thompson, P., Lee, M. R., & Cayzer, N. (2005). Alkali feldspar microtextures as provenance indicators in siliciclastic rocks and their role in feldspar dissolution during transport and diagenesis. *Journal of Sedimentary Research*, *75*(5), 921-942.

Rasmussen, B. (1996). Early diagenetic REE-phosphate minerals (florencite, gorceixite, crandallite, and xenotime) in marine sandstones: a major sink for oceanic phosphorus. *American Journal of Science, 296*(6), 601-632.

Rønning, H. (2011). *Petrography and diagenesis of the Jurassic sandstones of the Nordmela and Stø formations in the Bjørnøya East and Bjørnøya South area in the Barents Sea*. Department of Geology and Mineral Resources Engineering. Norwegian University of Science and Technology.

Smelror, M., Petrov, O., Larssen, G. B., & Werner, S. (2014). Geological history of the Barents Sea. *Norges Geol. undersøkelse*, 1-135.

Statoil. (2013). Snøhvit. Retrieved from http://www.statoil.com/no/TechnologyInnovation/NewEnergy/Co2CaptureStorage/Pages/Snohvit.aspx

Statsministerens-kontor. (2016, 2016-08-29). Oppstart av 24. konsesjonsrunde – invitasjon til å nominere blokker. https://www.regjeringen.no/no/aktuelt/ons2/id2509912/.

Storvoll, V., Bjørlykke, K., Karlsen, D., & Saigal, G. (2002). Porosity preservation in reservoir sandstones due to grain-coating illite: a study of the Jurassic Garn Formation from the Kristin and Lavrans fields, offshore Mid-Norway. *Marine and Petroleum Geology, 19*(6), 767-781.

Vorren, T. O., Richardsen, G., Knutsen, S.-M., & Henriksen, E. (1991). Cenozoic erosion and sedimentation in the western Barents Sea. *Marine and Petroleum Geology, 8*(3), 317-340. doi:http://dx.doi.org/10.1016/0264-8172(91)90086-G

Walderhaug, O., & Bjørkum, P. A. (2003). The effect of stylolite spacing on quartz cementation in the Lower Jurassic Stø Formation, southern Barents Sea. *Journal of Sedimentary Research*, *73*(2), 146-156.

Appendix A – CL photos

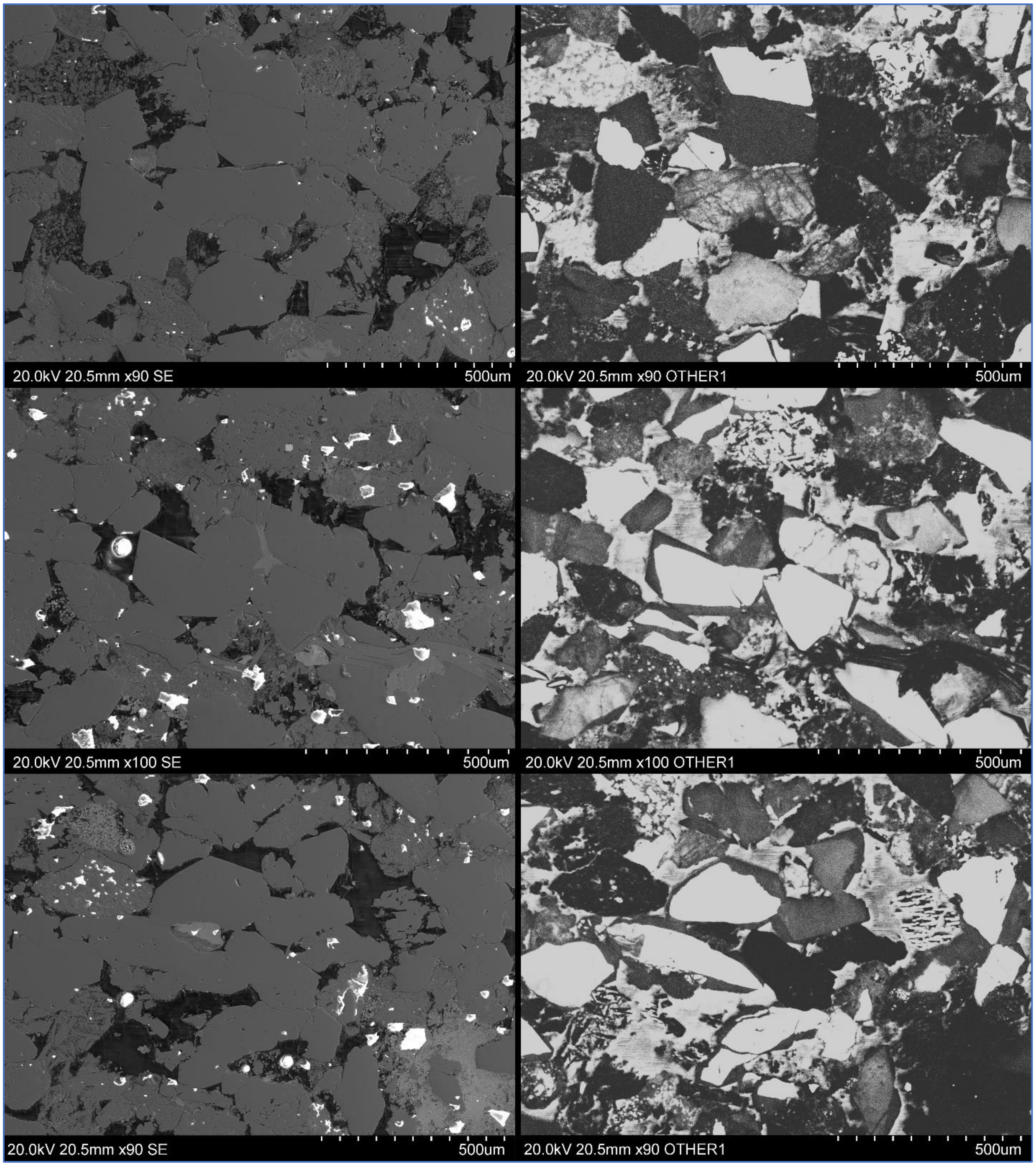

Appendix 1: SE vs CL photos at depth 1460.55m, Nordmela formation.

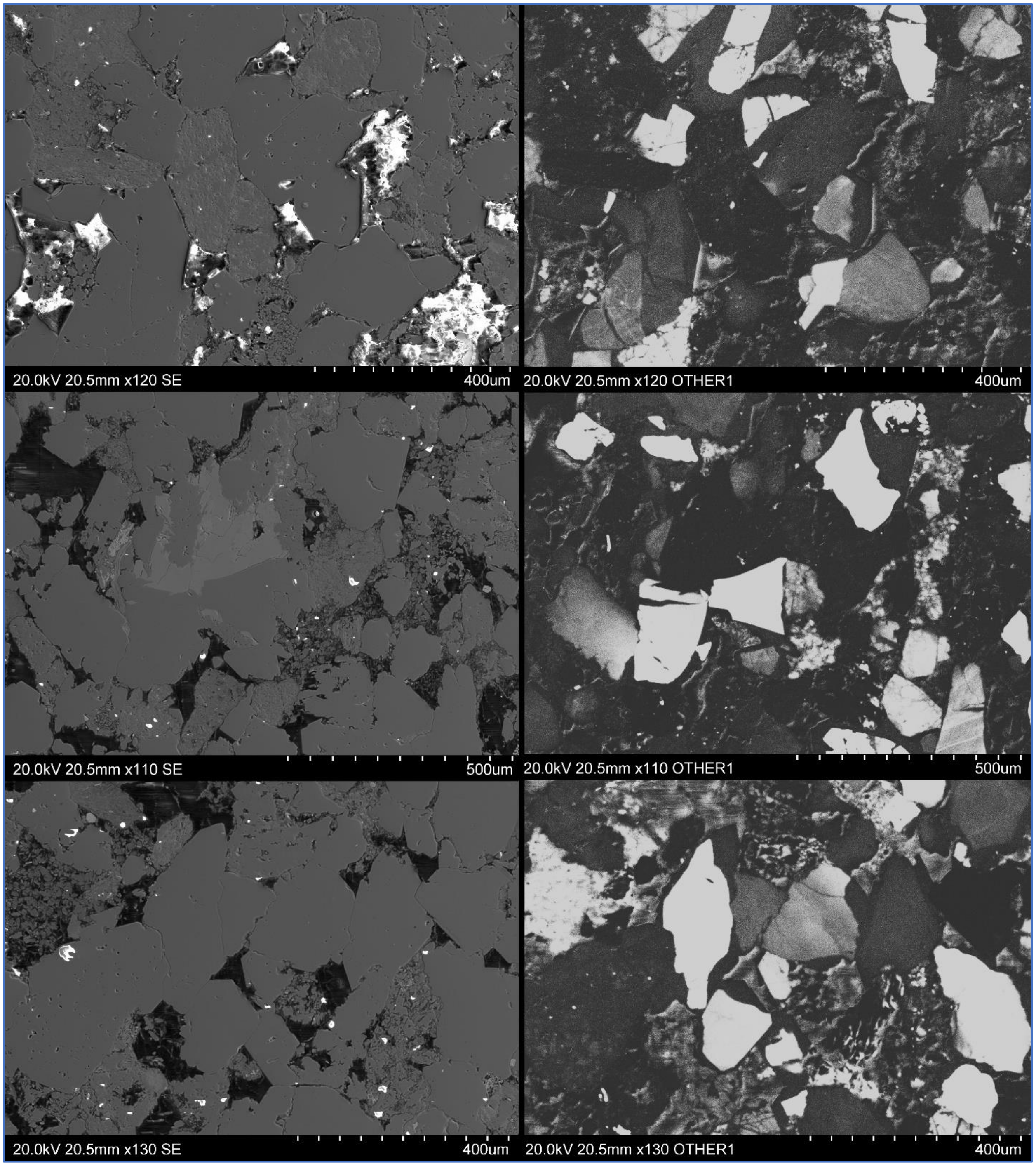

Appendix 2: SE vs CL photos at depth 1460.80m, Nordmela formation.

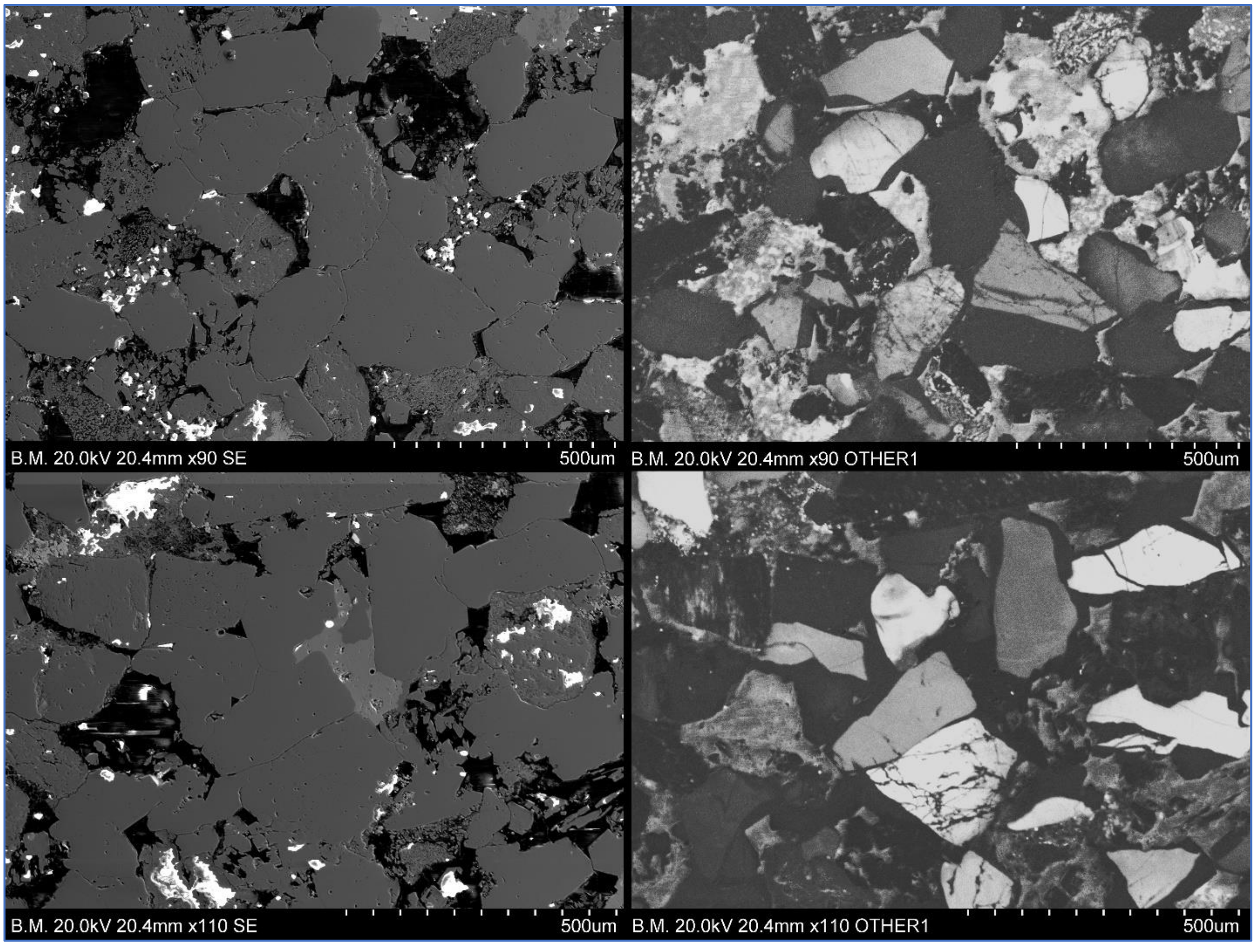

Appendix 3: SE vs CL photos at depth 1460.85m, Nordmela formation.

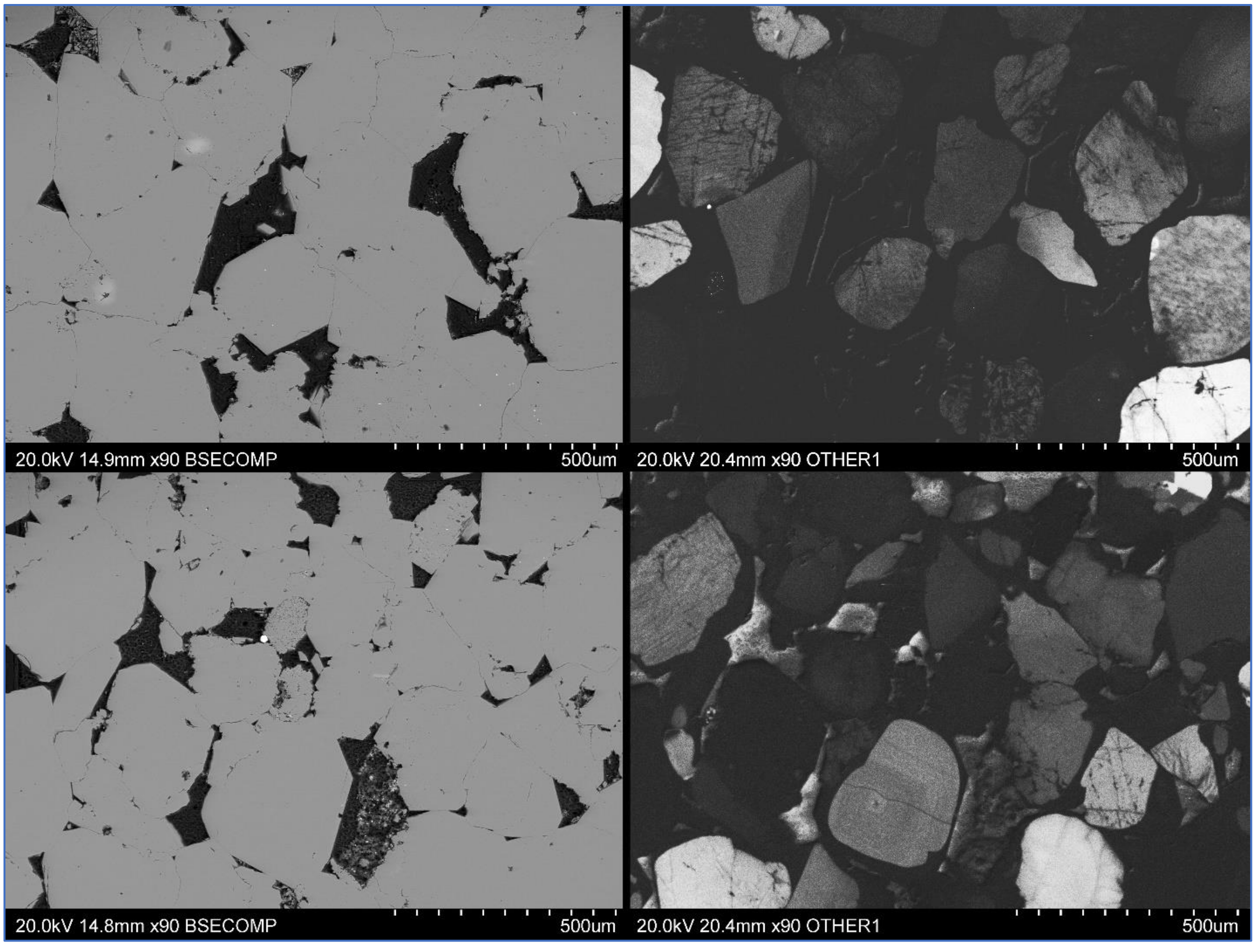

Appendix 4: BSE vs CL photos at depth 1463.70m part 1, Nordmela formation.

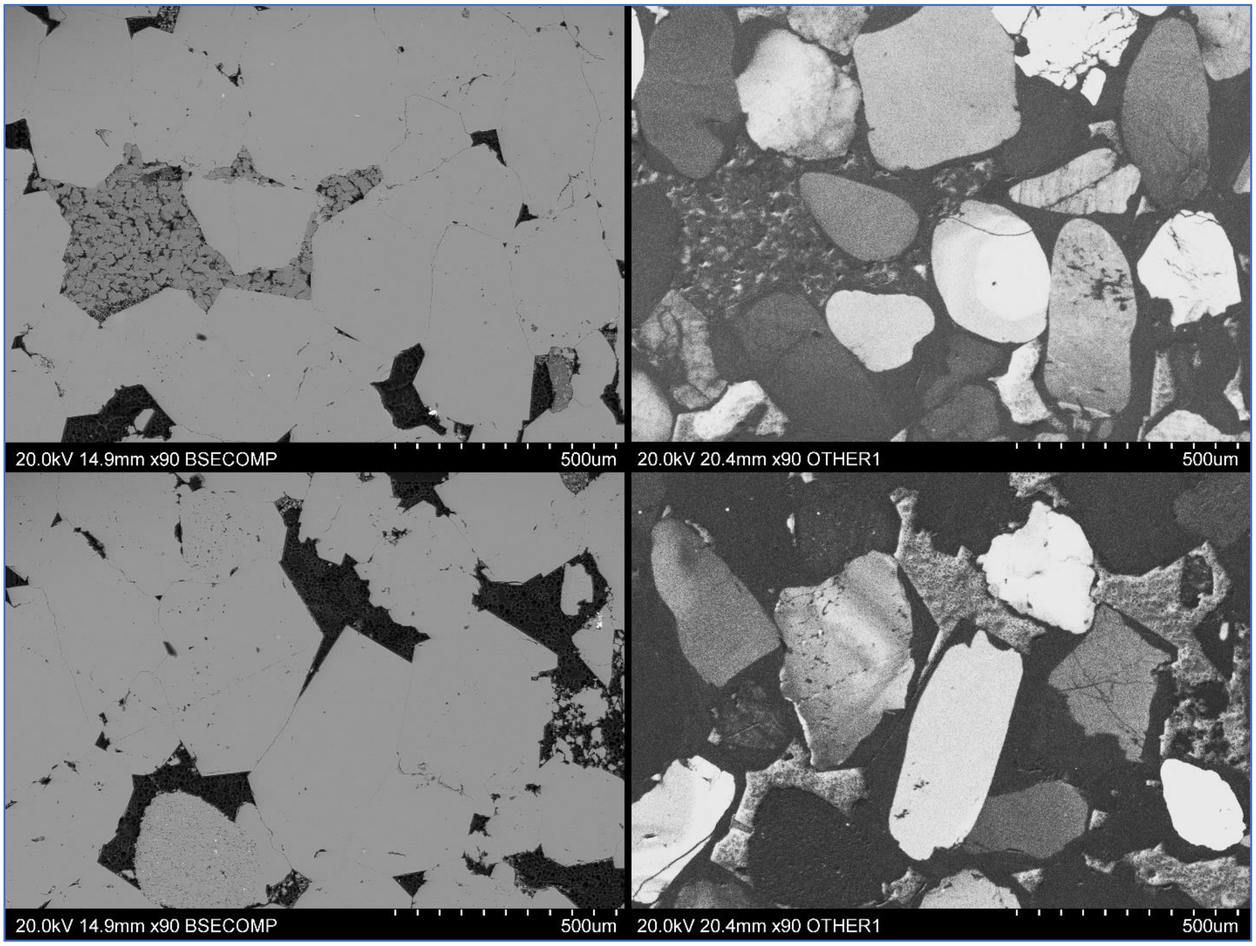

Appendix 5: BSE vs CL photos at depth 1463.70m part 2, Nordmela formation.

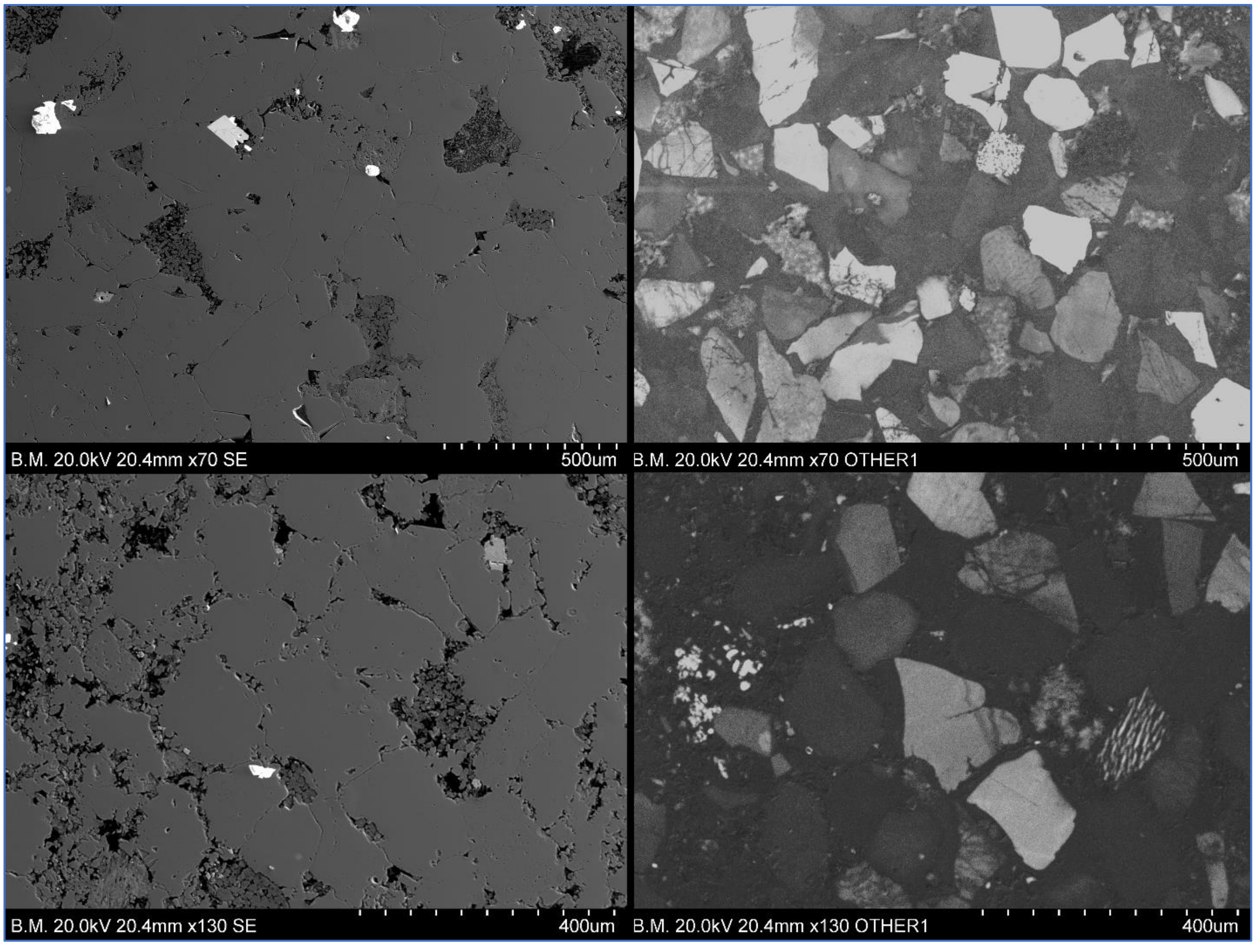

Appendix 6: SE vs CL photos at depth 1468.90m, Fruholmen formation.

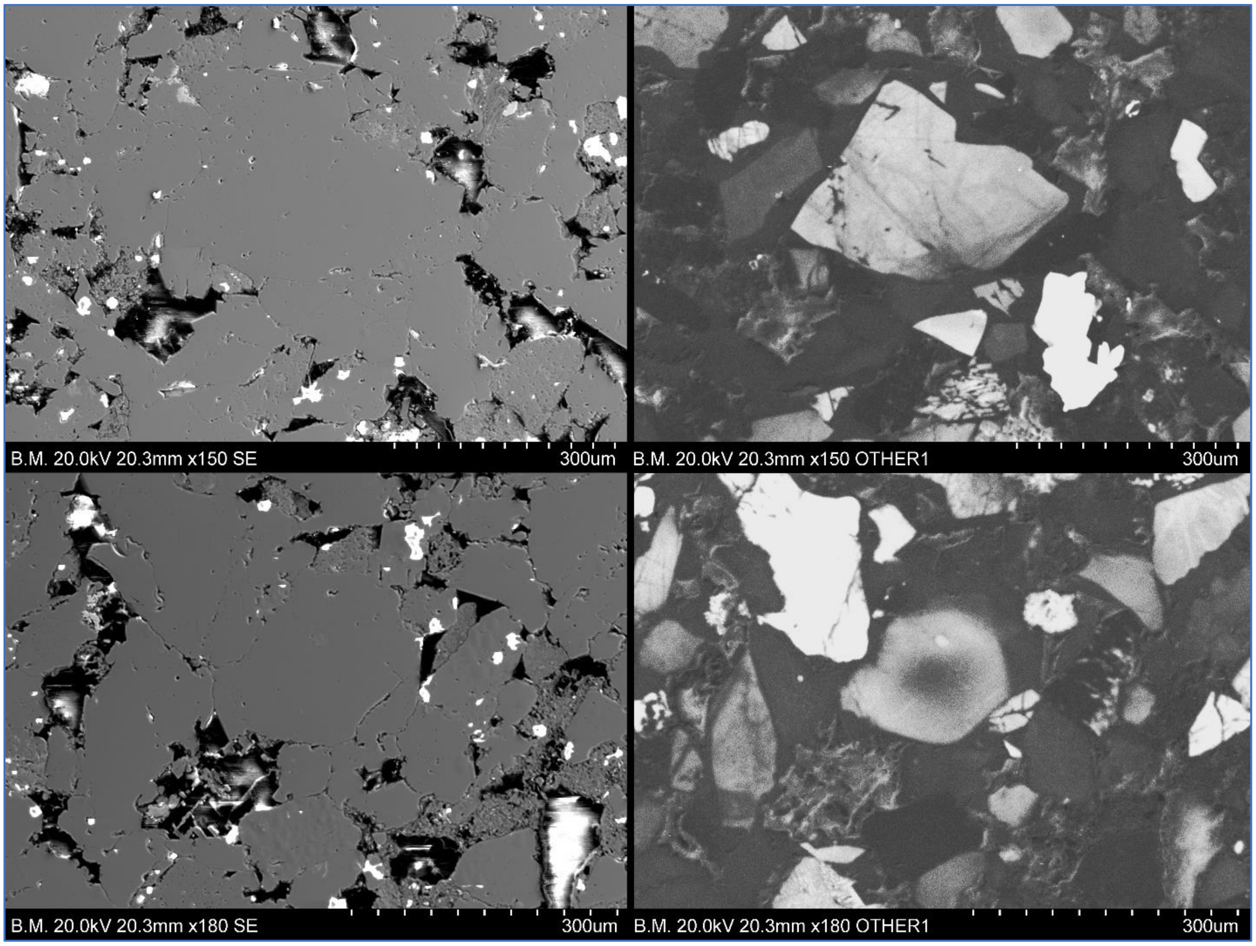

Appendix 7: SE vs CL photos at depth 1487.95m, Fruholmen formation.

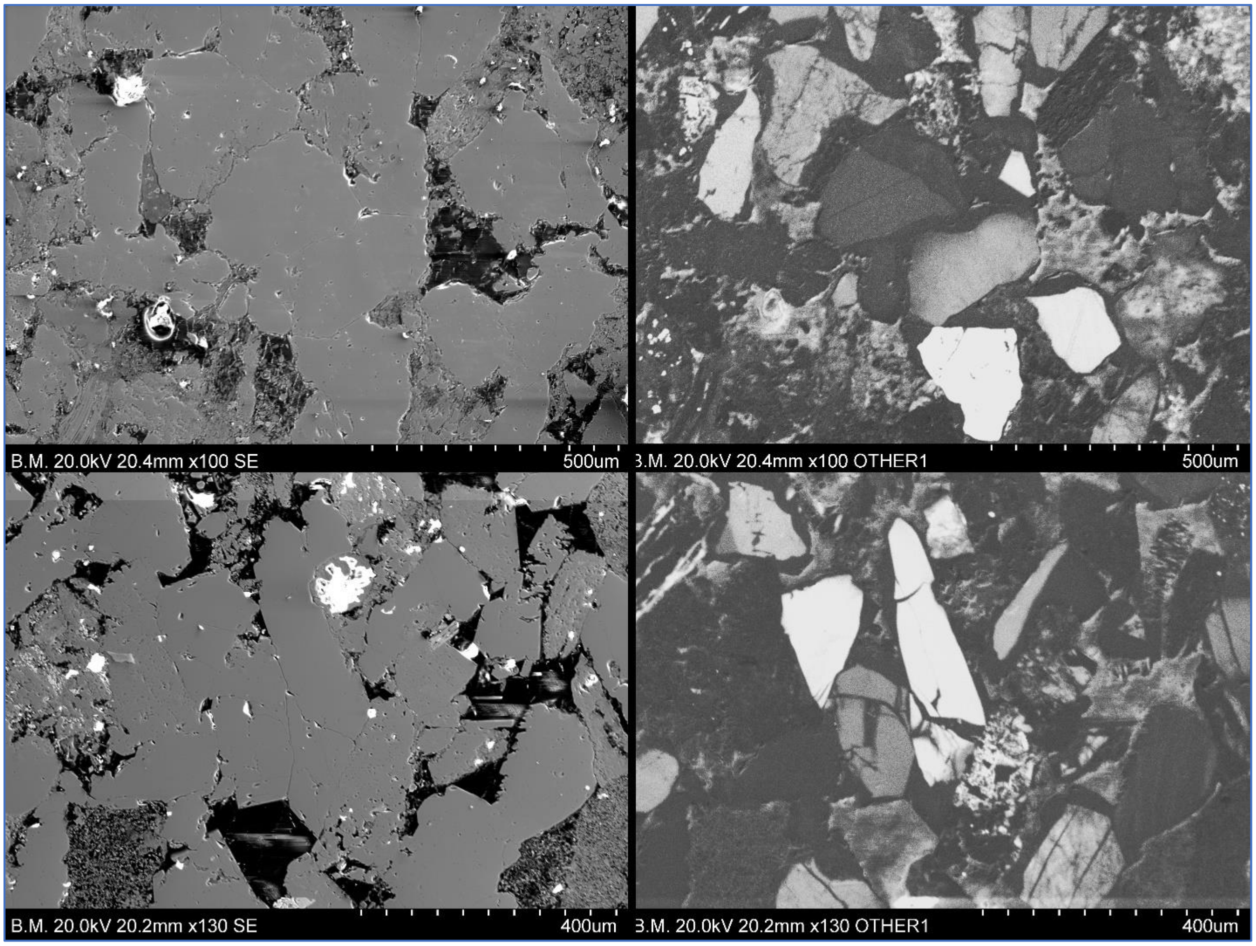

Appendix 8: SE vs CL photos at depth 1495.44m, Fruholmen formation.

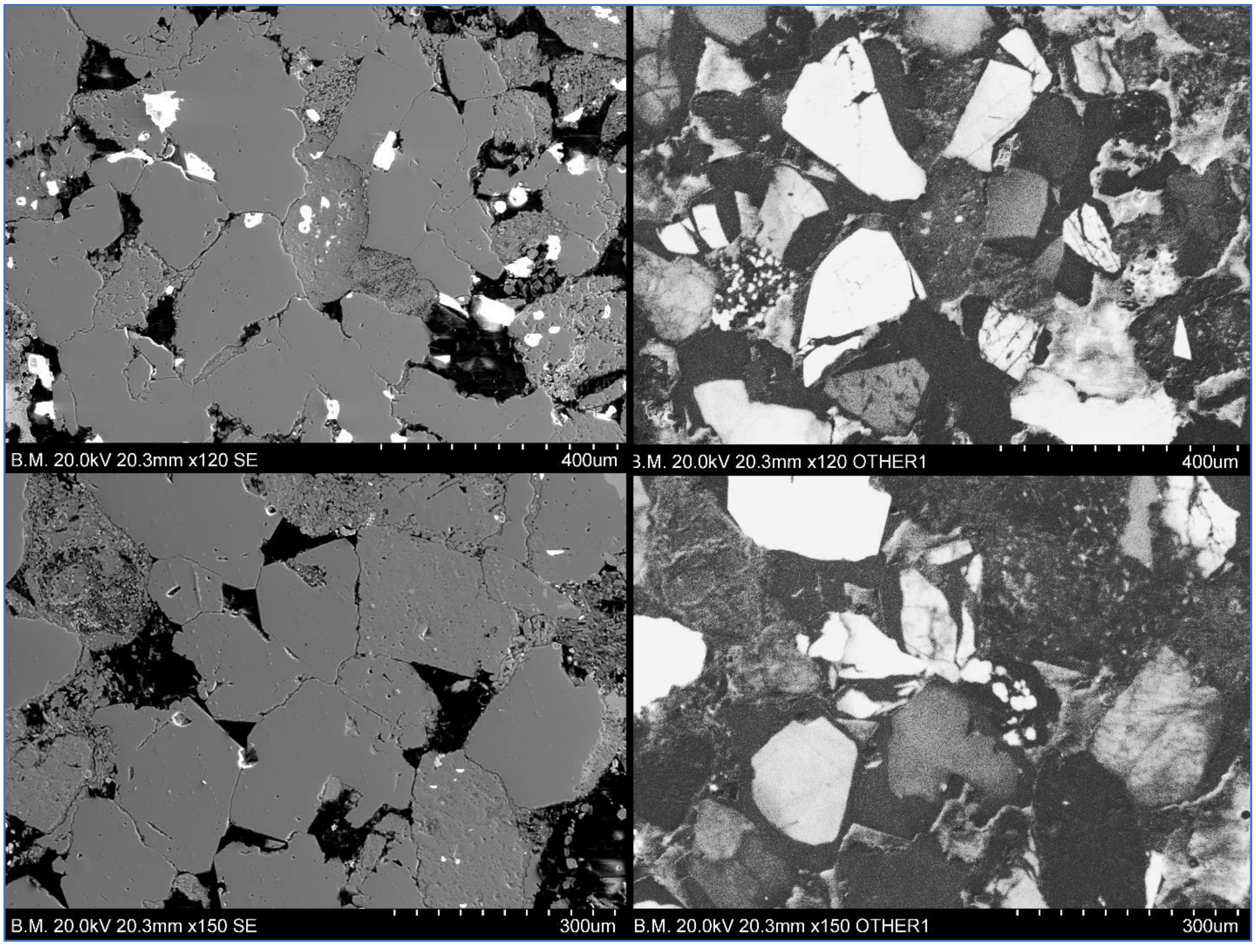

Appendix 9: SE vs CL photos at depth 1513.41m, Fruholmen formation.

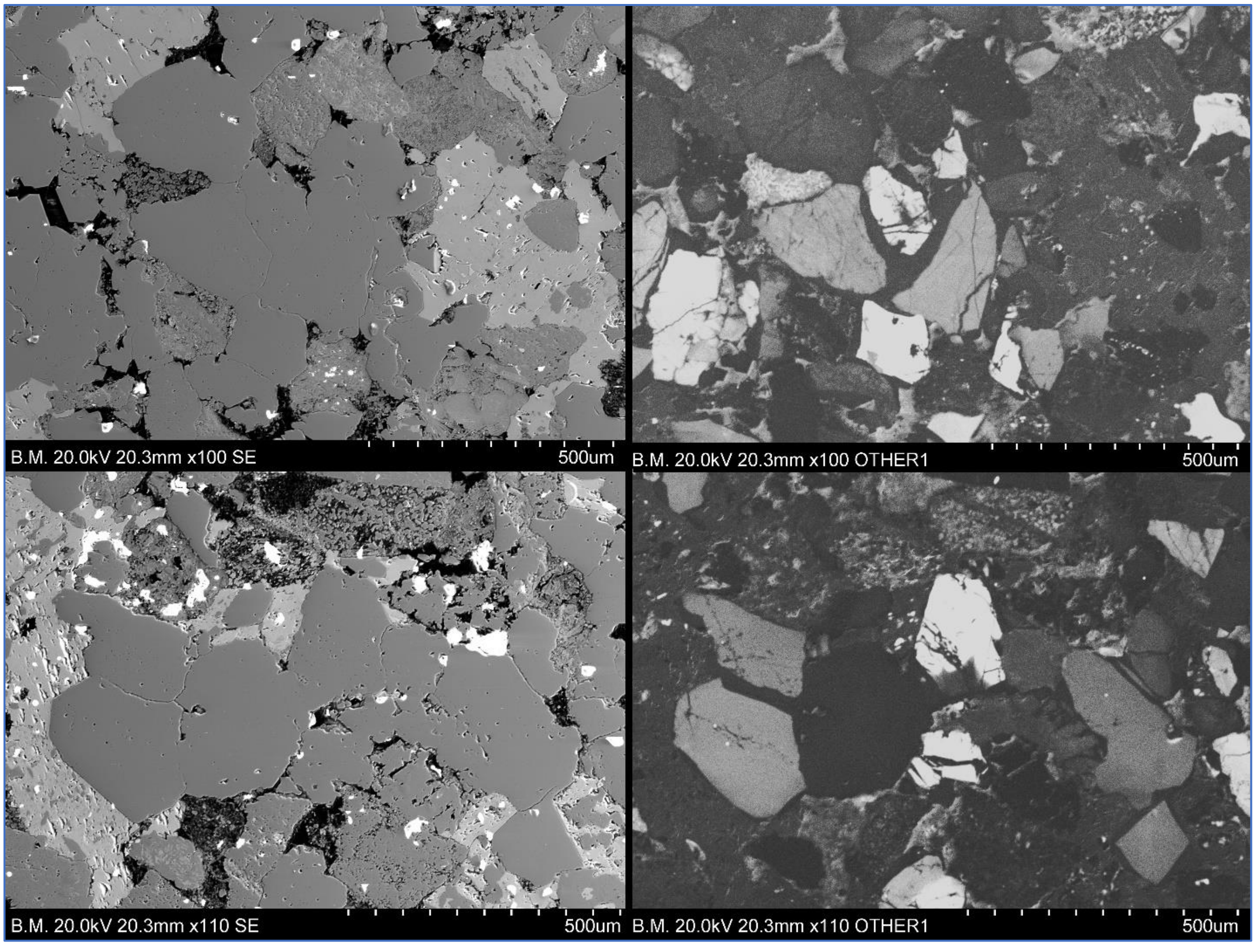

Appendix 10: SE vs CL photos at depth 1538.32m, Fruholmen formation.

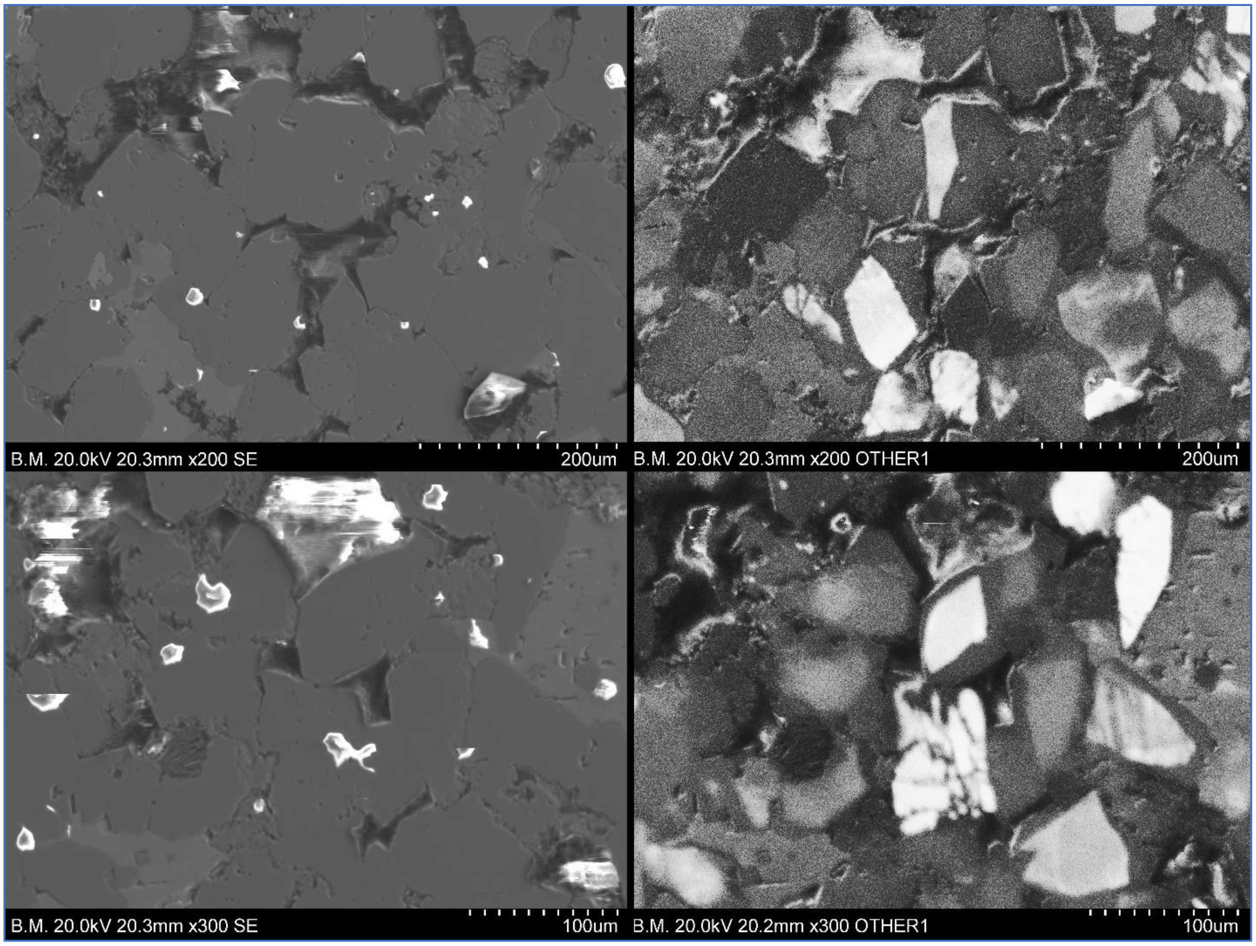

Appendix 11: SE vs CL photos at depth 1543.02m, Fruholmen formation

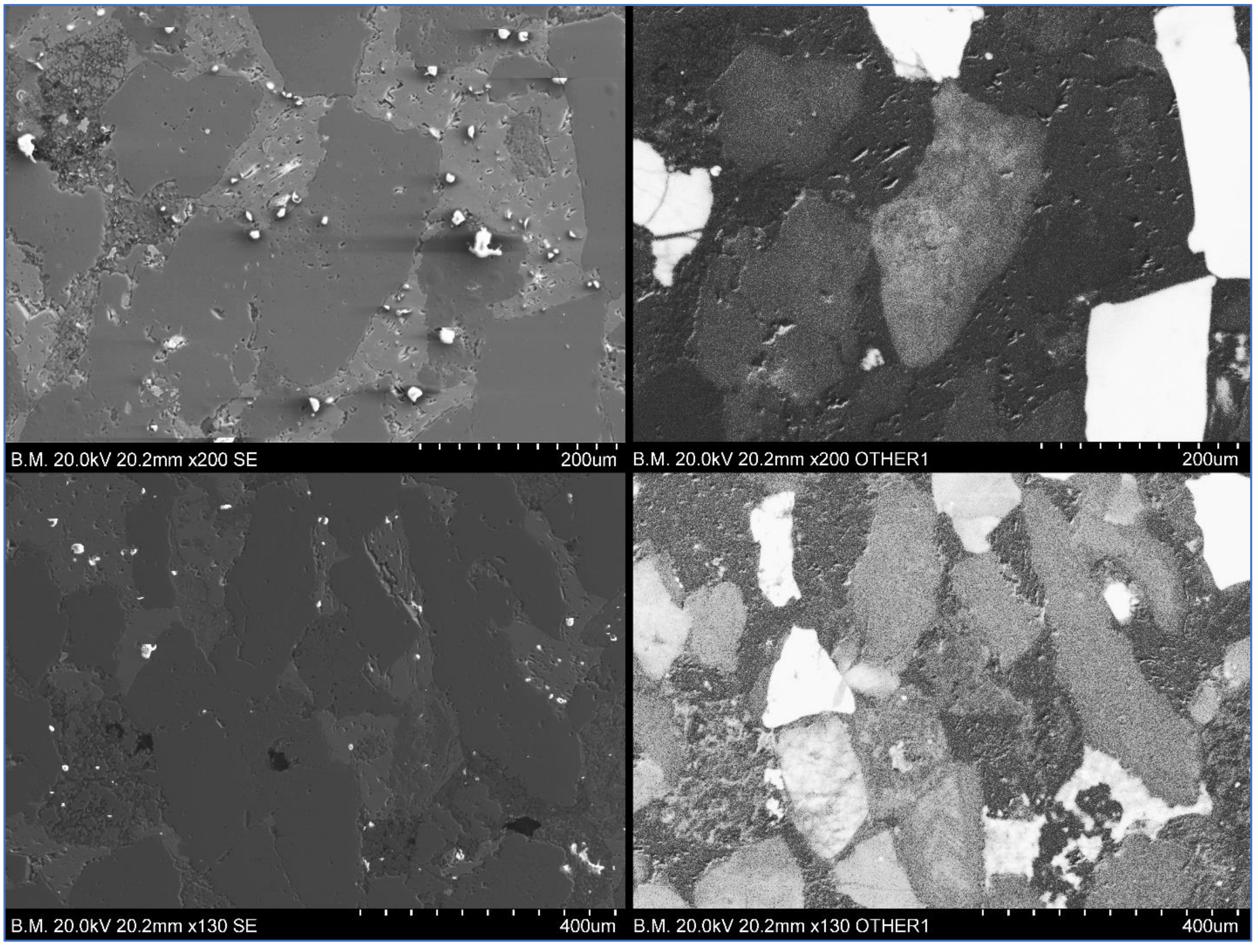

Appendix 12: SE vs CL photos at depth 2840.50m, Snadd formation.

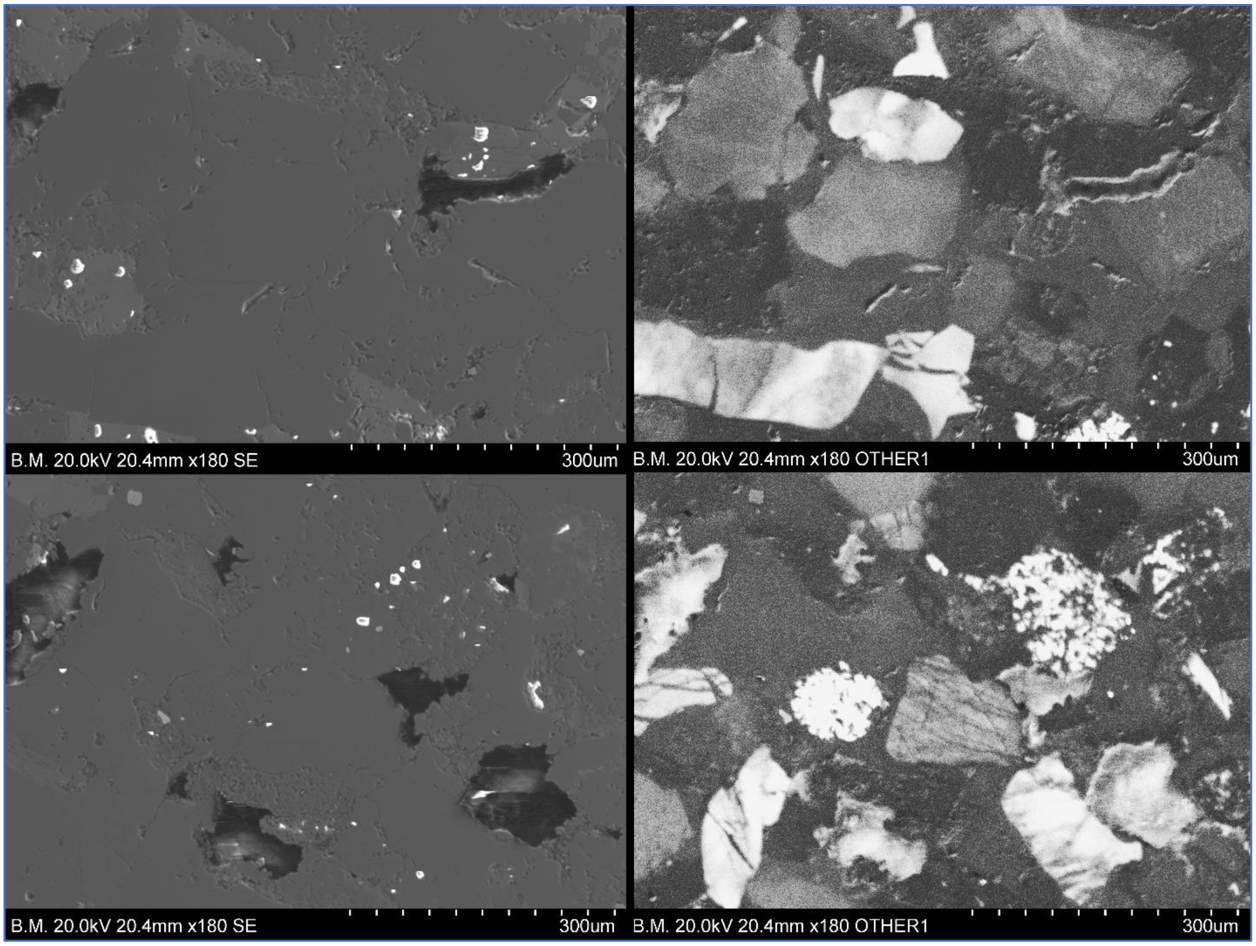

Appendix 13: SE vs CL photos at depth 2846.70m, Snadd formation.

Appendix B – EDS spectra

Appendix 14: Representative spectrum for quartz in all formations.

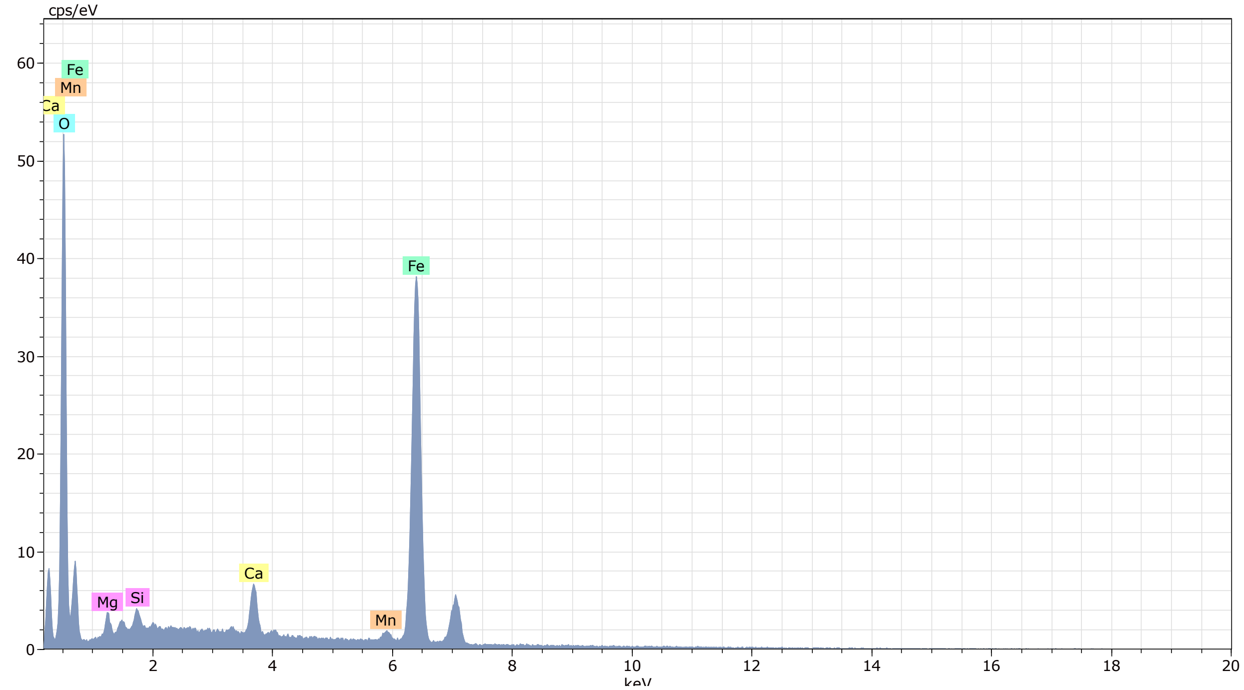

Appendix 15: Representative spectrum for siderite in all formations.

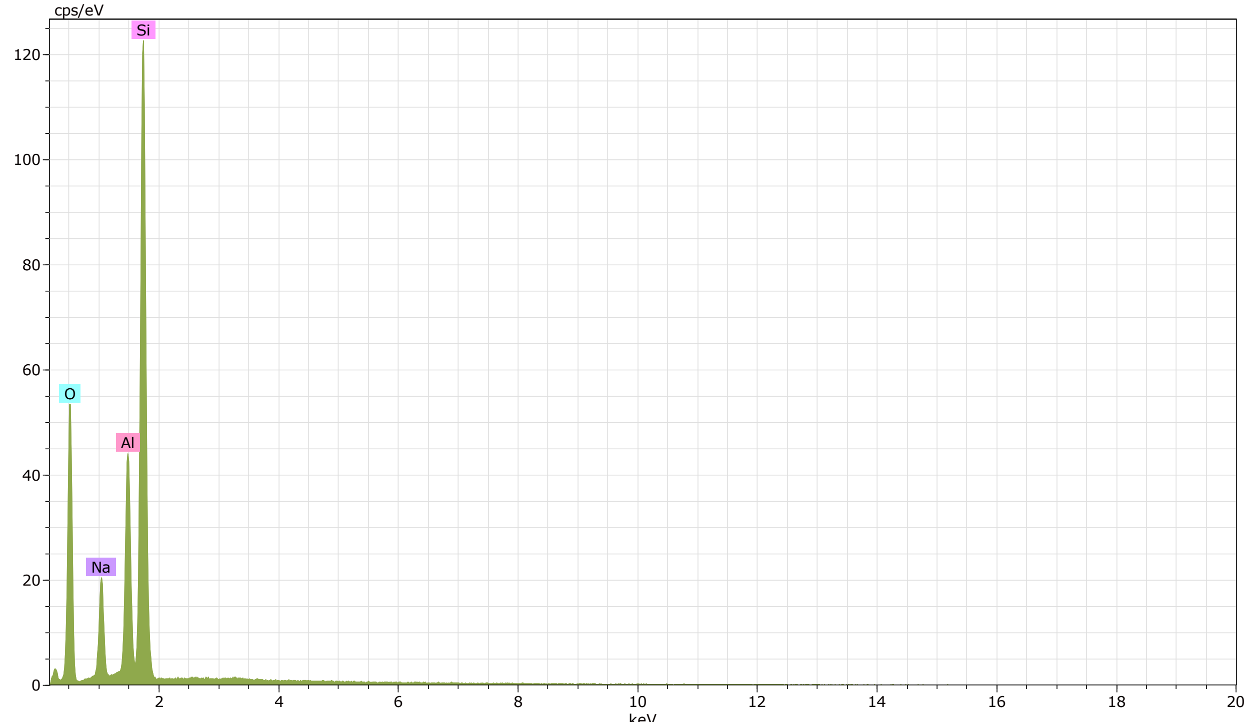

Appendix 16: Representative spectrum for albite in all formations.

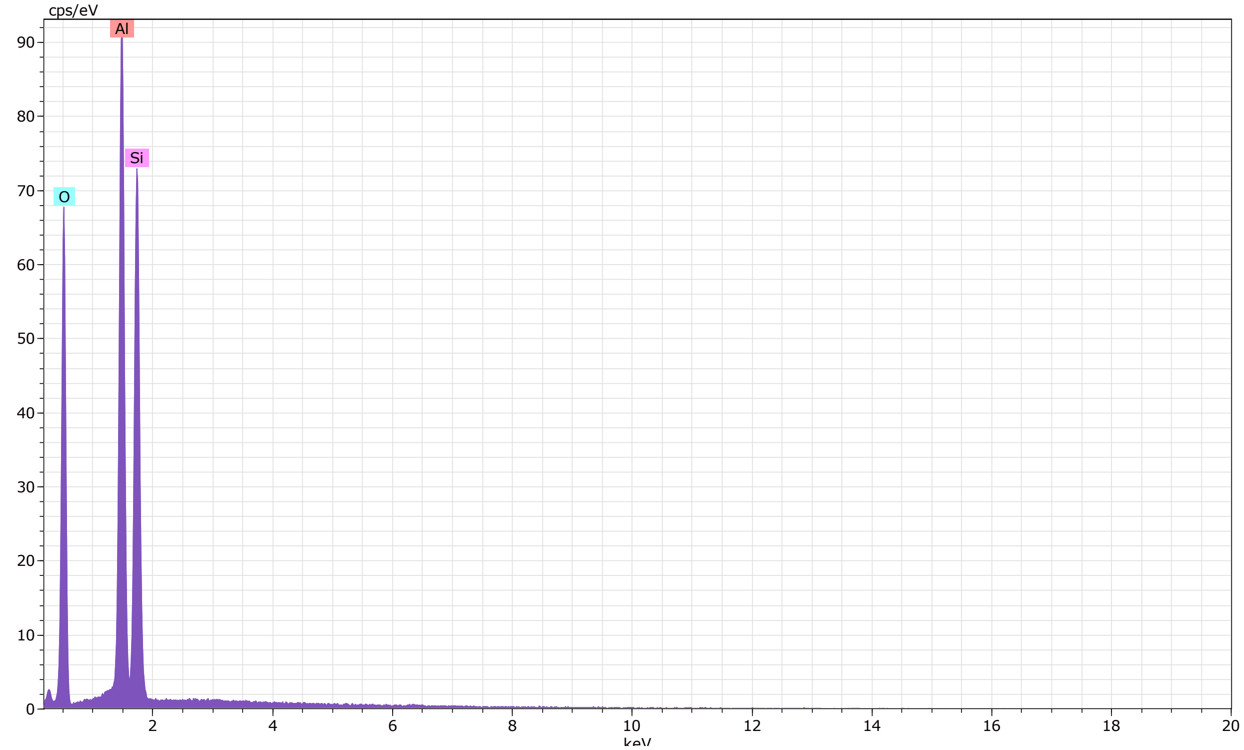

Appendix 17: Representative spectrum for kaolinite in all formations.

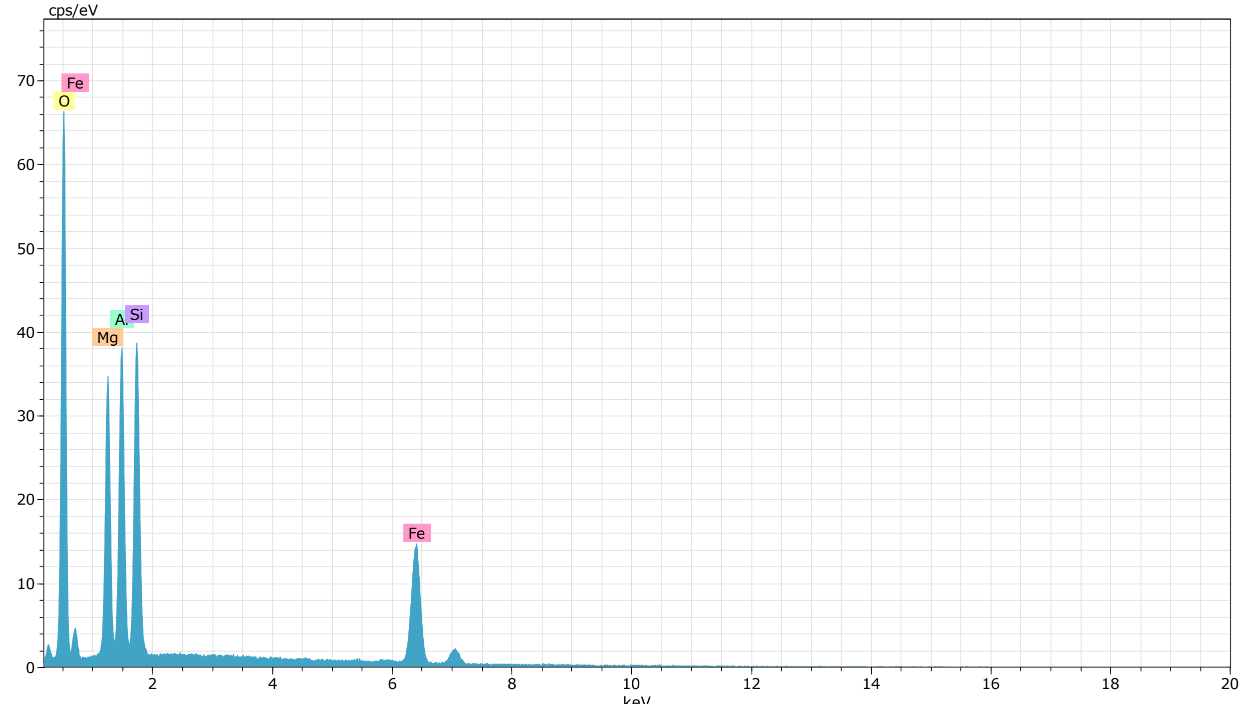

Appendix 18: Representative spectrum for chlorite in the Nordmela and Fruholmen Formations.

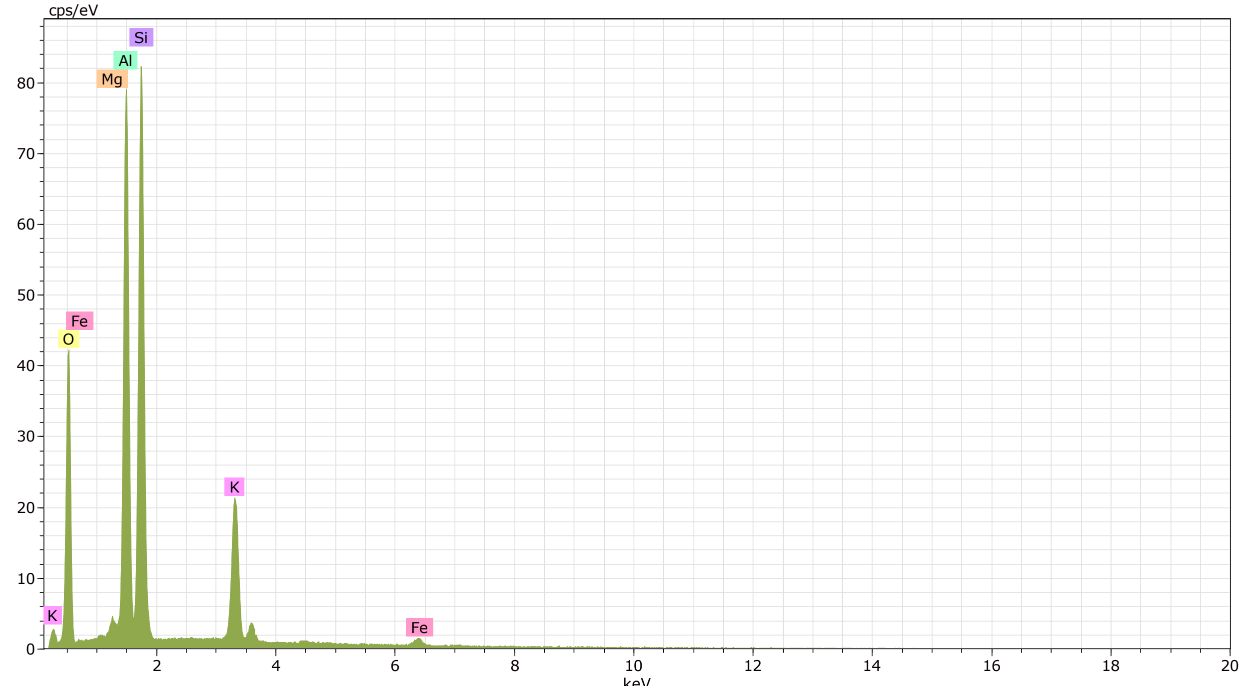

Appendix 19: Representative spectrum for illite in all formations.

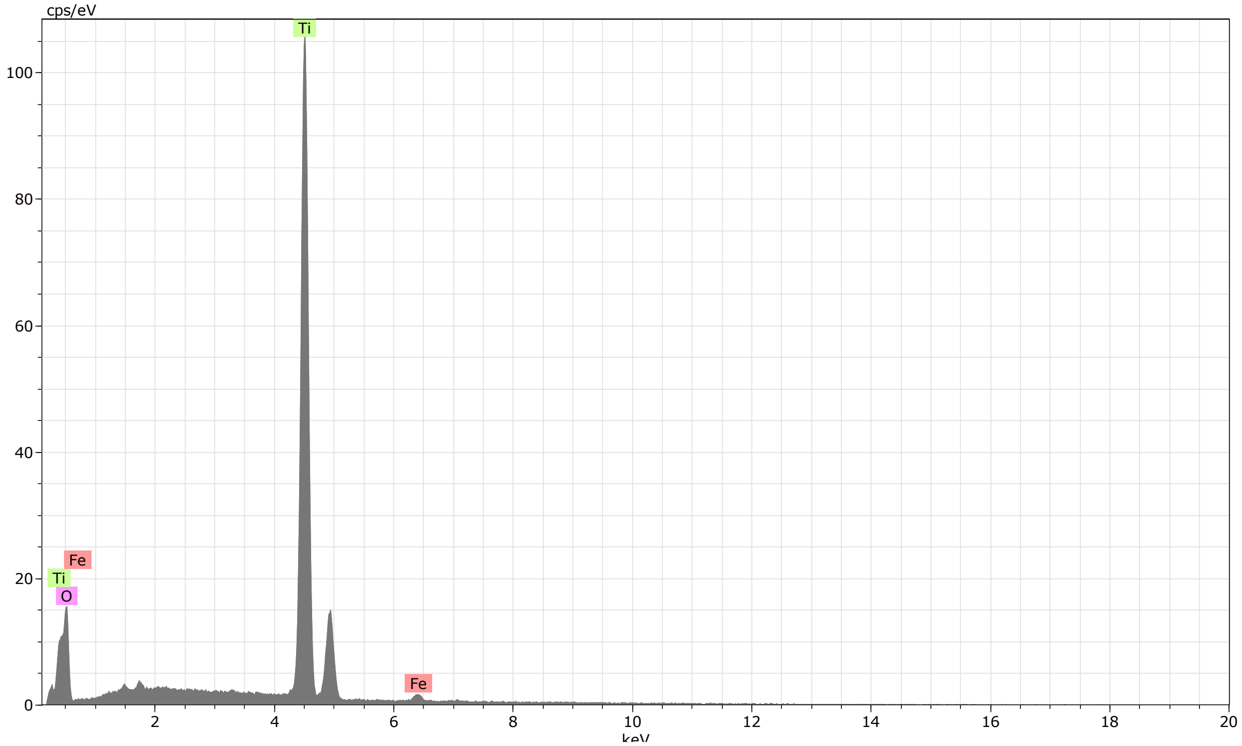

Appendix 20: Representative spectrum for rutile in all formations.

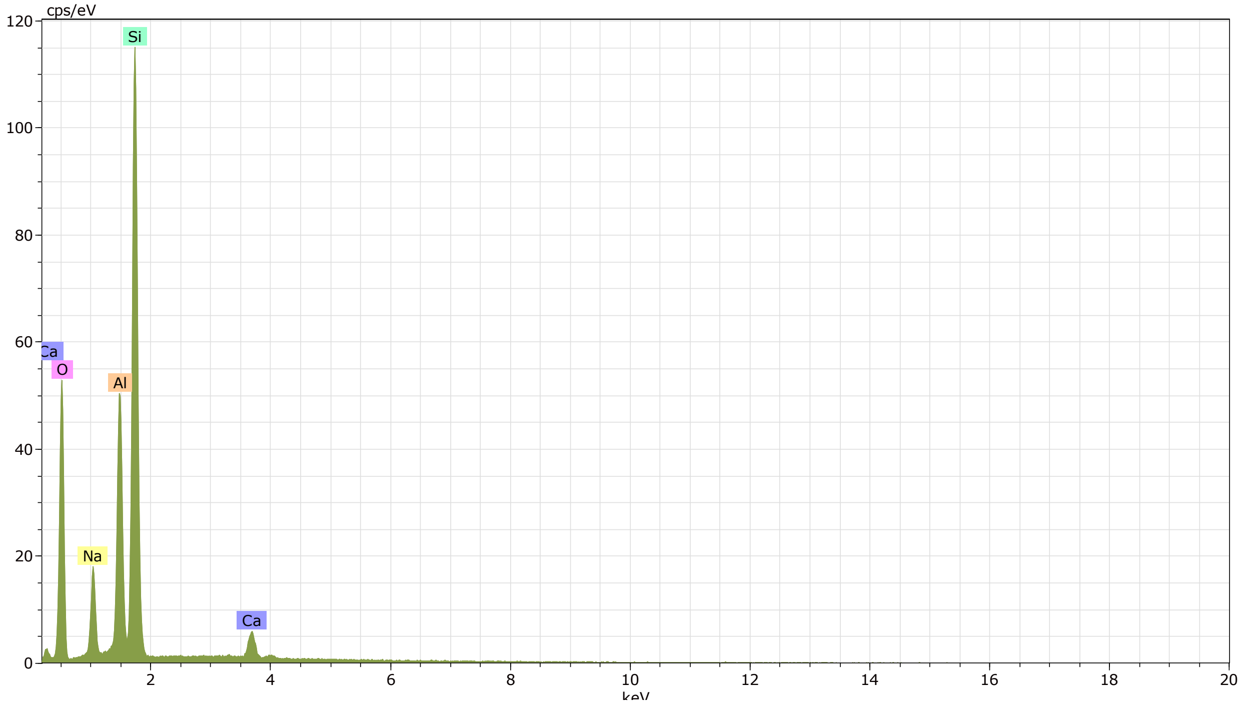

Appendix 21: Representative spectrum for the oligoclase lamellae observed in the albite-oligoclase lamellar grain.

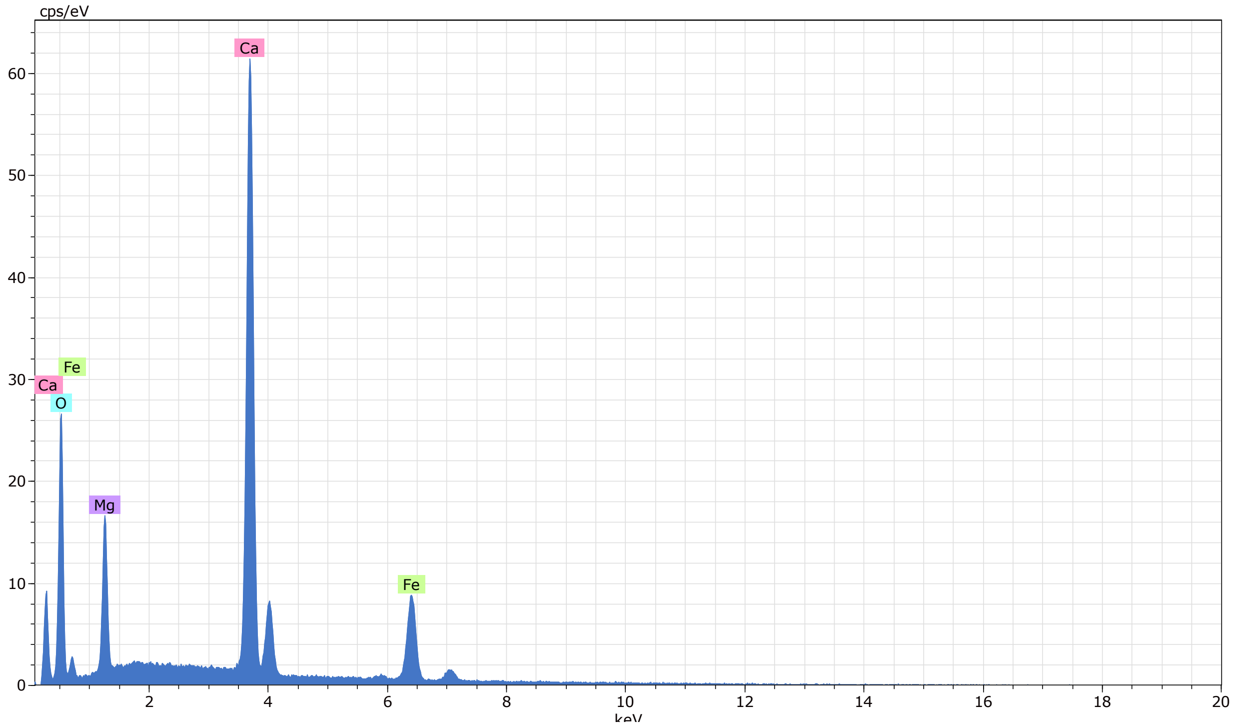

Appendix 22: Representative spectrum for calcite in the Nordmela Formation.

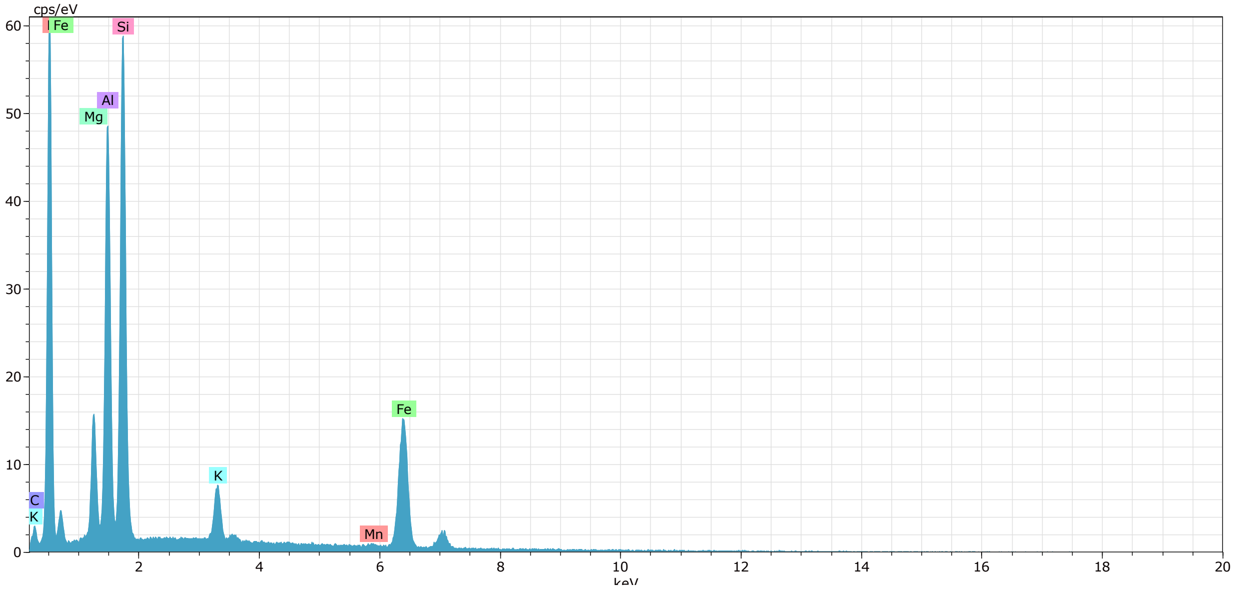

Appendix 23: Representative spectrum for what is thought to be glauconite in all formations.

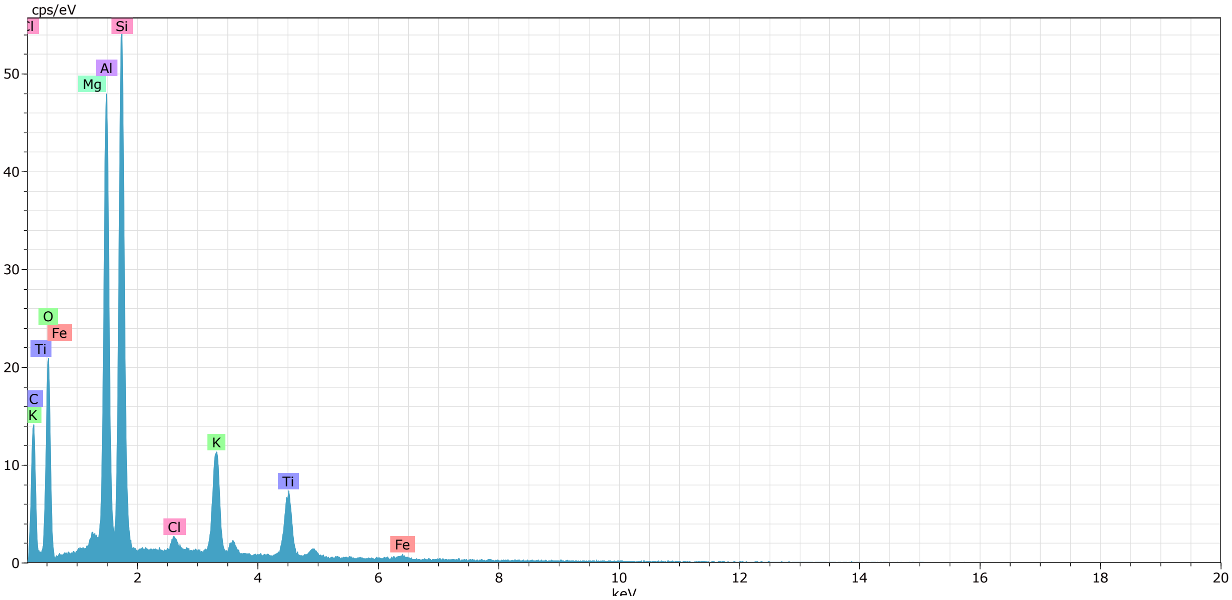

Appendix 24: Representative spectrum for titanium-enriched illite in all formations.

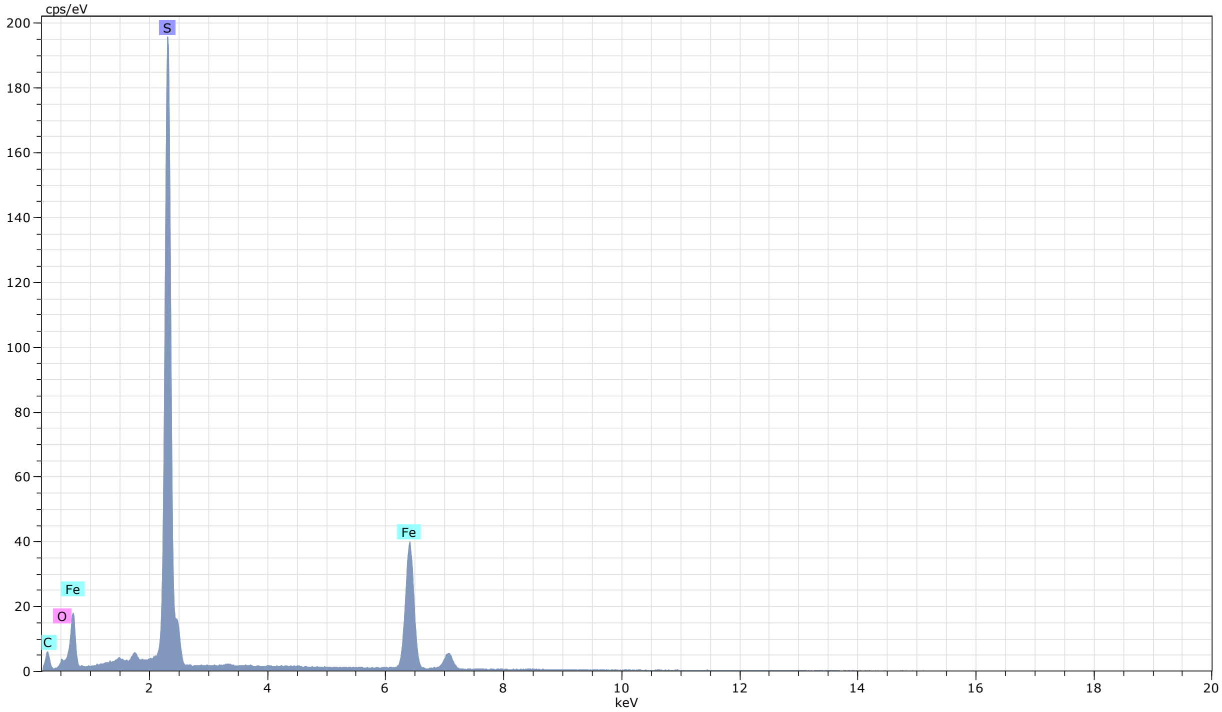

Appendix 25: Representative spectrum for pyrite in all formations.

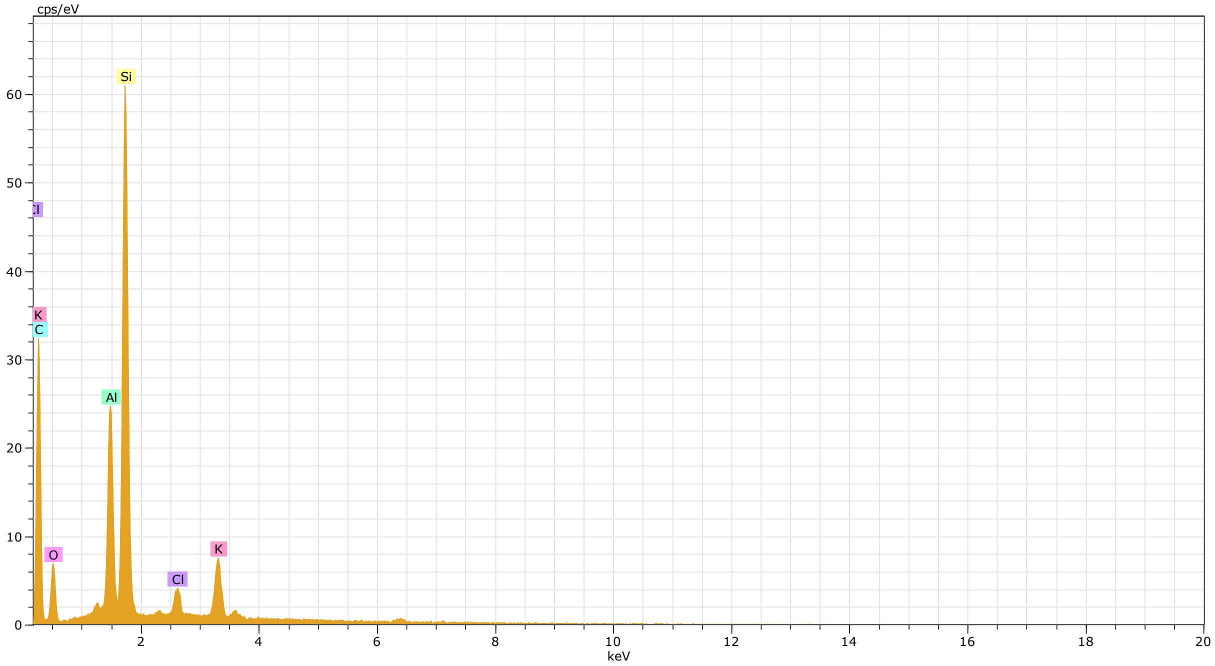

Appendix 26: Representative spectrum for partly dissolved K-feldspar in the Nordmela Formation.

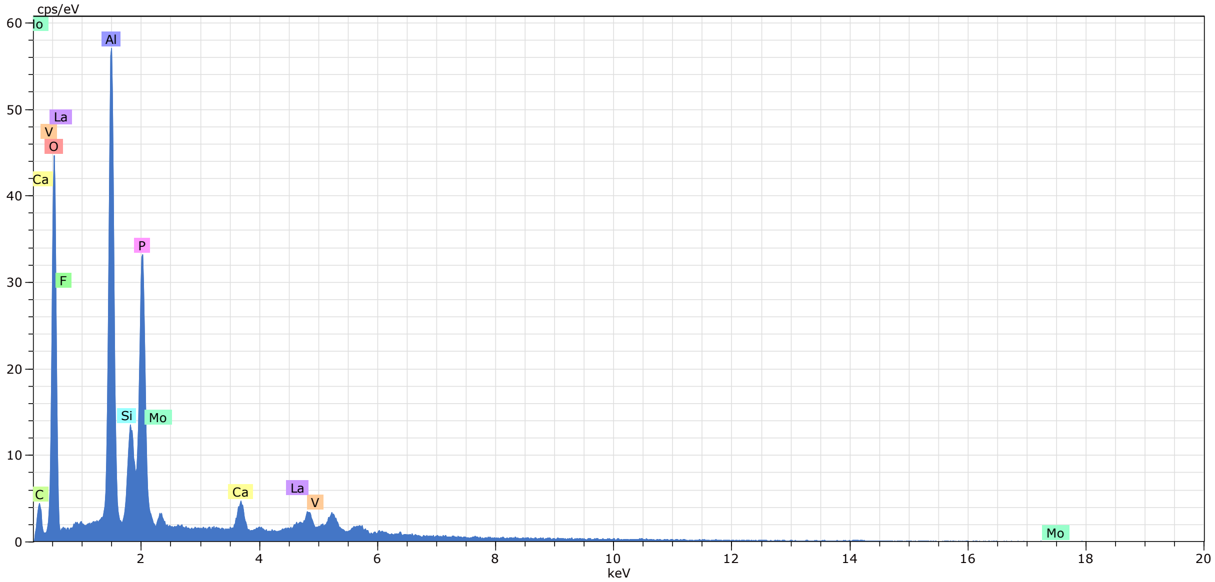

Appendix 27: Representative spectrum for florencite in the Nordmela and Fruholmen Formations.

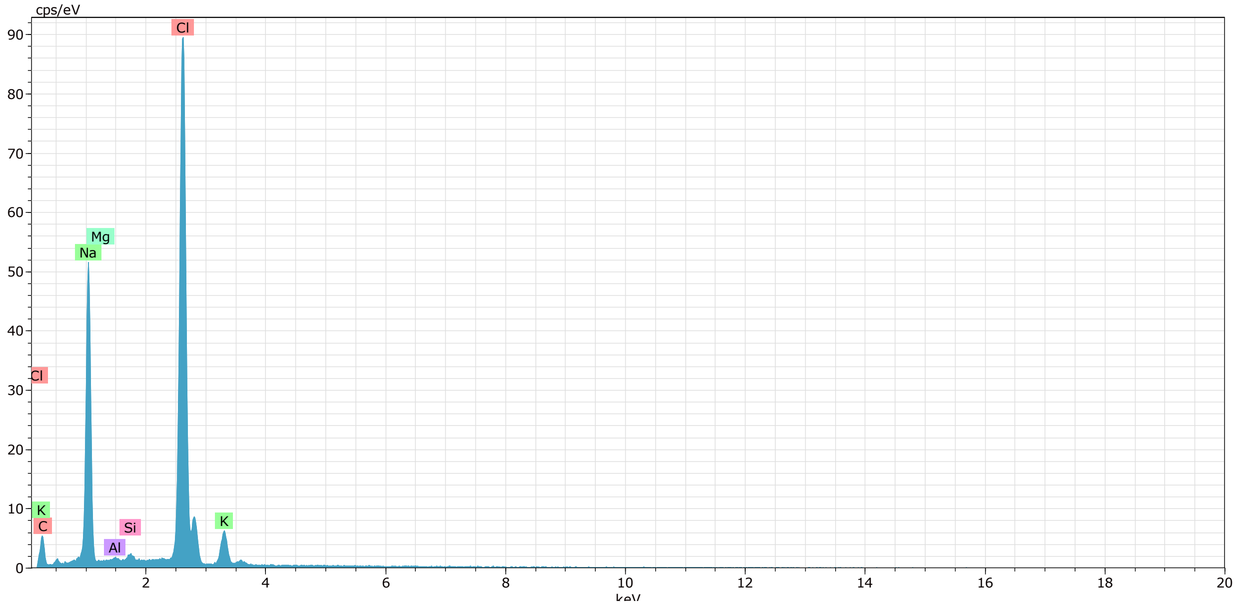

Appendix 28: Representative spectrum for halite in the Fruholmen Formation.

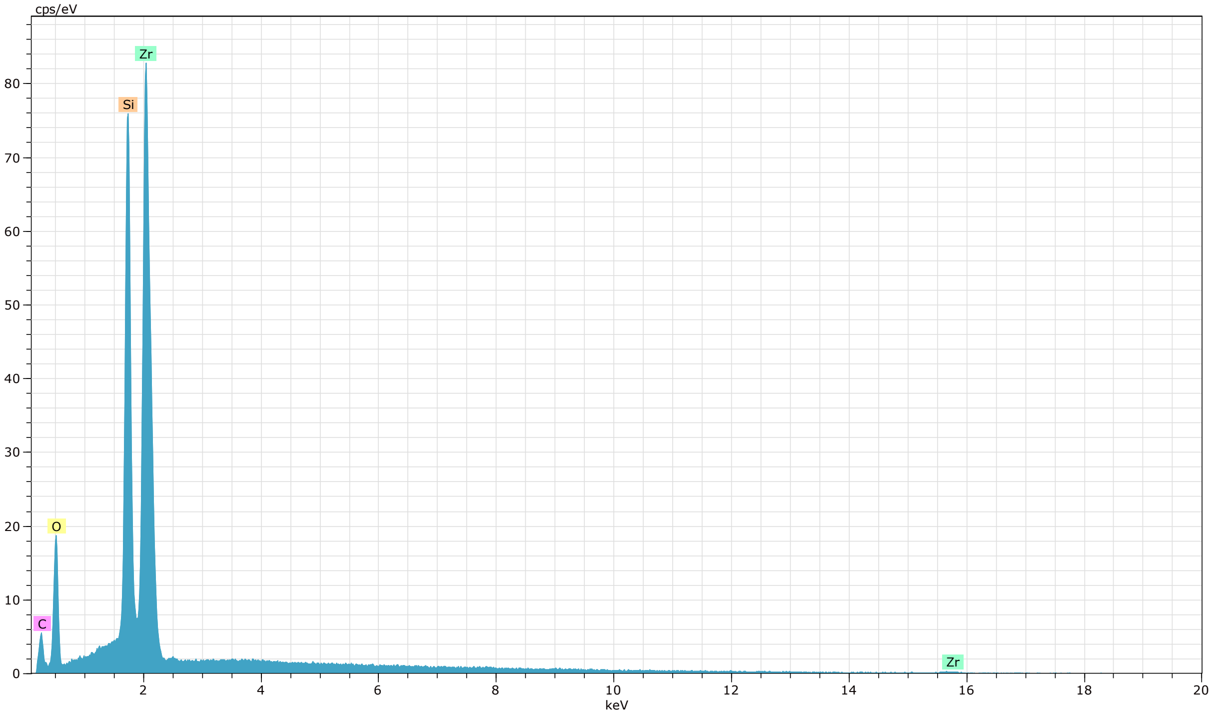

Appendix 29: Representative spectrum for zircon in all formations.

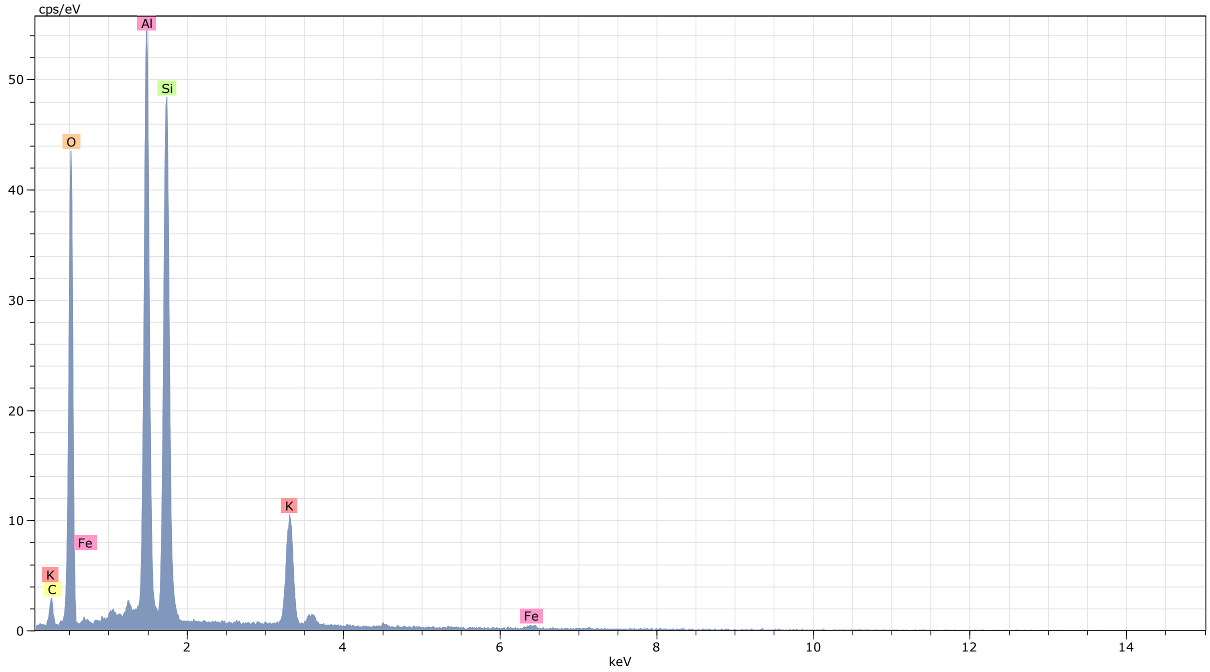

Appendix 30: Representative spectrum for muscovite in all formations.

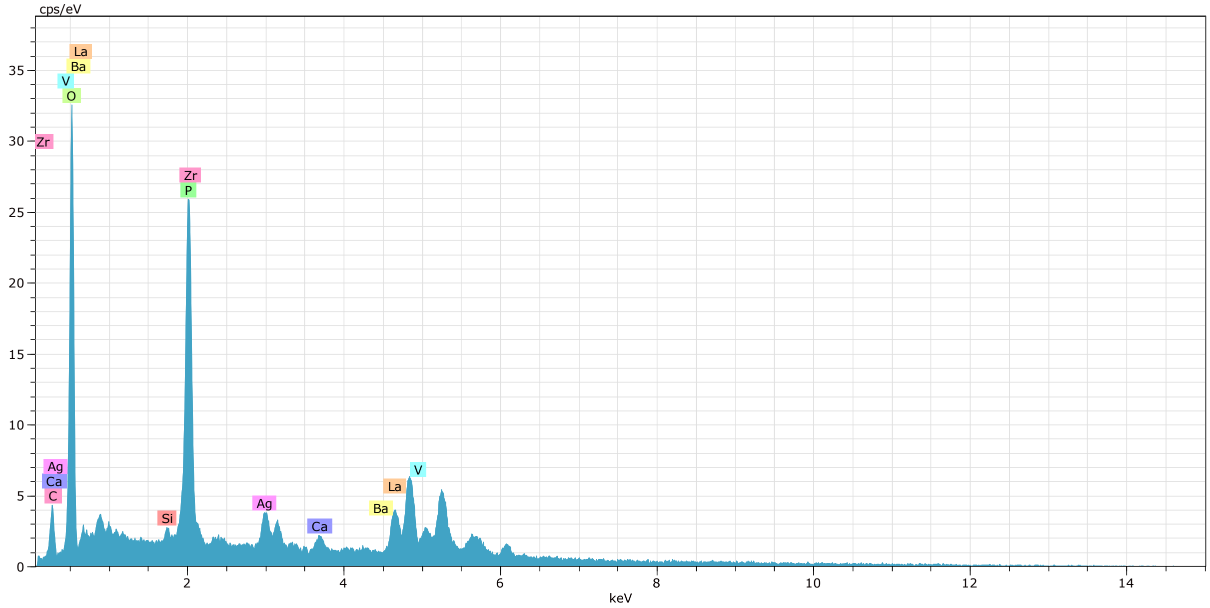

Appendix 31: Representative spectrum for monazite in the Fruholmen Formation.

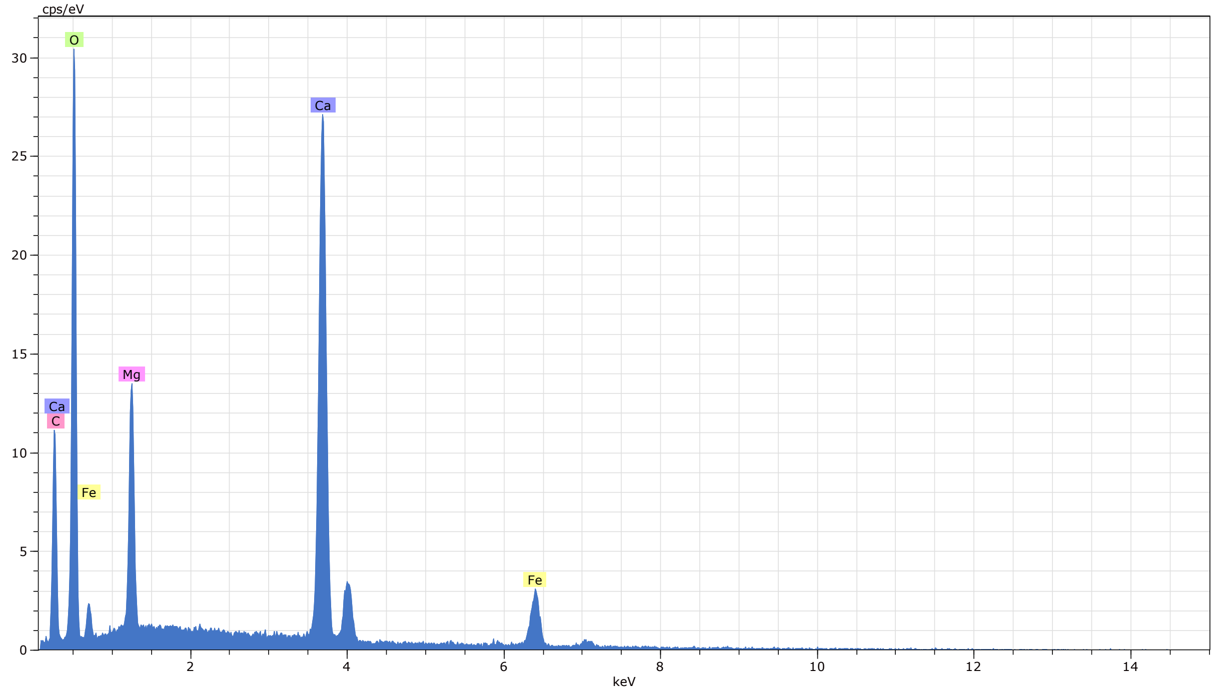

Appendix 32: Representative spectrum for Mg-rich calcite in the Fruholmen Formation.

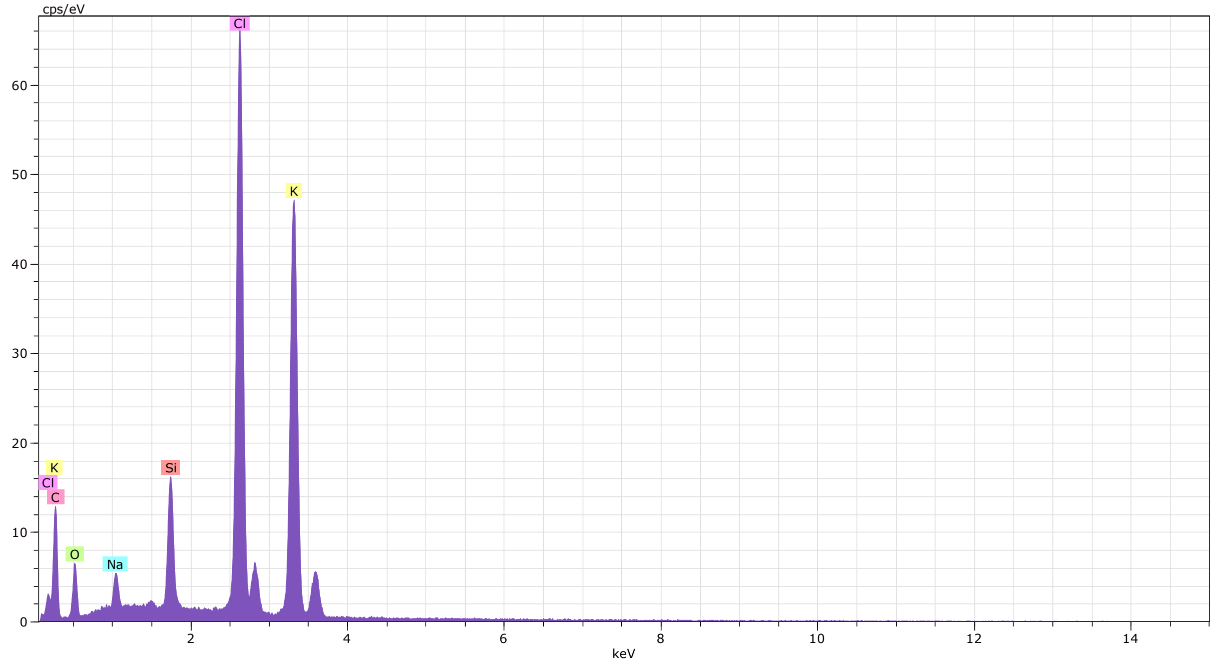

Appendix 33: Representative spectrum for sylvite in all formations.

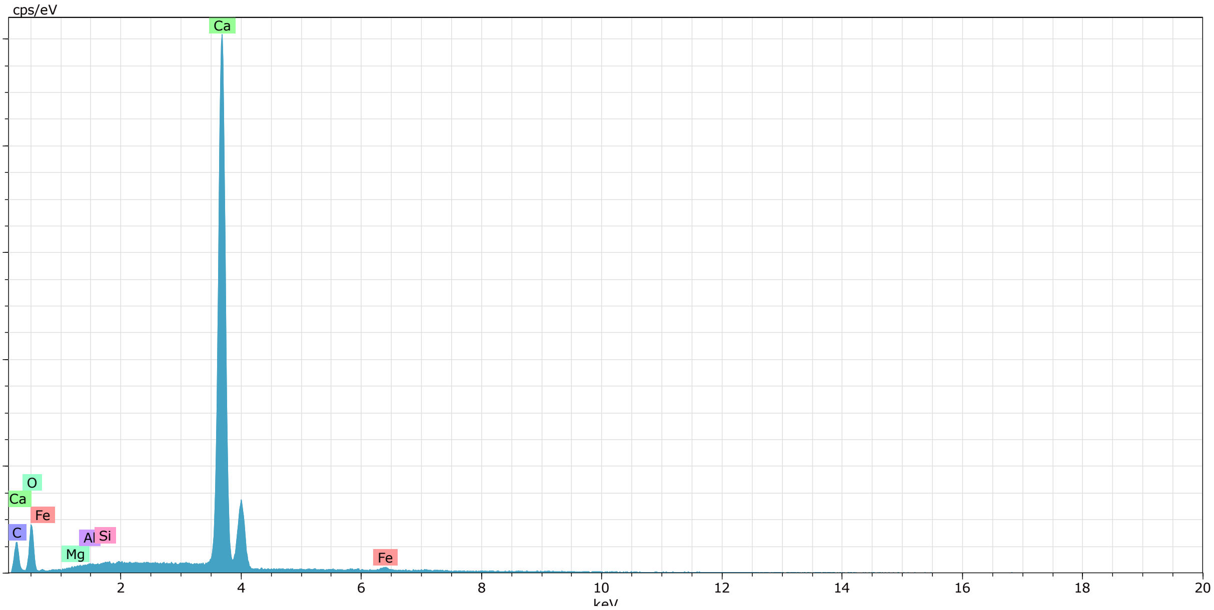

Appendix 34: Representative spectrum for clean calcite in the Fruholmen Formation.

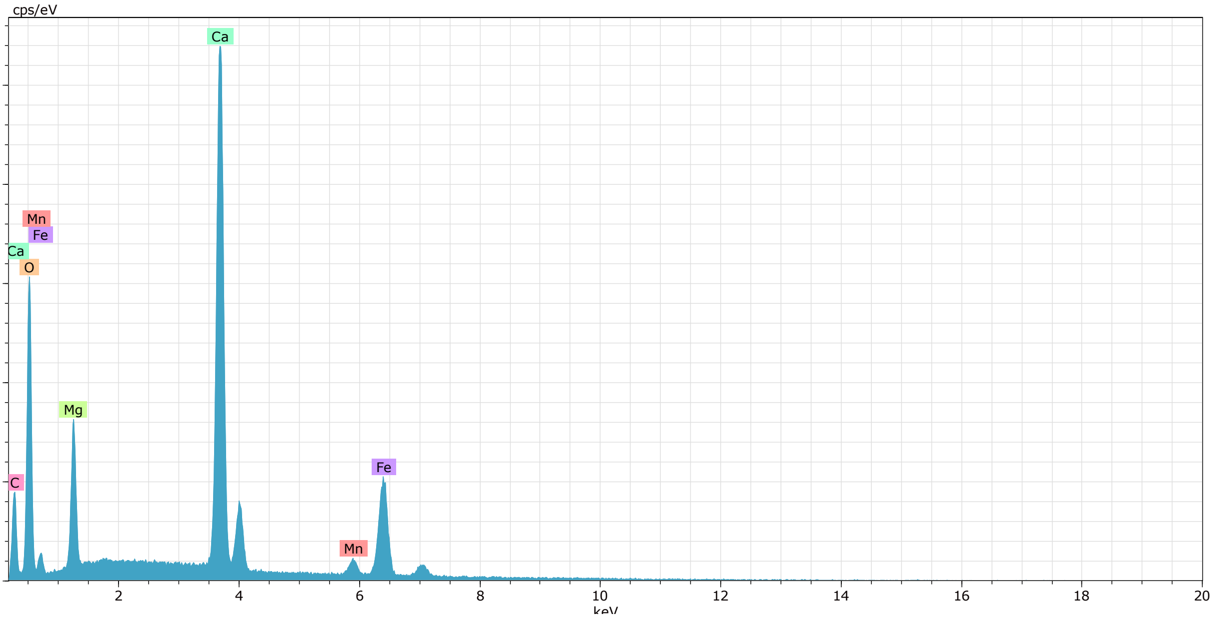

Appendix 35: Representative spectrum for ankerite in the Snadd Formation.

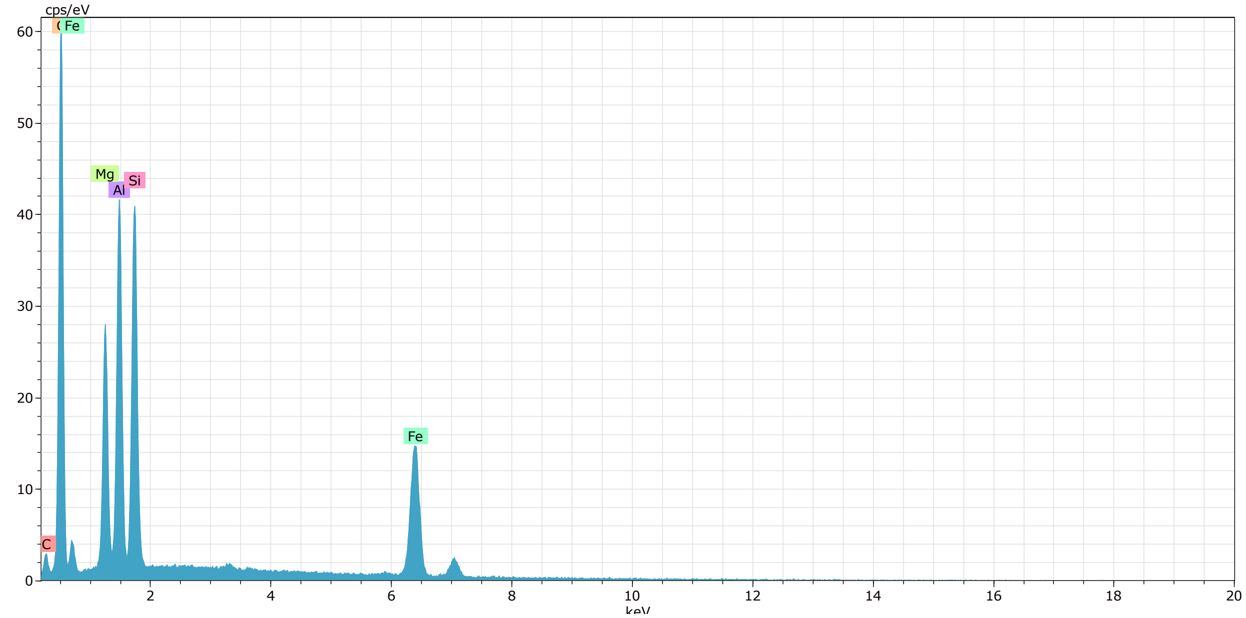

Appendix 36: Representative spectrum for chlorite in the Snadd Formation.

Appendix C – perthite data points

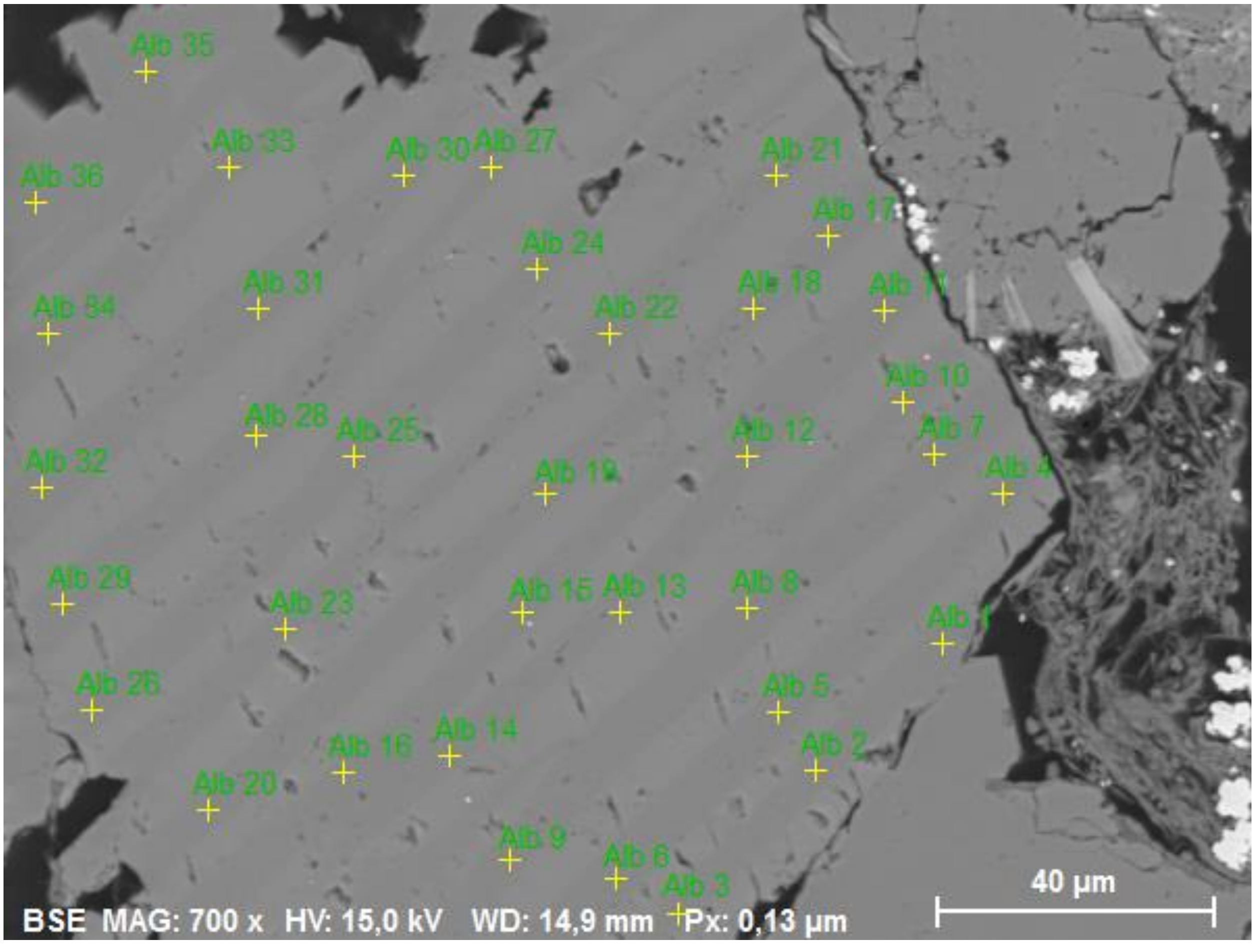

Appendix 37: Composition analysis points for albite component of albite-oligoclase lamellar grain.

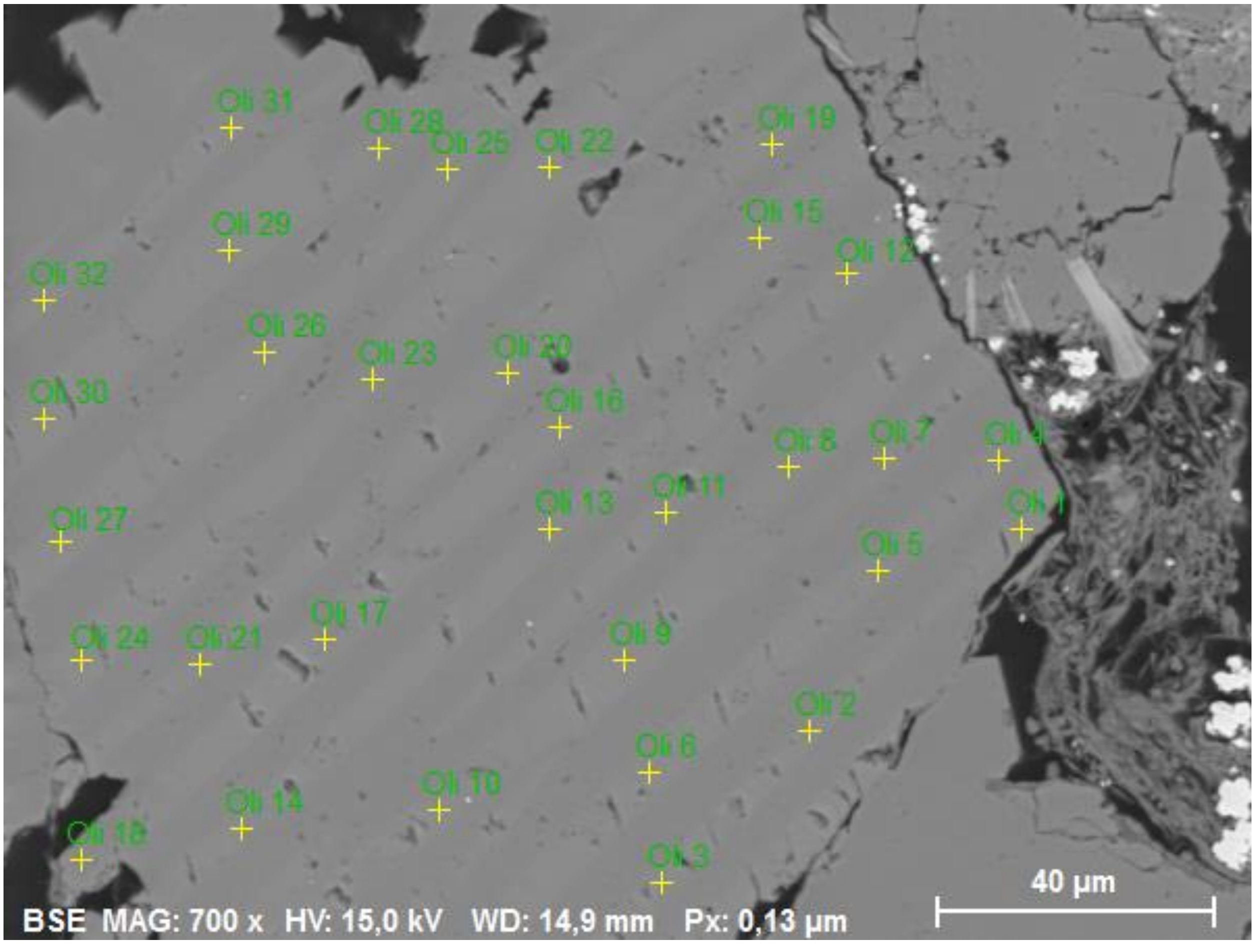

Appendix 38: Composition analysis points for oligoclase component of albite-oligoclase grain.